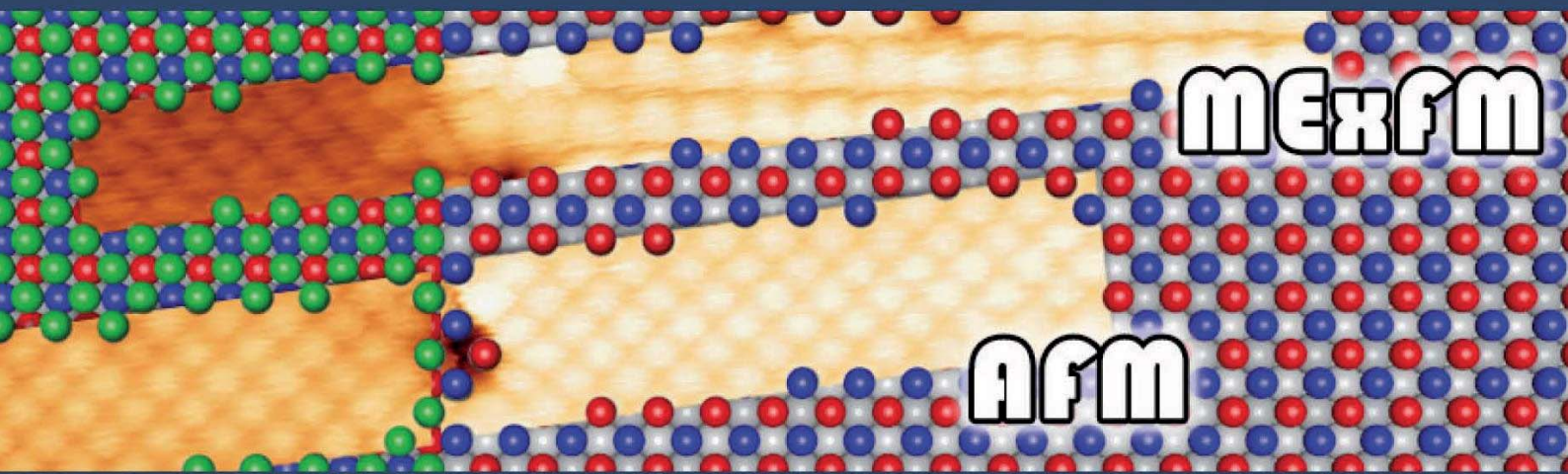


René Schmidt



Magnetic Exchange Force Microscopy and Spectroscopy on Fe/W(001)



Cuvillier Verlag Göttingen
Internationaler wissenschaftlicher Fachverlag

MAGNETIC EXCHANGE FORCE MICROSCOPY AND SPECTROSCOPY ON Fe/W(001)

Dissertation
zur Erlangung des Doktorgrades
des Department Physik
der Universität Hamburg

vorgelegt von
Dipl. Phys. René Schmidt
aus Rheda-Wiedenbrück

Hamburg
2011

Bibliografische Information der Deutschen Nationalbibliothek

Die Deutsche Nationalbibliothek verzeichnet diese Publikation in der Deutschen Nationalbibliografie; detaillierte bibliografische Daten sind im Internet über <http://dnb.d-nb.de> abrufbar.

1. Aufl. - Göttingen: Cuvillier, 2011

Zugl.: Hamburg, Univ., Diss., 2011

978-3-86955-855-4

Gutachter der Dissertation:	Prof. Dr. Roland Wiesendanger Prof. Dr. Hans Peter Oepen
Gutachter der Disputation:	Prof. Dr. Roland Wiesendanger Prof. Dr. Stefan Heinze
Datum der Disputation:	29.07.2011
Vorsitzender des Prüfungsausschusses:	Dr. Stefan Mendach
Vorsitzender des Promotionsausschusses:	Prof. Dr. Peter Hauschildt
Dekan der MIN-Fakultät:	Prof. Dr. Heinrich Graener

© CUVILLIER VERLAG, Göttingen 2011
Nonnenstieg 8, 37075 Göttingen
Telefon: 0551-54724-0
Telefax: 0551-54724-21
www.cuvillier.de

Alle Rechte vorbehalten. Ohne ausdrückliche Genehmigung des Verlages ist es nicht gestattet, das Buch oder Teile daraus auf fotomechanischem Weg (Fotokopie, Mikrokopie) zu vervielfältigen.

1. Auflage, 2011

Gedruckt auf säurefreiem Papier

978-3-86955-855-4

ABSTRACT

In this work scanning probe techniques, namely frequency-modulated atomic force microscopy (FM-AFM) in the non-contact regime and related methods like Kelvin probe force microscopy (KPFM), magnetic force microscopy (MFM), and magnetic exchange force microscopy (MExFM), are utilized in ultra high vacuum and at low temperatures to structurally, electronically and magnetically study the monolayer regime of iron on tungsten (001) in real space. Implementing the spectroscopic mode of MExFM, that is, magnetic exchange force spectroscopy (MExFS), the exchange interaction between single iron atoms with antiparallel coupling is experimentally accessed for the first time.

Iron grows pseudomorphically on W(001) whereby the layers are highly strained. Differences in strain between first and second layer iron and hybridization with the substrate lead to differences in electronic properties and magnetism: both layers exhibit a different work function, mapped with KPFM. Interestingly, even on the same layer, different work functions are observed. Moreover, both layers are magnetically different. The second layer is ferromagnetic (FM) with in-plane anisotropy as verified by MFM, while the first layer is antiferromagnetic (AF) with out-of-plane anisotropy. Using MExFM the AF alignment of the monolayer magnetic moments is resolved by detecting the short-ranged magnetic exchange force between tip and sample. The origin of the magnetic contrast formation is discussed and compared to *ab initio* calculations. Later, MExFS, which allows to directly measure the distance dependence of the magnetic exchange interaction between an atomically sharp magnetic tip and the antiferromagnetically ordered Fe monolayer on W(001), is employed. The site specific distance dependence of the total tip-sample interaction is recorded above Fe atoms which exhibit parallel as well as antiparallel atomic magnetic moments. The contribution of the magnetic exchange interaction between both sites can be extracted by subtracting the two curves from each other. All other interactions are identical on both sites. The experimental results are compared to *ab initio* calculations accounting for magnetically different tips composed of either Cr or Fe, or mixtures of both. Depending on symmetry and stability of the experimentally used probe tips, qualitatively different MExFM contrasts and MExFS data with a stronger distance dependence are observed. By analyzing the energy loss per

single cantilever oscillation cycle, simultaneously recorded with topography and frequency shift in the experiments, a bottom-up characterization of the structurally and magnetically unknown probe tip apex is given. Considering the tip apex as magnetically and structurally independent cluster allows to explain the observed tip behavior.

CONTENTS

Abstract	i
1 Introduction	1
2 Magnetism in Solids	5
2.1 Atomic Magnetism	5
2.1.1 Exchange Interaction between Atoms	7
2.1.2 Magnetism in Metals	10
3 Atomic Force Microscopy and Spectroscopy	17
3.1 Principle of AFM	17
3.2 Forces between Surface and Probe	18
3.3 Dissipation of Energy	23
3.3.1 Apparent Damping	24
3.3.2 Dissipation Mechanisms	25
3.4 Imaging Modes	26
3.5 Spectroscopy Modes	28
3.5.1 Bias Spectroscopy	28
3.5.2 Force Spectroscopy	29
3.5.3 Dissipation Spectroscopy	32
3.6 Frequency Shift to Force Conversion	33
4 Instrumentation and Preparation	37
4.1 Set-up	37
4.2 Tip Preparation	39
4.3 Sample Preparation	43
5 Growth and Properties of 1st and 2nd layer Fe on W(001)	49
5.1 Structural Properties	49
5.2 Electronic Properties	52
5.3 Magnetic Properties	54
6 Magnetic Exchange Force Microscopy on Fe/W(001)	61
6.1 MExFM using Ferromagnetic Tips	62
6.2 MExFM using Antiferromagnetic Tips	68

6.3	MExFM in Zero Field	68
6.4	MExFM near Structural Defects	69
6.5	Distance Dependence of MExFM Contrast	73
7	Magnetic Exchange Force Spectroscopy on Fe/W(001)	75
7.1	MExFS using Stable Tips	75
7.2	Tip State Switching during Spectroscopy	82
7.2.1	Magnetically Unstable Tips	82
7.2.2	Structurally Unstable Tips	83
8	Tip Modifications	87
8.1	Dissipation of Energy	88
8.1.1	Atomic Scale Dissipation Contrast	90
8.1.2	Chemical and Exchange Interaction Induced Dissipation	92
8.1.3	Tip Classification	93
8.2	Spontaneous Tip Modifications	94
8.2.1	Structural Changes	95
8.2.2	Magnetic Changes	97
8.3	Intended Tip Modifications	104
8.3.1	Spectroscopic Method	104
8.3.2	Scanning at Close Distance	107
9	Summary and Outlook	109
	Bibliography	115
	Publications	128
	Conferences	129

CHAPTER 1

INTRODUCTION

The semi-empirical Bethe–Slater curve, known since 1930 (figure 2.3), shows that, when the separation between atomic moments in a solid is varied by changing the element and hence the lattice constant, the exchange interaction changes from antiferromagnetic to ferromagnetic or vice versa. To directly access and measure this distance dependence of the exchange interaction strength between two magnetic atoms of the same element is not possible, because the separations between magnetic atoms in a solid of a given material are fixed by the crystal structure. On surfaces the situation changes and surface imaging techniques can be applied to address this theoretical hypothesis.

Scanning probe methods such as spin-polarized scanning tunnelling microscopy (SP-STM) [1–4], spin-flip spectroscopy [5, 6], and the recently developed atomic force microscopy (AFM) [7, 8] based magnetic exchange force microscopy (MExFM) [9, 10], allow one to study magnetic ordering on surfaces with atomic scale precision. SP-STM and MExFM allow for direct characterization of even more complex magnetic structures with atomic-scale resolution. These techniques help to gain a fundamental understanding of spin-related magnetic phenomena within the field of condensed matter research.

In the past, scanning tunneling spectroscopy (STS) has been employed to measure the oscillatory distance dependent nature of the Ruderman-Kittel-Kasuya-Yosida (RKKY)-type magnetic exchange interaction between pairs of individual Co adatoms on Cu(111) by evaluating the Kondo resonance using a non-magnetic tip [11], and on Pt(111) by analyzing magnetization curves using a magnetic tip [12]. In both cases the magnetic coupling was mediated via conduction electrons of the non-magnetic substrate.

While the application of SP-STM and SP-STs, which combine the atomic-resolution capability of STM with spin sensitivity, is limited to probe conducting systems, that is, metallic and semiconducting magnetic nanostructures, MExFM opens up the possibility to extend spin characterization with at least equal precision towards insulators. Proposed by R. WIESENDANGER *et al.* [13] in 1991, the basis of MExFM is to combine the atomic resolution capability of

AFM with the magnetic sensitivity of magnetic force microscopy (MFM) [14], but down to single spin resolution. Applying MExFM, the exchange interaction between a magnetic probe and the single magnetic moments of surfaces is visualized in real-space at length scales that are not accessible by other magnetic sensitive techniques, such as MFM [15] and magnetic resonance force microscopy (MRFM) [16]. Hence, MExFM promises to be a powerful tool to investigate many different types of exchange interactions, such as direct exchange or the prominent RKKY-interaction, either mediated by a substrate, between single molecules, or even single atoms.

The feasibility of MExFM to map spin structures with atomic resolution on insulating surfaces was demonstrated on antiferromagnetic NiO(001) [9, 17]. The key to success, in contrast to previous attempts to perform MExFM [18–22], was the application of an external magnetic field. The field was used to align the magnetic moment of the foremost probe tip apex atoms to enhance the interaction strength between the tip and sample moments. Implementation of the magnetic field paved the way for direct measurement of the magnetic exchange coupling between tip and sample atoms and for the visualization of the rowwise antiferromagnetic contrast between neighbouring rows of Ni atoms.

This work expands upon the first successful application of MExFM towards more systems and more capability. The sample system studied within this work is the first and second atomic layer of iron on tungsten with surface orientation (001). The focus, however, is put on the first atomic iron layer. This layer has been subject to theoretical considerations using density functional theory (DFT) [23], and it has already been studied earlier using SP-STM [24]. It has been found that, due to hybridization with the tungsten substrate, the iron monolayer becomes antiferromagnetic with out-of-plane anisotropy, that is, monolayer Fe atoms arrange in a checkerboard pattern with the moment of every second iron atom pointing either up or down, respectively.

The electronic and magnetic structure of iron is very different to that of the insulating NiO. Namely, the itinerant d -electron spins of the iron ML are delocalized, while, in NiO, the d -electrons are localized at the Ni atoms and couple via superexchange. Therefore, the study of Fe/W(001) with MExFM and the comparison to NiO(001) allows new insights into the contrast mechanism in MExFM. Since no further systems have been investigated successfully with MExFM, and since there is a lack of experiments on insulators which can be compared with SP-STM studies [1, 4, 12, 25–27], it is vital to understand the relevant contrast mechanisms in detail to clarify whether MExFM can be developed into a versatile tool for the analysis and manipulation of atomic scale magnetic structures.

Up to now, MExFM was only utilized in imaging mode. However, its spectroscopic mode, that is, measuring the interaction between probe tip and sample as a function of tip-sample distance, should allow to directly measure the distance dependence of the exchange interaction between single magnetic mo-

ments and a magnetic tip across a vacuum gap. By performing such measurements, as shown here, it is now possible to quantify the magnitude of the exchange interaction for the first time. Hence, this work presents the first successful application of the spectroscopic mode of MExFM, i.e. magnetic exchange force spectroscopy (MExFS), where, in contrast to previous STM-based experiments [11,12], the magnetic exchange interaction is not mediated by a substrate.

After an introduction into the field of atomic magnetism in chapter 2, chapter 3 introduces the basic principles of AFM, where a super-sharp tip probe, mounted at the end of a vibrating cantilever, scans a surface. Within a certain distance between tip and surface, tip-sample interactions lead to a mechanical response of the cantilever vibration. Measuring this response allows for the analysis of the various interaction forces, such as chemical and magnetic exchange force, with a sensitivity of a few pN. A detailed description of the experimental setup and the preparation of Fe/W(001) are found in chapter 4.1. Chapter 5 discusses different properties of the used probes and the sample system, studied with KPFM and MFM.

After characterization of both, probe and sample, the $c(2 \times 2)$ surface magnetic unit cell of the iron monolayer is obtained by MExFM utilizing iron and chromium coated probes, presented in chapter 6. By comparison with theory, the origin of the obtained image contrast of the magnetic moments oriented perpendicular to the surface is revealed. Due to the difference in electronic structure, the corrugation amplitude as obtained on Fe/W(001) is essentially larger than it was observed in the first MExFM experiments performed in 2007 on NiO(001) [17]. Furthermore, chromium coated probes turn out to be much better suited than iron coated probes at small tip-sample separation for stable imaging with atomic and spin resolution. In contrast to the preliminary experiments on NiO(001), first successful MExFM experiments without external magnetic field are performed using chromium coated probes.

Chapter 7 presents the first direct measurement of the magnetic exchange interaction across a vacuum gap by combining magnetic exchange force spectroscopy (MExFS) and three-dimensional force field spectroscopy (3D-FFS). In MExFS, the spin sensitive probe is approached perpendicular to the sample surface and the total interaction potential between tip and sample is measured. Subtracting two curves obtained on oppositely oriented atomic magnetic moments on the surface yields the magnetic exchange interaction between both moments. All non-magnetic interactions are elegantly eliminated using this method, since all surface iron atoms are chemically identical. Comparison with DFT calculations reveals that theory is able to reproduce the measured magnetic exchange energy qualitatively and quantitatively using pyramidal shaped tips. However, some experimental results are not reproducible. They indicate that the used tips are not stable but undergo a strong modification during approach and retraction within single cantilever oscillation cycles. This assumption is supported by a strong variation of the energy dissipated while

keeping the oscillation amplitude of the cantilever constant. A survey on dissipation is presented in chapter 8 and leads to a classification of the used probe tips as either stable or unstable.

Chapter 8 further presents methods for the *in situ* preparation of magnetic sensitive tips. It is shown that, although coated with magnetic material, the tips used in this work do not show spin sensitivity from the beginning. Instead, spontaneously or deliberately induced modifications of the tip apex are needed to eventually perform successful MExFM and MExFS experiments. The findings of the last chapter are of further interest concerning the manipulation of single atoms in MExFM for realizing future atomic spin logic devices [28].

CHAPTER 2

MAGNETISM IN SOLIDS

The background of magnetic phenomena in solids are magnetic moments (spins) of electrons. Spins are able to interact in a cooperative way, which leads to a behavior quite different from what is observed, if magnetic moments are isolated from each other. Spin-coupling via one of the various types of magnetic exchange interaction leads to a surprisingly rich variety of magnetic properties in solids. This chapter shall introduce into the field of magnetism in a rather short and simple way from single magnetic moments to magnetic interactions between ordered moments in a solid. For simplicity, from knowledge base, as one can find it in recent textbooks [29–31], only the parts fundamental to understand this work are discussed. The discussion is focused on the magnetism of the 3d-metals iron and chromium, as they are the matter of interest in this work.

2.1 Atomic Magnetism

The quantum mechanical spin \mathbf{S} and the orbital angular momentum \mathbf{L} of an electron result in a magnetic dipole moment. For the sake of simplicity this atomic magnetic moment will be referred to as ‘spin’ throughout this work¹. In atoms with filled electron shells, the spins are in up/down² pairs and the total magnetic moment of all electrons is zero. Atoms with partially filled shells do have a net magnetic moment, written as a multiple of the *Bohr magneton*

¹Not only electrons have a magnetic moment, but also nuclei can possess a non-zero spin resulting from their angular momentum. However, nuclear magnetic moments are typically a thousand times smaller than electronic moments and are not relevant in the context of this work.

²The spin quantum number s takes the value of $\frac{1}{2}$ for electrons. For the value of the spin angular momentum $m_s\hbar$ this means only two possible values so that $m_s = \pm\frac{1}{2}$. The component of angular momentum along a particular axis is then $\hbar/2$ or $-\hbar/2$, referred to as ‘up’ and ‘down’, respectively.

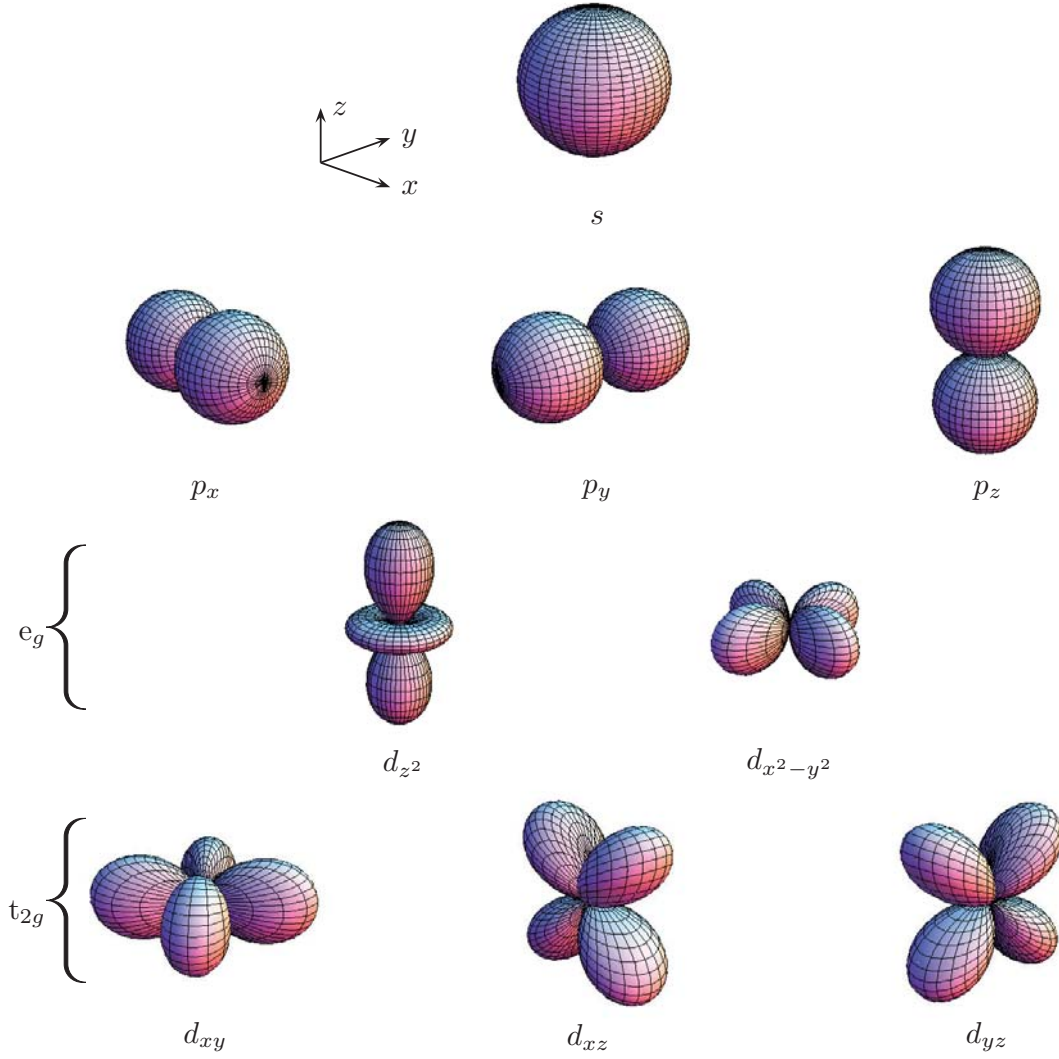


Figure 2.1: Angular electron density distribution of *s*, *p* and *d* orbitals. The *d_{z²}* and *d_{x²-y²}* levels are grouped together and called the *e_g* levels. The *d_{xy}*, *d_{xz}* and *d_{yz}* levels are grouped together and called the *t_{2g}* levels.

$\mu_B = \frac{e\hbar}{2m}$, which is a convenient unit to describe its magnitude. For bulk iron this value amounts to $2.2\mu_B$ [32,33].

Every solid is formed by atoms, which can either possess zero or a net magnetic moment larger than zero. To be able to characterize the magnetism of a material we have to take into account the cooperation of all magnetic moments carried by the individual atoms forming the solid. These moments and their interaction can depend on the particular environment of each atom, that is, its nature and the position of neighboring atoms, temperature, and external magnetic field. Moreover, the magnetic moments in a solid can be either localized or carried by delocalized conduction (itinerant) electrons that can move nearly free inside the solid.

The atoms of a paramagnet do have a non-zero magnetic moment because of unpaired electrons, but the moments of neighbouring atoms do have a negligible interaction with each other and can be assumed as independent. Without external magnetic field, they can orient themselves randomly in any direction, resulting in a zero net magnetic moment of the paramagnet. On applying a magnetic field, the spins are able to align with the field. This results in a net magnetic moment parallel to the applied field. Hence, paramagnetic materials are attracted to magnetic fields, but the total magnetization will drop to zero in the absence of the applied field.

To be able to consider the interactions between an atom and its immediate surroundings and the magnetic interactions between adjacent atoms in a crystal, it is convenient to review the shapes of the atomic orbitals [29]. Figure 2.1 shows the angular dependences of the electron density of the s , p and d orbitals. While the s orbital is the only one with spherical symmetry, the others have a pronounced angular dependence with zero electron probability density at the nucleus. The d orbitals are divided into two classes, the t_{2g} orbitals, pointing between the x , y and z axes (d_{xy} , d_{xz} and d_{yz} orbitals) and the e_g orbitals which point along these axes (the $d_{z^2-x^2-y^2}$, abbreviated to d_{z^2} , which has lobes pointing along the z axis and the $d_{x^2-y^2}$ with its lobes pointing along the x and y axes).

2.1.1 Exchange Interaction between Atoms

As the magnetic moments have been introduced as magnetic dipoles, the first interaction to be considered between two moments is the magnetic dipole interaction. The magnitude of the interaction of two iron dipoles with $2.2 \mu_B$ each, separated by their nearest neighbour distance in the metallic iron, $r = a/\sqrt{2}$, can be estimated to $\approx (\mu_0 \cdot (2.2\mu_B)^2 / 4\pi r^3) = 30 \mu\text{eV}$ corresponding to 0.35 K. Given that many magnetic materials arrange at much higher temperatures, like iron does up to its Curie temperature of $T_C = 1043 \text{ K}$, this interaction is too weak to account for the ordering. From molecular field theory we can calculate the exchange constant of iron to $J = 11.9 \text{ meV}$ [30], which is a four hundred times larger than the dipolar interaction. The molecular field³ can be estimated to $B_{\text{mf}} = 2100 \text{ T}$. Hence, it is a thousand times bigger than the contribution to a B -field due to the magnetization of iron, $\mu_0 M = 2.2 \text{ T}$. The high Curie temperature and the large internal field of iron can only be explained by exchange effects.

Up to this point all arguments are based on the overlap between orbitals of neighbouring atoms in a solid. Noteworthy, neither direct nor indirect exchange can explain the non-integral value of iron atoms of $2.2 \mu_B$ in the solid

³The molecular field model had been proposed by WEISS in 1907. It assumes that the exchange interaction is nothing more than an internal magnetic field B_{mf} and is related to the exchange interaction characterized by J_{ij} . It can be shown that T_C scales with the strength of the exchange interaction [30].

state. A correct description of magnetism in solids must include their band structure as well.

Since the interaction between electrons is governed by their Coulomb energy, we can describe the exchange interactions between two magnetic moments in a proper way by considering the wave functions of two undistinguishable electrons with $s = \frac{1}{2}$ which have spatial coordinates \mathbf{r}_1 and \mathbf{r}_2 , respectively. As fermions, electrons have to fulfill the Pauli exclusion principle. Therefore, the total wavefunction has to be antisymmetric. Considering the spin of the electrons, there are two possibilities: a symmetric spatial part ψ in combination with an antisymmetric spin part χ , representing a singlet state with $s = 0$, or an antisymmetric spatial part in combination with a symmetric spin part, representing a triplet state with $s = 1$. The total wave functions for both cases is written as

$$\psi_S = \frac{1}{\sqrt{2}}(\psi_a(\mathbf{r}_1)\psi_b(\mathbf{r}_2) + \psi_a(\mathbf{r}_2)\psi_b(\mathbf{r}_1)) \cdot \chi_S \quad (2.1)$$

$$\psi_T = \frac{1}{\sqrt{2}}(\psi_a(\mathbf{r}_1)\psi_b(\mathbf{r}_2) - \psi_a(\mathbf{r}_2)\psi_b(\mathbf{r}_1)) \cdot \chi_T. \quad (2.2)$$

The difference in energy between the singlet case ψ_S and triplet case ψ_T , $E_S - E_T$, is

$$E_S - E_T = 2 \int \psi_a^*(\mathbf{r}_1)\psi_b^*(\mathbf{r}_2)\hat{H}\psi_a(\mathbf{r}_2)\psi_b(\mathbf{r}_1)d\mathbf{r}_1d\mathbf{r}_2, \quad (2.3)$$

and the **exchange constant** (or exchange integral) J is defined as

$$J = \frac{E_S - E_T}{2} = \int \psi_a^*(\mathbf{r}_1)\psi_b^*(\mathbf{r}_2)\hat{H}\psi_a(\mathbf{r}_2)\psi_b(\mathbf{r}_1)d\mathbf{r}_1d\mathbf{r}_2. \quad (2.4)$$

Using \mathbf{S}_1 and \mathbf{S}_2 as operators for the two spin- $\frac{1}{2}$ electrons, their interaction can be described by the Hamiltonian

$$\hat{H} = A\mathbf{S}_1 \cdot \mathbf{S}_2. \quad (2.5)$$

After parametrization of singlet and triplet state the spin-dependent term of eq. 2.5 can be written as

$$\hat{H} = -2J\mathbf{S}_1 \cdot \mathbf{S}_2. \quad (2.6)$$

If $J > 0$, then $E_S > E_T$ and the triplet state $s = 1$ is favoured. If $J < 0$, then $E_S < E_T$ and the singlet state $s = 0$ is favoured. HEISENBERG found that this simple formula for two electrons can be applied between all neighbouring atoms in a solid and derived the Hamiltonian of the **Heisenberg model** as a simple three dimensional generalization of the spin-spin interaction of two electrons:

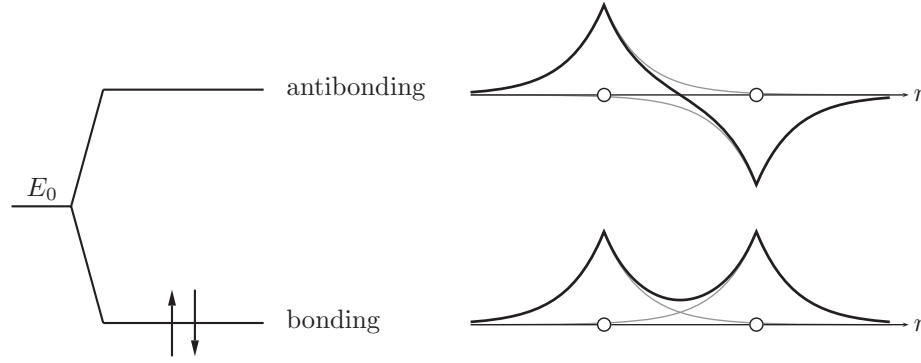


Figure 2.2: Regarding the exchange between two electrons on different atoms, molecular orbitals have to be considered. The sum of the two atomic orbitals is the so called bonding orbital, which is spatially symmetric with $S=0$. The bonding orbital is of lower energy than the antibonding orbital, which corresponds to the difference of the atomic orbitals and, which is spatially antisymmetric with $S = 1$. Due to its lower energy, the singlet ground state is favoured and the electrons fill the bonding state while the antibonding state is empty.

$$\hat{H} = - \sum_{ij} J_{ij} \mathbf{S}_i \cdot \mathbf{S}_j, \quad (2.7)$$

where J_{ij} is the distance dependent exchange constant between i^{th} and j^{th} spin. If the exchange interaction is negative ($J_{ij} < 0$) it is favourable for nearest neighbour magnetic moments to align antiparallel to each other and the solid is in an **antiferromagnetic (AF) ground state**. For a positive exchange interaction ($J_{ij} > 0$) it is favourable for the moments to align parallel to one another at $T = 0$ K resulting in a **ferromagnetic (FM) ground state**.

Ferromagnetism is characterized by a spontaneous magnetization even without applying an external magnetic field. For both ground states a critical temperature exists, at which the available thermal energy overcomes the interaction energy between the spins. Hence, paramagnetic behavior can also be observed in ferromagnets that are above their Curie temperature, and in antiferromagnets above their Néel temperature.

Direct Exchange

If two electrons are on the same atom, the exchange integral in the Heisenberg model is usually positive. Thus, the triplet state is stabilized and an antisymmetric spatial state is ensured, minimizing the Coulomb repulsion between the two electrons by keeping them apart. If the two electrons are on neighbouring atoms, any joint state will be a combination of two states, one centered on each atom. By forming bonds, the electrons can save kinetic energy, because now they are allowed to wander around both atoms rather than just one. Thus,

we have to consider molecular orbitals instead of atomic orbitals. Figure 2.2 demonstrates that the molecular orbitals can be either bonding, that is, spatially symmetric, or antibonding, that is, spatially antisymmetric. Because the antibonding orbital has a larger kinetic energy due to its greater curvature, the singlet state with antiparallel spin orientation is favoured and hence, the exchange integral is likely to be negative.

Indirect Exchange

As soon as two atoms are so far apart that the overlap between their spin carrying orbitals is negligible, direct exchange is not effective any more. However, magnetic ordering is still observed. This effect is most dramatic for Gd, where the spin is localized in the f -states, which do not overlap at all. In this case the exchange interaction is indirect, as it is mediated by the conduction electrons. The localized magnetic moment spin-polarizes the $5p$ and $6s$ conduction electrons and this polarization hence couples to a neighbouring localized magnetic moment in a distance r . This is known as RKKY-interaction, named after Ruderman, Kittel, Kasuya and Yosida, who discovered this effect [34–36]. The exchange integral takes the form of an r -dependent interaction given by

$$J_{\text{RKKY}}(r) \propto \frac{\cos(2k_{\text{F}}r)}{r^3}. \quad (2.8)$$

The oscillatory dependence with wavelength π/k_{F} shows that quite large variations in the strength of the interaction and even reversal of its sign are possible with small changes in the relationship between the interatomic distance and the periodicity of the spin density. For d -electron metals like Fe an analogous indirect exchange mechanism via the s -conduction electrons (s - d -coupling) is present and actually contributes stronger to the ferromagnetic ordering than the direct exchange due to the rather small overlap between the d -orbitals of neighbouring Fe atoms.

2.1.2 Magnetism in Metals

Magnetic order is relatively rare for pure materials. At room temperature only Fe, Co, Ni, Gd are ferromagnetic and only Cr and Mn are antiferromagnetic.

The Bethe–Slater curve [37] displays the correlation between the sign of the exchange constant J_{ex} and the ratio $r_{\text{ab}}/r_{\text{d}}$ with r_{ab} being the interatomic distance and r_{d} the radius of the d shell (see figure 2.3). As indicated in the figure this curve allows to distinguish between ferromagnetic $3d$ elements like Fe, Co, and Ni exhibiting a parallel alignment and thus a positive exchange constant and antiferromagnetic elements like Mn and Cr with an antiparallel orientation of the magnetic moments, having a negative exchange constant. The semi-empirical Bethe–Slater curve is widely used to explain changes in the magnetic moment coupling, when the interatomic distance between two atoms

is changed. However, it only considers direct exchange between overlapping d -orbitals in transition metals, but not the band structure of the solid.

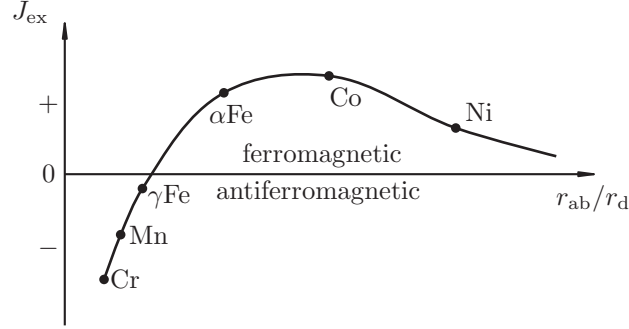


Figure 2.3: The semi-empirical Bethe–Slater curve links the magnitude of the exchange integral with the ratio of the interatomic distance r_{ab} and the radius of the d shell r_d .

The structure of iron is body-centred-cubic (bcc) with a bulk lattice constant of $a = 286.7$ pm [38]. However, the bond length of two adjacent iron atoms, which is their nearest neighbour distance, is $a/\sqrt{2} = 202.7$ pm [39]. With eight valence electrons the electronic configuration of iron is $[\text{Ar}].3d^6.4s^2$. The orbital radii of the outermost electrons of iron are calculated to 136.6 pm and 38.2 pm for the $4s$ - and $3d$ -orbital, respectively [40,41]. By reviewing the radial distribution of the $3p$, $3d$ and $4s$ orbitals of iron in figure 2.4, it becomes obvious that the $3d$ orbitals of two adjacent atoms in bulk iron do overlap, leading to a direct exchange between the magnetic moments of iron. This direct exchange is not effective, when two iron atoms are farther apart. Here, the exchange interaction is indirect and mediated by the $4s$ electrons (s - d -coupling).

Magnetic exchange mechanisms are important in allowing the magnetic moments in a solid to communicate with each other. Other magnetic exchange mechanisms like superexchange and double exchange do exist in solids, but they are not relevant for pure metals and thus are not discussed here.

Band Ferromagnetism

To understand collective magnetism in solids correctly, their band structure has to be considered. Metals exhibit conduction electrons that can be described as free electron gas, because they are able to travel through the solid as a result of the overlap between the wave functions of neighboring atoms in the lattice structure. The wave functions thus form a band with an equal number of spin up and spin down electrons. When a magnetic field is applied, only the electrons in a range $k_B T$ close to the Fermi level will respond by raising or lowering their energy depending on their spin. A small surplus of one type of spins will result. The spin-split bands are separated by $g\mu_B B$ (for electrons the g -factor amounts to 2 at $T = 0$ K, neglecting the orbital momentum), indicating

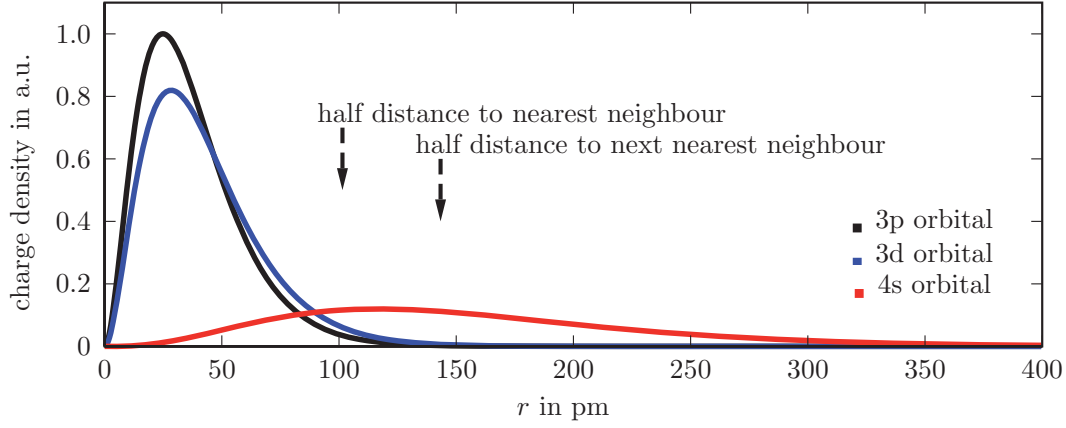


Figure 2.4: Radial distribution of the $4s$, $3p$ and $3d$ orbitals in iron. Half distance values to nearest and next nearest neighbours in the metal are marked by arrows. Obviously, the orbitals of the spin carrying $3d$ electrons and of the $4s$ conduction electrons of two adjacent iron atoms do overlap.

that the splitting is very small. This weak paramagnetic effect, known as **Pauli-paramagnetism**, is visualized in figure 2.5a.

Spontaneous spin splitting

Considering paramagnetic spin split bands, an equal number of spin up and spin down electrons is present. If in the absence of an applied field a small number of electrons at the Fermi surface is taken from the spin down band and placed spin-flipped in the spin up band, this costs energy and the whole process looks unfavourable. This situation is shown in figure 2.5b with δE being the energy range of the shifted and spin-flipped spin down electrons. However, the interaction of the magnetization with the molecular field reduces the energy leading to a ferromagnetic instability. Prerequisites for this instability are that the Coulomb effects (exchange processes) are strong enough and that the density of states at the Fermi energy is large. With U being the Coulomb energy, we can write

$$UD(E_F) \geq 1, \quad (2.9)$$

which is known as the **Stoner criterion** for ferromagnetism. If this criterion is not satisfied, spontaneous ferromagnetism will not occur. Only the elements Fe, Co, and Ni exhibit a value of $UD(E_F) > 1$, which is mainly caused by the large density of states directly at the Fermi energy. If the Stoner criterion is fulfilled a splitting of the spin up and spin down bands occurs without applying an external magnetic field.

Fe, for instance, possesses 8 valence electrons in $3d$ and $4s$ states. Different measurements [30] show that Fe has slightly less than one electron that can

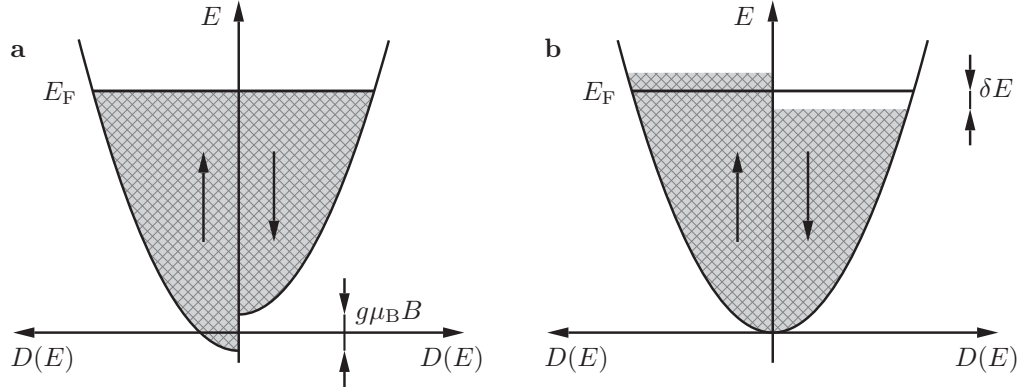


Figure 2.5: **a** Parabolic density of states for a free electron gas showing splitting of energy bands in an externally applied field B . The splitting of both bands amounts to $2\mu_B B$. **b** Density of states showing spontaneous spin splitting of energy bands without an applied magnetic field [29,30,42].

be called free or itinerant ($4s^{0.95}$). The remaining 7.05 electrons occupy the more localized $3d$ band. The number of d electrons with respect to each spin subband is therefore

$$n_{\uparrow} + n_{\downarrow} = 7.05. \quad (2.10)$$

The observed magnetic moment of $2.2 \mu_B$ per atom yields

$$n_{\uparrow} - n_{\downarrow} = 2.2. \quad (2.11)$$

Thus, we obtain that 4.625 of these 7.05 $3d$ electrons are spin up and 2.425 are spin down electrons.

Itinerant ferromagnetic order usually only happens in relatively narrow d -bands that are poorly delocalized. In general one can say that strong delocalization in a solid due to large overlap with neighboring wave functions tends to lead to pairing of spins and thus weak magnetism. This is why s - and p -type metals are all paramagnetic.

Metals with an exchange splitting smaller than the energy difference between the Fermi energy E_F and the top of the d -band are called weak ferromagnets. One example is Fe.

In summary magnetism in metals arises from the Coulomb repulsion between two electrons present on the same site. This repulsion acts to push away electrons that have antiparallel spins. An atom carries a magnetic moment, if Stoner's criterion is locally satisfied, that is, if the local density of states is larger than a certain critical value.

Anisotropy Effects

The local density of states strongly depends on the environment of the atom. Considering magnetic moments embedded in a ferromagnetic crystal, the total energy E_{mag} depends on the direction of the magnetization with respect to its crystal axes. This effect is the source of the **magnetocrystalline anisotropy energy** (MAE), E_{MAE} . It involves electrostatic crystal-field interaction and arises from spin-orbit-coupling (SOC). The spin-orbit interaction itself is, simply speaking, the dipole interaction of an electron spin with the magnetic field created by its orbital motion. SOC typically is much smaller than Coulomb and exchange interaction, depending on the electronic structure of the atom. For example, a high effective nuclear charge of inner electrons as within rare-earth atoms enhances the SOC. In transition metal compounds, the splitting of the crystal field favours the suppression (quenching) of orbital moments. In such solids, SOC has to compete against the splitting and this competition determines the degree of quenching and the magnitude of the magnetic anisotropy. $3d$ electrons tend to undergo strong quenching, for example, Fe has a magnetization of about $2.2 \mu_B$ (cf. chapter 2.1.1), but only about 5% of this moment is of orbital origin [31].

Adding an external magnetic field applied in a certain direction also induces an anisotropy because the **ZEEMAN-energy** has to be taken into account. The interaction of a magnetic moment \vec{m} with an external magnetic field \vec{H} is described by the energy

$$E_{\text{Zeeman}} = -\mu_0 \vec{m} \cdot \vec{H}, \quad (2.12)$$

where μ_0 is the magnetic field constant. The Zeeman energy favours spin alignment parallel to the external magnetic field.

Furthermore, the direction of magnetic moments in a ferromagnet depends on its shape. The resulting **shape anisotropy** energy can be considered as magnetostatic dipole interaction along the magnets surface. Typical magnetostatic anisotropy energies are much smaller than the MAE. However, the interaction is long range and, if many atoms are involved, it results in the formation of magnetic domains.

A kind of exchange anisotropy occurs in the presence of SOC, when the spins create orbital currents that interact with both the crystal field and with neighboring spins, hence changing the electrostatic energy of the electron. This **single-ion anisotropy** is the leading anisotropy mechanism in most magnetic materials.

Magnetoelastic anisotropy is caused by strain of a crystal's lattice. It is equivalent to the MAE, because a strained cubic lattice might as well be considered as an unstrained lattice, but with reduced symmetry. The main source of magnetoelasticity is magnetocrystalline single-ion anisotropy.

Surface and interface anisotropies are of particular importance in magnetic thin films and nanostructures. They occur on surfaces or at the interface

of two materials due to reduced symmetry, for example, due to surface roughness or lattice mismatch, respectively. Surface anisotropy is of magnetocrystalline origin, too: strength and symmetry of the anisotropy is determined by the interplay between crystal-field interaction and SOC.

A phenomenon related to single-ion anisotropy, surface and interface anisotropy is the exchange bias effect [43,44] at the interface between a ferromagnetic and an antiferromagnetic layer.

CHAPTER 3

ATOMIC FORCE MICROSCOPY AND SPECTROSCOPY

The atomic force microscope [7] detects (atomic) forces between a probe and a sample. A silicon tip mounted on a silicon cantilever (see figure 3.1) with spring constant c_z is used as force probe and scanned across the sample surface. Scanning is realized by piezoelectric tube scanners, moving the sample (or, as in other set-ups, the probe). The forces occurring between tip and sample lead to a mechanical response of the cantilever, detected by means of a laser interferometer (see chapter 4.1 for details). In the static mode simply the deflection of the cantilever is detected. Different dynamic modes, where the cantilever is deliberately vibrated during scanning, either detect the change in cantilever resonance frequency, phase or amplitude. AFM is a real-space imaging technique that reveals surface features such as terraces, islands and steps, that is, the topography. Height differences in atomically resolved images reflect variations of the magnitude of the atomic forces between the foremost tip atom and the surface atoms underneath. However, AFM data is always a convolution of sample topography and tip geometry. Hence, the lateral resolution of AFM is determined by the size of the interaction region and strongly depends on the sharpness of the tip. In order to properly evaluate AFM images, a rough knowledge of tip shape and dimension is inevitable (see chapter 8).

3.1 Principle of AFM

In this work only frequency modulation AFM (FM-AFM) [8] in the non-contact regime has been utilized. In FM-AFM, the cantilever oscillates self-excited at its resonance frequency f_0 with amplitude A . The oscillation signal is phase-shifted by 90° and fed back as excitation a_{exc} to the shaker piezo driving the oscillation. A feedback loop adjusts the excitation such that A remains con-

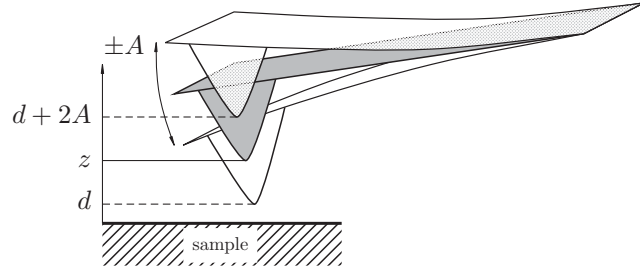


Figure 3.1: Sketch of the oscillating cantilever tip. The adjusted tip-sample distance z and the closest tip-sample distance $d = z - A$ are shown. Note that the sizes of tip and cantilever are not realistic. Typical dimensions are a tip height of $10\ \mu\text{m}$ with a tip radius of about $2\ \text{nm}$, while the cantilever beams have lengths of $225\ \mu\text{m}$ to $250\ \mu\text{m}$, widths of $38\ \mu\text{m}$ to $71\ \mu\text{m}$ and thicknesses of $7\ \mu\text{m}$ to $10\ \mu\text{m}$ [46].

stant (see figure 3.2). Thereby the tip-sample distance is not altered by changes in the oscillation amplitude, but by a shift of the resonance frequency of the unperturbed cantilever due to conservative tip-sample interactions, $\Delta f(z)$. If non-conservative forces occur between tip and sample, the energy loss has to be balanced by an increase of excitation energy to keep the amplitude constant. The actual frequency of the cantilever $f = f_0 - \Delta f$, is detected by a phase locked loop (PLL) [45]. In the constant Δf mode, the frequency shift is used as set-point (feedback) signal for surface scans and a piezo scanner adjusts the tip-sample distance accordingly. The voltage applied to the piezo scanner is interpreted as topography ($z(x, y)$ -map). An exemplary frequency shift versus distance curve as work curve of the topography-feedback is discussed in figure 3.8. A second method to scan the surface is the constant height mode, where z is kept constant, the topography-feedback is switched off, and a $\Delta f(x, y)$ -map is acquired.

3.2 Forces between Surface and Probe

All experiments presented in this work have been carried out in ultra high vacuum (UHV) utilizing metallic tips and samples. Therefore, this chapter is limited to vacuum forces between (magnetic) metallic surfaces and a probing tip. Later on the focus is put on atomic forces in close proximity to surface atoms.

When working in the dynamic mode where the cantilever is vibrated and a change in cantilever resonance frequency, phase or amplitude is detected due to some tip-sample interaction, but no energy is lost during approach and retract of a single cantilever oscillation cycle, the forces between tip and sample have to be considered as conservative. One common way to deal with conservative forces between probe and surface is a classification into long-range and short-range forces, depending on the distance dependence of the interac-

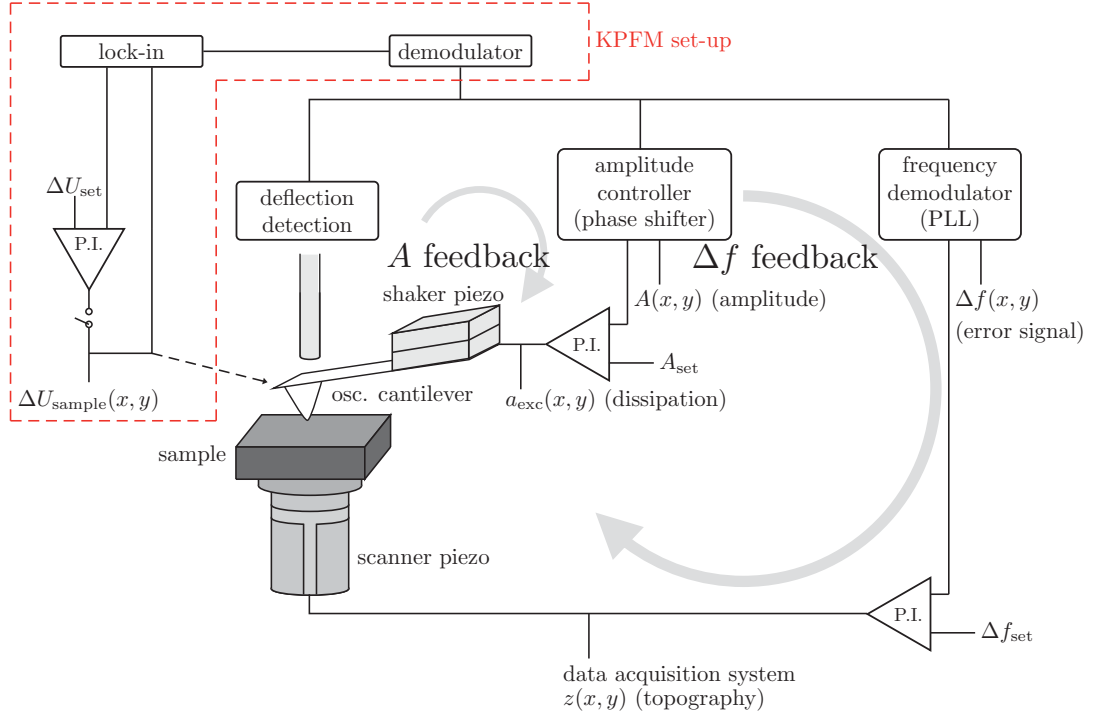


Figure 3.2: Working principle of FM-AFM and KPFM: an amplitude feedback keeps A constant, while the frequency shift feedback allows to scan the sample at constant frequency shift, Δf_{set} . Besides $A(x, y)$, frequency shift Δf , excitation $a_{\text{exc}}(x, y)$, and phase shift of the self excited oscillation, $\phi(x, y)$, are recorded. In red, the additional set-up needed to perform KPFM is sketched (cf. chapter 3.4).

tion potential. If the variation of the interaction potential is negligible on the scale of interatomic distances, the forces are called long-range forces. They decay over a distance range of several nanometers or tens of nanometers. If the variation is significant on atomic length scales, the force is called short-range. The following model system is used (figure 3.3a): a macroscopic probe of pyramidal shape ends in single atoms, referred to as foremost tip end. The ideal macroscopic sample surface is a flat plane, but we deal with single surface atoms within the microscopic range. Probe and sample are electrically connected, for instance, to apply a bias voltage U_{bias} . The total force in the non-contact regime between tip and sample is a superposition of long-range and short-range forces.

At small tip-sample separation repulsive forces, for example, hard sphere repulsion, Pauli-exclusion interaction and Coulomb interaction, start to dominate. Repulsive forces are very short-range and have an exponential decaying or inverse power law with higher order distance dependence. Different types of forces as sketched in figure 3.3b are discussed in the following.

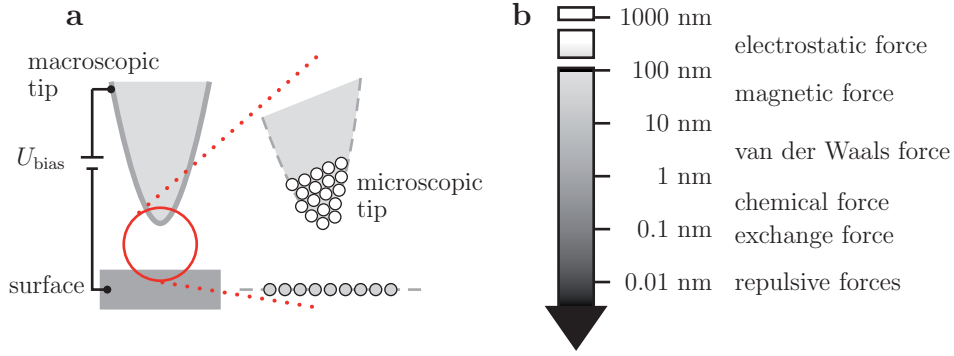


Figure 3.3: **a** Sketch of a macroscopically flat surface probed by a sharp tip, both electrically connected. At small separations the atomic structure of tip and sample become important. **b** By approaching the surface from a certain height in z -direction various distance dependent electromagnetic forces are detected.

Electrostatic Interactions

Within most metallic tip-sample systems it is very likely that tip and sample do have an electrostatic potential difference, leading to an electrostatic tip-sample interaction potential between tip and surface. This interaction potential is best evaluated in terms of the contact potential difference (CPD), cf. figure 3.4. If two metals with different work functions Φ_1 and Φ_2 are conductively connected electrons will flow from the metal with smaller work function to the metal with larger work function to equalize their Fermi levels. Thereafter, both metals are electrically charged. At small separations a capacitive electrostatic energy E_{cap} results [47]:

$$E_{\text{cap}} = \frac{1}{2}C(U_{\text{CPD}} - U_{\text{bias}})^2, \quad (3.1)$$

with C being the capacitance of the tip-sample system. This capacitive interaction can be nullified by applying a well set bias voltage $U_{\text{bias}} = U_{\text{CPD}} = (\Phi_1 - \Phi_2)/e$ that compensates for the CPD.

While in homogeneous systems the CPD between tip and sample materials can be balanced, it is impossible to nullify the electrostatic force everywhere in multi-component sample systems during scanning with one fixed bias voltage. Consequently, wrong heights are measured and constant force maps may exhibit apparent height differences, which are bias dependent [48–50]. Because the resulting capacitive force is proportional to ΔU^2 , sweeping ΔU results in a parabolic change of the tip-sample force that can be used to find the contact potential difference between tip and sample and to further characterize the tip. Local variations of electrostatic forces, for example, on multicomponent surfaces, can be imaged with Kelvin probe force microscopy (KPFM) (see chapter 3.4).

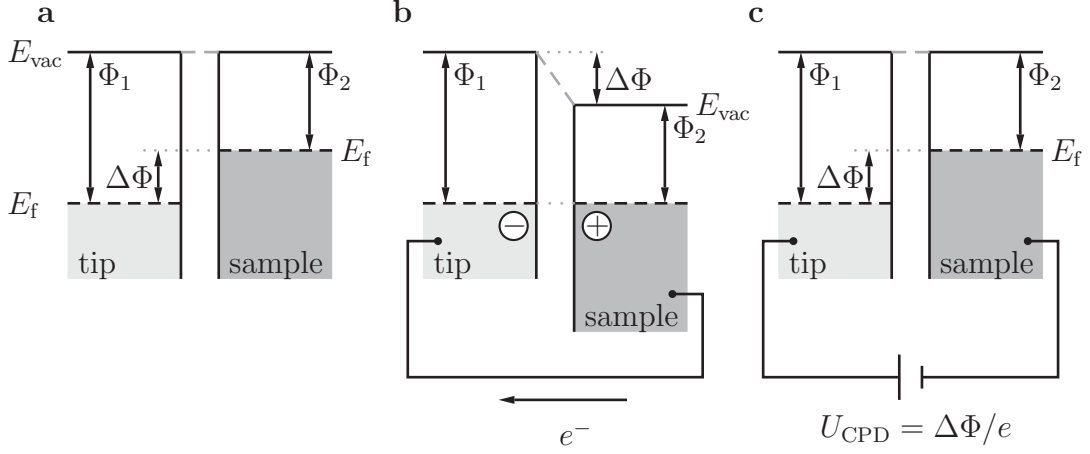


Figure 3.4: **a** Two metals, such as tip and sample, having different work functions Φ_1 and Φ_2 . **b** Conductively connected, chemical potentials are equalized by electrons flowing from the metal with smaller work function Φ_2 to the metal with larger work function Φ_1 . Thereafter, both electrodes are electrically charged. In a tip-sample configuration an attractive capacitive force can be detected. **c** Applying an appropriate bias voltage $U_{\text{bias}} = U_{\text{CPD}} = \Delta\Phi/e$ nullifies the capacitive force.

van der Waals Interactions

Fluctuations in the electric dipole moment of atoms and the polarization occurring thereafter within neighbouring atoms cause dispersive forces known as van der Waals forces. On atomic scale the very weak and always attractive van der Waals force is short-range with $1/r^6$ -dependence, while on macroscopic scale, that is, summing up over all interactions of individual atoms of macroscopic tip and sample, the van der Waals force is long-range and rather strong¹. For a spherical tip with radius R next to a flat surface the van der Waals potential can be written as [52]

$$E_{\text{vdW}} \propto -\frac{A_{\text{H}}R}{6z}, \quad (3.2)$$

with the distance between border of the sphere and surface z , and the material dependent Hamaker constant A_{H} . Van der Waals forces significantly depend on the macroscopic geometry in close vicinity to the probe apex and it is thus often not possible to estimate the real van der Waals interaction potential between probe tip apex and sample [53].

Magnetostatic Interactions

Long-range magnetostatic interactions play a crucial role, when tip and sample are ferromagnetic. In this case, the magnetic field \vec{H}_{tip} emanating from the

¹The strength of the van der Waals forces may dominate the tip-surface interaction in many cases [51].

tip interacts with the magnetic polarization \vec{J}_{sample} from the surface (and vice versa). The resulting magnetostatic interaction energy is given by

$$E_{\text{mag}} = - \int_{\text{tip}} \vec{J}_{\text{sample}} \cdot \vec{H}_{\text{tip}} dV. \quad (3.3)$$

This interaction is utilized in magnetic force microscopy (MFM) to image the domain structure of ferromagnetic samples (see chapter 3.4). Strength and range of the magnetostatic interaction strongly depend on tip (geometry of the tip magnetization) and sample configuration and might vary locally. Hence, measuring the corresponding magnetostatic force allows to image the domain structure of ferromagnetic samples. However, as identical stray fields above a surface can be a result of different magnetic configurations of tip and sample, interpretation of MFM measurements is not unambiguous.

Magnetic Exchange Interactions

In the case of tip and sample being magnetic and in very close proximity on the order of some hundred pm, a spin dependent exchange force has to be considered. As introduced in chapter 2.1.1, this force is due to the exchange between two magnetic moments, in an ideal fashion between the moments of foremost tip atom and surface atom underneath. For two spin carrying atoms i and j , the exchange energy can be written as

$$E_{\text{ex}} = -2J\vec{S}_i \cdot \vec{S}_j, \quad (3.4)$$

with J being the effective exchange integral² and \vec{S}_i and \vec{S}_j being the atom spins. Exchange forces occur only on atomic length scales and are much stronger than any magnetostatic interaction. Utilizing these forces to map spin structures with atomic resolution and measuring the distance dependence of this force experimentally is the main topic of this thesis.

Chemical Interactions

While long-range forces between probe and sample originate in full volume and surface of the macroscopic tip and are a critical function of tip shape, short-range forces involve mainly the tip apex, in an ideal case only the foremost tip atom sensing the surface atoms underneath. Hence, chemical forces only act, when the orbitals of foremost tip atom and sample atoms start to overlap.

Following the description for the covalent bond between two hydrogen atoms the interaction potential can be described by a MORSE potential [54], which is an exact solution of the SCHRÖDINGER equation:

$$E_{\text{Morse}}(r) = E_0 \left(e^{2\alpha(r_0-r)} - 2e^{\alpha(r_0-r)} \right), \quad (3.5)$$

²The exchange integral has been derived in chapter 2.1.1, eq. 2.7.

with E_0 being the bonding energy, r_0 the equilibrium distance and $\alpha = \sqrt{k_e/2E_0}$ the decay length. k_e is the force constant of the oscillation of the two atoms at equilibrium distance.

If not chemical interactions but short-range van der Waals forces or dipole interactions are dominant, the potential between tip and sample atom can be described by the LENNARD-JONES potential [55]

$$E_{\text{LJ}}(r) = -E_0 \left(2 \left(\frac{r_0}{r} \right)^6 - \left(\frac{r_0}{r} \right)^{12} \right). \quad (3.6)$$

The first term includes the attractive van der Waals force, while repulsive forces (second term) set in with decreasing tip-sample distance, as described by the MORSE potential.

3.3 Dissipation of Energy

As soon as the deliberately vibrated cantilever loses energy on approach and retract of a single cantilever oscillation cycle, non-conservative (or dissipative) tip-sample forces play a crucial role, and additional energy has to be invested to keep the cantilever oscillation alive. Friction for instance, that depends on time and velocity, is a non-conservative force that appears in close contact of tip and sample. Other dissipative processes might occur as well, for example, if energy is lost into vibrations of atomic junctions at the tip apex or of surface atoms.

The dissipation of energy into the tip-sample system can be deduced from the excitation signal recorded simultaneously with topography, amplitude and frequency shift during imaging and spectroscopy. In FM-AFM, the measured dissipation is averaged over many oscillation cycles. Far away from the sample $a_{\text{exc},0}$ compensates for intrinsic losses, since the cantilever is partially damped due to intrinsic friction mechanisms, related to its macroscopic quality factor $Q := \frac{2\pi f_0}{\gamma_0}$, with γ_0 being the intrinsic damping coefficient. The quality factor, which is influenced by cantilever material, geometry of the cantilever base and thermomechanical properties of coatings, is determined from the width of the cantilever resonance curve, $Q \approx \frac{f_0}{|f_1 - f_2|}$. The intrinsic loss of energy per oscillation cycle can be expressed as

$$E_0(A) = \frac{\pi c_z A^2}{Q}. \quad (3.7)$$

Quantitatively, the energy dissipation per cantilever oscillation cycle is obtained relative to intrinsic losses by using the general formula derived in [56,57]:

$$P_D = P_{\text{in}} - P_0 = \frac{\pi c_z f}{Q} (Q a_{\text{exc}} A \sin \varphi - A^2 \frac{f}{f_0}), \quad (3.8)$$

where P_{in} , P_0 and P_{D} , are the power fed into the cantilever oscillation, the intrinsic loss of the cantilever and the dissipated power due to the non-conservative tip-sample interaction, respectively. For the self excitation FM-AFM mode with constant amplitude used here, the phase is $\varphi = 90^\circ$, f equals f_0 and $A = Q \cdot a_{\text{exc},0}$ far away from the surface where $P_{\text{in}} = P_0$. Further, the dissipated energy per oscillation cycle is given by $E_{\text{D}} = P_{\text{D}} \cdot f_0^{-1}$, hence

$$E_{\text{D}} = \frac{\pi c_z A^2}{Q} \left(\frac{a_{\text{exc}}}{a_{\text{exc},0}} - 1 \right). \quad (3.9)$$

The dissipation data presented in this work, either obtained during imaging or $\Delta f(z)$ -spectroscopy, are calculated following eq. 3.9 and hence show the energy dissipated per oscillation cycle given in eV.

While conservative forces lead to a distance dependent shift of the resonance frequency, non-conservative (or dissipative) forces result in a distance dependent increase of the excitation, $a_{\text{exc}}(z)$ [58]. Several mechanisms leading to non-conservative forces and explaining an additional energy dissipation on the atomic scale exist, but it is not straightforward to relate the measured damping of the cantilever to the different origins of dissipation. Many effects of dissipation are not understood, yet. Moreover, besides true dissipation, different mechanisms leading to apparent damping exist and most experimental data do not allow an unambiguous assignment of the underlying mechanism.

3.3.1 Apparent Damping

It has been suggested that dissipation is an artefact of the response of a not-well adjusted amplitude regulator [59]: as the amplitude regulator has limited response time, in the range of a millisecond, the excitation may not be exactly out of phase with the cantilever oscillation, $\varphi \neq 90^\circ$. This results in an atomic-scale change of the excitation and thus in an apparent damping signal observable as atomic scale contrast in the excitation during imaging. By simulating an experiment using typical experimental parameters, it has been shown that the contrast in the excitation channel due to apparent damping is typically less than 1 meV/cycle, which is much too small to account for most experimental observations [60].

Another apparent damping mechanism might originate from an inharmonic cantilever-motion [61]: the equation used to calculate the total tip-sample interaction is only valid for harmonic motion, but as soon as tip and sample start to interact, the motion of the cantilever becomes slightly non-harmonic. In consequence, a part of the oscillation energy is stored in overtones of the cantilever frequency and the phase controller increases the measured excitation amplitude, although the interaction might be still conservative.

Moreover, crosstalk between topography and dissipation channel might also lead to apparent damping: during constant frequency shift imaging the tip-sample distance is varied to keep the interaction constant. This change might

lead to an atomic scale signal in the excitation, as the dissipation is distance dependent [62]. This artifact due to the z -feedback cannot be excluded experimentally, except when the distance feedback is switched off, for example, during constant height imaging. However, the dissipation only depends on tip-sample distance, when true non-conservative channels exist. If the energy loss varies on the atomic scale, the underlying mechanism is also sensitive to atomic details [62]. Hence, crosstalk reflects true mechanisms, enhanced by the variation of the tip-sample distance on atomic scale.

3.3.2 Dissipation Mechanisms

Besides apparent damping, several mechanisms have been proposed to explain true dissipation processes. While a detailed review of dissipation phenomena in FM-AFM can be found in [61], the most prominent mechanisms shall be shortly discussed. They can be classified into velocity-dependent and hysteresis-related mechanisms.

Velocity Dependent Dissipation

One example for velocity-dependent dissipation is Joule dissipation [63]. The dissipation occurs, when the tip-sample capacitance is charged and discharged, driven by the time-varying electric field produced by the tip oscillation. However, this effect only accounts for dissipation, when tip and sample are not perfect conductors.

Hysteresis Related Dissipation

At tip-sample distances below 1 nm, hysteresis related mechanisms have been identified as the most relevant non-conservative dissipation channels. The energy loss involved is found to be at least on the order of chemical binding energies [60, 64–68] and, hence, much larger than other true and apparent damping mechanisms. In the case of tip instabilities, atoms reconfigure during every oscillation cycle at the tip apex with a different path during forward and backward oscillation. The structurally reversible but statistically irreversible motion of the apex atoms between different energy minima is changing the atomic configuration in the tip-sample junction. The motion leads to hysteresis and hence to loss of energy.

That the microscopic system of tip and sample is able to move between two minima on the potential energy surface was already derived in 1993 [69] and further discussed in many publications within the scope of adhesion hysteresis [62, 64, 70, 71]. The hysteretic movement has also been found by dynamic simulations [65, 72] and in other modelling [73–75]: the derived double-welled potential energy surface is due to the merging of tip and surface potentials at the onset of the tip apex atom forming a chemical bond with the surface

(adhesion). However, in some cases the energy barrier between the minima might not disappear or become low enough upon tip retraction and the atom does not return to the tip or vice versa. In this special case the atom will be permanently pulled away, resulting in a tip modification.

Different to the findings of GHASEMI [66] where only pure Si tips were considered, the metal atoms at the tip apex used in this study are not able to form covalent bonds. Hence, frustrated tip structures facilitating hysteretic atomic rearrangements of the tip atoms do not occur. However, as more than only one tip atom can be involved, rearrangements of atomic clusters with respect to each other and, thus, discrete rearrangement of the tip apex with respect to the tip base might show up at certain distances, as soon as the short-range interactions are sufficiently strong to modify the local potential energy landscape of tip and sample.

Experimentally the effects of apparent damping on the dissipation can be minimized by properly adjusting the feedback circuits. Though crosstalk might still play a crucial role, hysteretic motion of atoms in combination with unstable tip apices is considered as the driving mechanism leading to the dissipation presented in chapter 8.

3.4 Imaging Modes

Different AFM techniques covering different types of applications do exist. Besides AFM which is used for structural analysis of the sample surface and to obtain atomic resolution, Kelvin probe force microscopy and magnetic force microscopy are used to study electrostatic and magnetostatic properties, respectively. Magnetic exchange force microscopy is used to map single spins on the surface.

Kelvin Probe Force Microscopy

The FM-AFM based KPFM [76] is widely used to acquire the work function of surfaces, even at atomic or molecular scales [47–49]. Determining the work function of conducting tips and samples is achieved by measuring the electrostatic forces between tip and sample. Applying a voltage between tip and sample, consisting of a DC-voltage U_{dc} and a modulated voltage $U_{\text{ac}} = U_{\text{mod}} \sin(2\pi f_{\text{mod}} t)$, the electrostatic force according to eq. 3.1 becomes

$$\begin{aligned} F_{\text{el}} &= \frac{1}{2} \frac{\partial C}{\partial z} U^2 \\ &= \frac{1}{2} \frac{\partial C}{\partial z} (U_{\text{dc}} - U_{\text{CPD}} + U_{\text{mod}} \cos(2\pi f_{\text{mod}} t))^2 \end{aligned} \quad (3.10)$$

Tuning the frequency of the AC-voltage to the second resonance frequency of the cantilever results in an improved sensitivity and allows the independent

and simultaneous imaging of topography and contact potential. As a result of the biasing conditions an oscillating electrostatic force appears, inducing an additional oscillation of the cantilever with the characteristic frequency f_{mod} . Hence, F_{el} can be further written as

$$\begin{aligned} F_{\text{el}} = & \frac{1}{2} \frac{\partial C}{\partial z} (U_{\text{dc}} - U_{\text{CDP}} + \frac{1}{2} U_{\text{mod}}^2) \\ & + \frac{\partial C}{\partial z} (U_{\text{dc}} - U_{\text{CDP}}) U_{\text{mod}} \cos(2\pi f_{\text{mod}} t) \\ & + \frac{1}{4} \frac{\partial C}{\partial z} U_{\text{mod}}^2 \cos(4\pi f_{\text{mod}} t). \end{aligned} \quad (3.11)$$

The 2nd term with the characteristic frequency f_{mod} is used to measure the contact potential and a lock-in amplifier is needed to detect the cantilever oscillation at f_{mod} . During scanning U_{dc} is adjusted so that the electrostatic force between tip and sample becomes zero and thus, the response at the oscillation frequency f_0 becomes zero, and, at the same time, the response at frequency f_{mod} becomes maximum. Since the electrostatic force at f_{mod} depends on $U_{\text{dc}} - U_{\text{CPD}}$, U_{dc} corresponds to the contact potential. Apart from that, one can use the normal topographic scan methods at the resonance frequency f_0 independently of the above. Thus, in one scan, the topography and the contact potential of the sample are determined simultaneously. The used KPFM mode is known as frequency-modulated mode, FM-KPFM. A good comparison between FM-KPFM and AM-KPFM, where the amplitude and not the frequency of the oscillation is detected and tuned to zero by a lock-in amplifier, can be found in [77].

Magnetic Force Microscopy

In MFM, magnetic dipole forces are probed with magnetic tips at a typical tip-surface distance of $h = 10 - 20$ nm [14, 78, 79]. Since the tip (sample) should exhibit a stray-field pointing along a specific direction³, MFM is sensitive to the component of the magnetic stray field of sample (tip), which is aligned within the same direction. Knowing the magnetic properties of the tip, for example, allows to gain insights into the magnetism of the probed sample. As most sample surfaces have a miscut, it is common to use MFM in the plane-subtraction mode described in [79] and shown in figure 3.5: using FM-AFM the topography of the sample, figure 3.5a, is obtained with compensated slope, figure 3.5b. Thereafter, the feedback is switched off, and the tip is retracted up to a certain height h . An MFM image is obtained by recording Δf within the plane at a specific constant height, where it is dominated by long-range electrostatic and magnetostatic forces, figure 3.5c. The contribution of the electrostatic component is minimized by applying an appropriate bias voltage compensating for the CPD. The resolution limit for MFM is on the order of a

³This can be realized by *in situ* coating the side faces of a pyramidal tip [80].

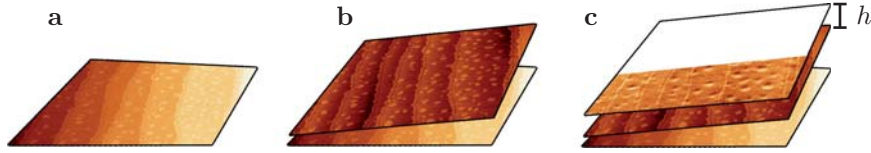


Figure 3.5: Sketch of the plane subtraction mode. After having recorded the topography in **a**, in **b** the slope of the sample is compensated and the tip is retracted. **c** Scanning in constant height mode is typically performed at a distance of $h = 10 - 20$ nm. [80].

few nm. This limit partly arises from the relatively large tip-surface distances used in MFM and the long decay length of the magnetic stray field probed at these distances.

Magnetic Exchange Force Microscopy

In contrast to MFM, it is expected that at smaller tip-sample distances, exchange forces lead to atomic scale magnetic contrast. Hence, with the FM-AFM based magnetic exchange force microscopy (MExFM) [9] magnetic nanostructures are mapped with atomic resolution combined with a sensitivity to single spins by using a probe with magnetically sensitive tip end. By this, MExFM allows to reveal the local energy difference of spins located in the sample surface. The measured atomic scale contrast is expected to be dominated by electron mediated and short-range exchange forces, that is, tip and sample are at close distance where the orbitals of foremost tip atom and sample atoms do overlap. According to the Heisenberg exchange, collinear alignment of tip and probed sample spins should lead to largest exchange energy and hence largest corrugation amplitude.

3.5 Spectroscopy Modes

In FM-AFM different spectroscopic methods can be utilized. In contrast to imaging, spectroscopy allows to precisely measure tip-sample interaction forces across a vacuum gap in point mode, hence, without scanning. The methods are used, for example, to characterize tip and surface, to measure the distance dependent tip-sample interaction strength, or to measure the distance dependent energy loss within single cantilever oscillation cycles.

3.5.1 Bias Spectroscopy

To minimize electrostatic forces, the bias voltage during scanning should balance the CPD between tip and sample. Experimentally, U_{CPD} can be determined by recording $\Delta f(U_{\text{bias}})$ -curves. Here, the frequency shift is stabilized

at a fixed value Δf_{stab} above a certain point of the sample surface and the feedback loop, that keeps Δf constant for imaging, is switched off. While ramping the bias voltage within a specified interval, the variation of Δf is recorded. Since the capacitive force is proportional to ΔU^2 according to eq. 3.1, a parabolic shaped $\Delta f(U_{\text{bias}})$ -curve is expected with $U_{\text{bias}} = U_{\text{CPD}}$ at its apex. If the used tip is not perfectly conductive, hysteresis and jumps within the spectroscopy curves do occur. Hence, $\Delta f(U)$ -spectroscopy can be further used to characterize the tip.

3.5.2 Force Spectroscopy

$\Delta f(z)$ -curves reflect the total tip-sample interaction force within the probed z -range. They can be converted into force curves, $F(z)$ (cf. chapter 3.6), hence, they allow to directly measure the distance dependence of the interaction strength between tip and sample above a certain point.

Data Acquisition

$\Delta f(z)$ -spectroscopy curves as presented in figure 3.6 can be acquired differently: the stabilization frequency, that is, the starting point of the spectroscopy, can be chosen either close to the surface, $\Delta f_{\text{stab}}(\text{i})$, or far away from it, $\Delta f_{\text{stab}}(\text{ii})$. In such, the z -piezo is either retracting from the surface or approaching the surface, respectively. Both methods will qualitatively and quantitatively lead to the same result. While the step width is adjustable, no absolute z -scale can be extracted from experimental data, that is, $z = 0$ pm is arbitrarily set as closest tip-sample distance (cf. figure 3.8).

Method (i)

Sketched in figure 3.6, the tip-sample distance is stabilized at $\Delta f_{\text{stab}}(\text{i})$ close to the surface, where an atomic contrast is observed (green dotted line), as verified by a control image shown in figure 3.6b. The corresponding z_{start} -position of the spectroscopy, affected by the atomic corrugation, is recorded before moving the z -piezo. Only thereafter, the z -feedback is switched off and the tip is retracted in z -direction from the stabilization position up to a certain distance z_{end} with step size Δz while recording $\Delta f(z)$ data (green solid arrow). After sweeping z , the feedback is switched on and the tip is again approaching the stabilizing frequency at z_{start} without data being obtained.

Method (ii)

Sketched in figure 3.6, the tip-sample distance is stabilized at $\Delta f_{\text{stab}}(\text{ii})$ far away from the surface where short-range interactions, for example, chemical and magnetic exchange, no more contribute to the obtained contrast (dark red dotted line), as verified by a control image, shown in figure 3.6c. The

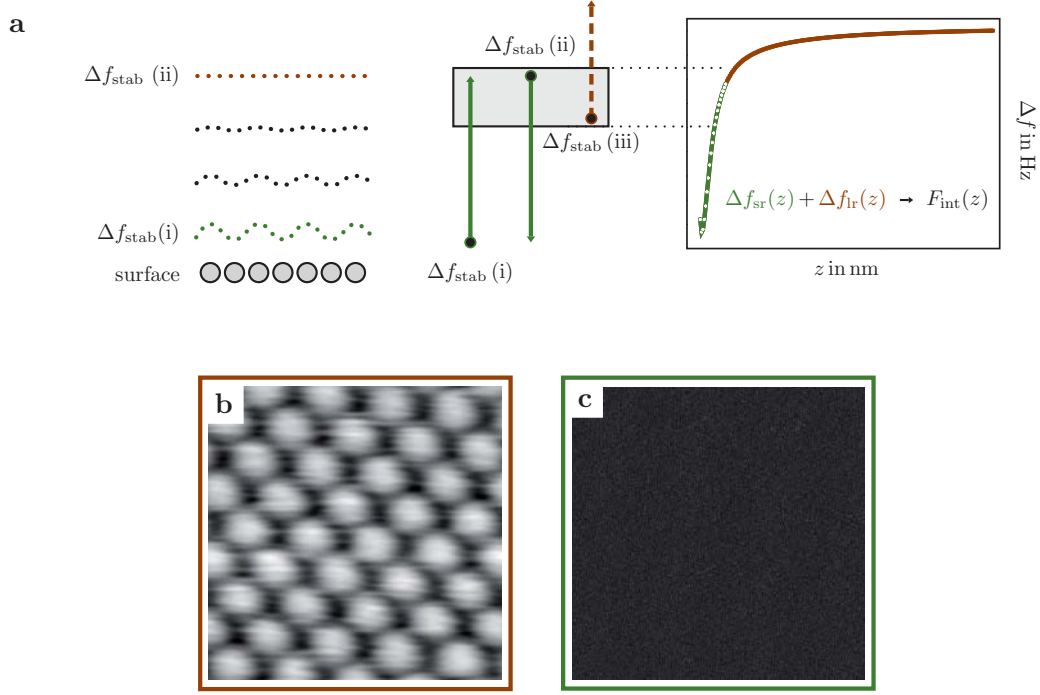


Figure 3.6: **a** Data acquisition scheme. **b** Atomic resolution obtained at $\Delta f_{\text{stab}}(i)$. **c** Topography far away from the surface where short-range interactions do not contribute to the contrast, obtained at $\Delta f_{\text{stab}}(ii)$. The images are used prior to any spectroscopy to judge on tip stability and to allow for selecting a suitable stabilization frequency for either method.

corresponding z -position is recorded, the z -feedback is switched off and the tip is approached in z -direction from the stabilizing position z_{start} down to a certain distance z_{end} with step size Δz while recording $\Delta f(z)$ data. Thereafter, the z -feedback is switched on and the tip is again approaching the stabilizing frequency at z_{start} without data being obtained.

3D-Force Field Spectroscopy

To obtain individual, site specific curves, which can be assigned with unambiguity to certain positions on the atomic lattice, it is useful to perform the spectroscopy in a 3D fashion (3D-Force Field Spectroscopy, 3D-FFS). Here, the procedure of choice, either (i) or (ii), is repeated on all $(m \times m)$ spectroscopy points in the xy -plane and the resulting $3D-\Delta f(x, y, z)$ data set represents the total tip-sample interaction. By this, a map of atomic forces can be obtained three-dimensionally with atomic resolution [18, 81].

The time to acquire a field of, for example, (128×128) spectroscopy curves with a step width of $\Delta z = 1$ pm over a z -range of 300 pm can easily take up to several hours. Therefore, a stable system and measuring at low temperatures

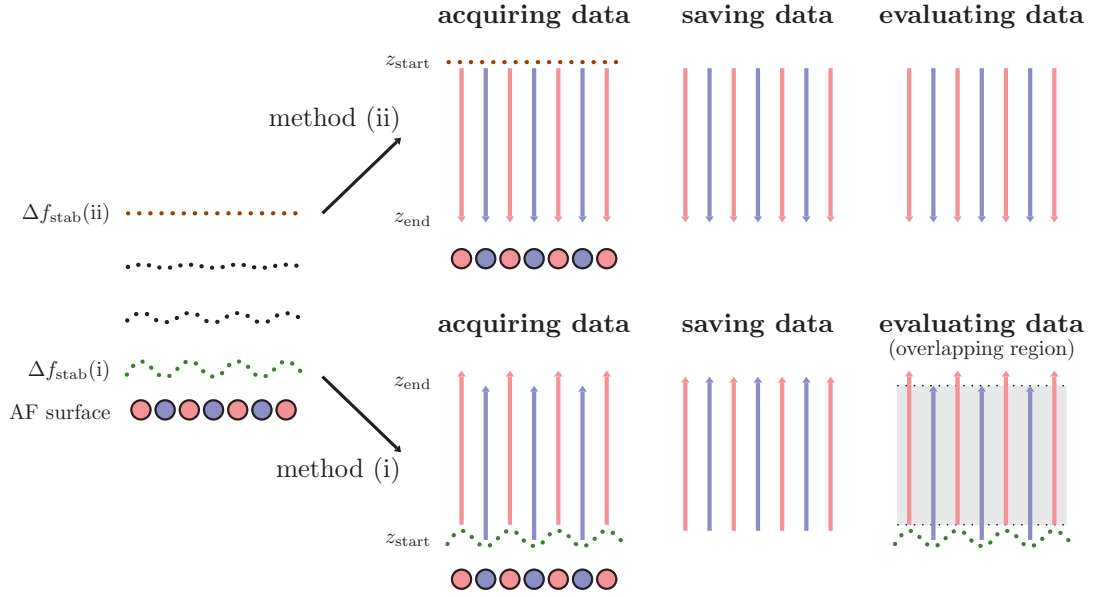


Figure 3.7: Data evaluation scheme. Data acquired using method (ii) can be directly analyzed, while method (i) requires an additional step to adjust the z -scale correctly.

are helpful to avoid piezo creep and temperature dependent drift effects during data acquisition.

If, however, not only short-range, but also long-range interactions are of interest, an additional long-range curve is recorded such that data points within the long-range curve (dark red in figure 3.6) and short-range curves (green in figure 3.6) do overlap, that is, within the rectangle sketched in figure 3.6, where $\Delta f_{\text{stab}}(\text{iii}) < \Delta f_{\text{stab}}(\text{ii})$. The long-range curve is not site-specific and can be acquired on a shorter time scale with larger step-width than the short-range curves. Thereafter, the long-range curve can be added to every single short-range curve, $\Delta f_{\text{sr}}(z) + \Delta f_{\text{lr}}(z)$, and the total interaction F_{int} is obtained site specific over a long tip-sample distance range.

Magnetic Exchange Force Spectroscopy

The spectroscopic mode of MExFM, that is, atomic resolution and precise distance dependent measurements of tip-sample forces by means of $\Delta f(z)$ -curves combined with spin sensitivity, is referred to as **magnetic exchange force spectroscopy** (MExFS). Recording a 3D-data set with atomic resolution on, for example, an antiferromagnetic surface exhibiting parallel and antiparallel oriented magnetic moments with respect to the tip magnetization, allows to extract individual curves recorded on well defined atomic sites. Hence, $\Delta f_{\text{ap}}(z)$ on an antiparallel, and $\Delta f_{\text{p}}(z)$ on a parallel oriented moment, respectively, can be unambiguously identified and extracted.

Both curves contain the full tip-sample interaction. However, non-site specific long-range interactions, like the van der Waals interaction, and the chemical interaction are the same on chemically identical surface atoms. Due to the supposed antiferromagnetic structure of the surface, the curves differ only by the magnetic exchange interaction between single atoms with oppositely oriented moments. Hence, the contribution due to exchange, represented by $\Delta f_{\text{ex}}(z)$, is elegantly obtained by subtracting both curves from each other:

$$\Delta f_{\text{ex}}(z) = \Delta f_{\text{ap}}(z) - \Delta f_{\text{p}}(z). \quad (3.12)$$

Whichever acquisition method, either (i) or (ii), is chosen, the real starting point of the obtained curves is not stored properly by the data acquisition software [82]. While the starting point using method (ii) is the same for all curves, see figure 3.7, such a data set can be directly evaluated according to eq. 3.12.

The subsequent evaluation of a data set obtained using method (i) requires some additional steps, see figure 3.7. Here, the atomic corrugation has to be considered, that is, a shift of the z -scale of all $\Delta f(z)$ -curves is necessary to evaluate the curves relative to each other. The shift-value is obtained from the value of z_{start} , recorded for every curve. The 2D matrix containing all start values hence represents the topography. As only the overlapping regions of the data can be subtracted, method (i) results in loss of data points. Furthermore, the first few data points close to the surface have to be cut off due to piezo hysteresis effects (creep), when the time constant for the tip to stabilize at z_{start} after a spectroscopy curve has been recorded is not chosen properly.

However, method (i) has one major advantage: the maximum frequency shift up to which stable imaging of the magnetic contrast is possible is already obtained whilst imaging in MExFM mode as $\Delta f(z_{\text{start}}) = \Delta f_{\text{stab}}$ (cf. figure 3.6b) and when acquiring single curves, the tip is usually not approached beyond this value, but retracted along z , hence the tip state is secured. In contrast, the total z -range in which single curves can be acquired whilst approaching the surface from Δf_{stab} down to $\Delta f(z_{\text{end}})$ is not known with unambiguity when using method (ii). Here, the available z -range has to be approximated step-wise by means of single $\Delta f(z)$ -curves before a $(m \times m)$ -spectroscopy field can be recorded. This has to be done carefully, as a sudden tip crash during a too close approach may happen and irreversibly destroy the tip state (cf. chapter 8).

3.5.3 Dissipation Spectroscopy

Hitherto, the presented spectroscopic methods only allow for measuring conservative tip-sample forces. To gain insight into non-conservative tip-sample interactions and to understand the origin of dissipation occurring in FM-AFM experiments, it is useful to measure the dissipation as a function of tip-sample

distance. To do so, the excitation amplitude, $a_{\text{exc}}(z)$, used to keep the oscillation amplitude A constant, is measured in dependence of the distance. This is done simultaneously with force spectroscopy by utilizing the presented methods. The dissipation can be derived from the excitation as presented in chapter 3.3.

3.6 Frequency Shift to Force Conversion

To obtain forces or energy (for example, the magnetic exchange energy) from the recorded frequency shift, $\Delta f(z)$ ($\Delta f_{\text{ex}}(z)$) has to be converted. Several approaches towards a conversion algorithm have been made by GOTSMANN [83, 84], DÜRIG [85], HÖLSCHER [58, 86], GIESSIBL [87, 88] and SADER [89]. The used algorithms are discussed in the following. With the pre-condition $\Delta f \ll f_0$ amongst others DÜRIG [85] and GIESSIBL [87] find

$$\Delta f(z) = \frac{f_0}{\sqrt{2}\pi c_z A^{3/2}} \int_d^\infty \frac{F(z)}{\sqrt{z-d}} dz, \quad (3.13)$$

with tip-sample distance z and distance at the lower turnaround point of the tip d , as visualized in figure 3.1.

Figure 3.8a shows an analytically derived force versus distance curve and its related frequency shift versus distance curve in **b**. The force curve reflects long-range van der Waals plus short-range forces described by a Lennard-Jones potential [90]. As theoretical parameters $f_0=190$ kHz, $c_z=140$ N/m and $A=3$ nm have been used. The van der Waals force is calculated using $A_H = 0.2$ aJ and a tip radius of 2 nm. The Lennard-Jones force has been added using a binding energy of $E_0 = 1$ eV and an equilibrium distance of 0.3 nm. These parameters are typical parameters in the experiments presented in the forthcoming chapters. The curves are calculated within a range of 0 nm to 2.2 nm tip-sample separation. The frequency shift does not vary monotonically with distance, but changes its sign roughly on the repulsive branch of the tip-sample interaction force, that is, on the left side of the force minimum in figure 3.8f, indicated as z_{min} by the red dotted line. A negative Δf slope corresponds to attractive tip-sample forces, while a positive slope indicates the presence of repulsive forces. Note that the $\Delta f(z)$ -relationship is not directly proportional to the force, but its shape reflects the same general distance dependence: Δf as well as the force between tip and sample is zero for infinite large distances, becomes negative at smaller distances due to the presence of attractive long- and short-range interactions and finally gets positive, when short-range repulsive interactions dominate.

An analytical inversion of eq. 3.13 is not possible and numerical solutions have to be used instead.

$\Delta f(z)$ can be integrated using the DÜRIG [85] approach as follows

$$F(d) = \sqrt{2} \frac{c_z A^{3/2}}{f_0} \frac{\partial}{\partial d} \int_d^\infty \frac{\Delta f(z)}{\sqrt{z-d}} dz. \quad (3.14)$$

Here, the normalized frequency shift $\gamma(z)$ can be introduced, as Δf depends not only on z , but on the external parameters A , c_z and f_0 as well [87]:

$$\gamma(z) = \frac{c_z A^{3/2}}{f_0} \Delta f(z). \quad (3.15)$$

The normalized frequency shift allows to compare frequency shifts obtained with different experimental variables such as oscillation amplitude and cantilever stiffness. The ansatz presented by DÜRIG in eq. 3.14 might lead to errors due to non-neglectable long-range interactions. Another approach is presented by SADER [89] using a LAPLACE-transformation prior to any approximations. With $\Omega(z) = \Delta f(z)/f_0$ the integral of $\Delta f(z)$ is

$$F(d) = 2c_z \int_d^\infty \left(1 + \frac{\sqrt{A}}{8\sqrt{\pi(z-d)}} \right) \Omega(z) - \frac{A^{3/2}}{\sqrt{2(z-d)}} \frac{d\Omega(z)}{dz} dz. \quad (3.16)$$

A simple and intuitive matrix method to deconvolute the frequency shift has been proposed by GIESSIBL in 2001 [88]: the force can be calculated by using the matrix $\mathbf{W}' = (w'_{ij})$ with the elements

$$w'_{ij} = \begin{cases} \frac{f_0}{\pi c_z A} \int_{1-[2(i-j+1)]/[(2\alpha+1)]}^{1-[2(i-j)]/[(2\alpha+1)]} (\tau/\sqrt{1-\tau^2}) d\tau & \text{for } 0 \leq i-j \leq 2\alpha \\ 0 & \text{else} \end{cases}, \quad (3.17)$$

where $\alpha = \text{round}(A/\Delta)$ with Δ being the step width of the z -scale and with $F_i = F_i(z_{i+\alpha})$:

$$\begin{pmatrix} F_1 \\ F_2 \\ \dots \\ F_N \end{pmatrix} = \mathbf{W}'^{-1} \cdot \begin{pmatrix} \Delta f_1 \\ \Delta f_2 \\ \dots \\ \Delta f_N \end{pmatrix} = \begin{pmatrix} w'_{11}{}^{-1} & 0 & \vdots & 0 \\ w'_{21}{}^{-1} & w'_{22}{}^{-1} & \vdots & 0 \\ \dots & \dots & \ddots & \dots \\ w'_{N1}{}^{-1} & w'_{N2}{}^{-1} & \vdots & w'_{NN}{}^{-1} \end{pmatrix} \cdot \begin{pmatrix} \Delta f_1 \\ \Delta f_2 \\ \dots \\ \Delta f_N \end{pmatrix}. \quad (3.18)$$

A direct comparison of the introduced approaches using the analytically derived $F(z)$ -curve as input is shown in figure 3.8. Using the existing Δf -to- F conversion algorithms derived by GIESSIBL, DÜRIG and SADER force and energy are re-calculated from the analytical Δf -curve, plotted in figure 3.8c and **d**, respectively. The presented methods show quantitatively and qualitatively the same result with deviations from the analytically derived force curve of

only a few tenth nN, as plotted in figure 3.8f. The energy curves are compared in figure 3.8g. While $\Delta f(z)$, $F(z)$, and $E(z)$ show comparable trends, they differ quantitatively and the minima are not at the same positions.

As during the data acquisition some several thousand curves are recorded, an accurate and fast automation method has to be found to be able to evaluate the data in acceptable time. This has been achieved using MATLAB [91], which handles huge matrices efficiently. Fastest deconvolution is achieved using the matrix method by GIESSIBL [88]. However, a bad signal-to-noise ratio (SNR) of single Δf -curves will lead to large noise within the calculated force. When further integrating the force to get the energy data, this noise leads to an overestimation of the energy within the regime where $F \approx 0$. Hence, the DÜRIG algorithm is applied when evaluating single curves. Here, the energy is directly calculated using the normalized frequency shift γ . As the integration is sensitive to noise anyway, it is, for example, possible to average over all p- and ap-sites present in a 3D-MExFS data set prior to the conversion. Furthermore, $\Delta f(z)$ -curves might be smoothed or fitted with an analytical expression before the integration.

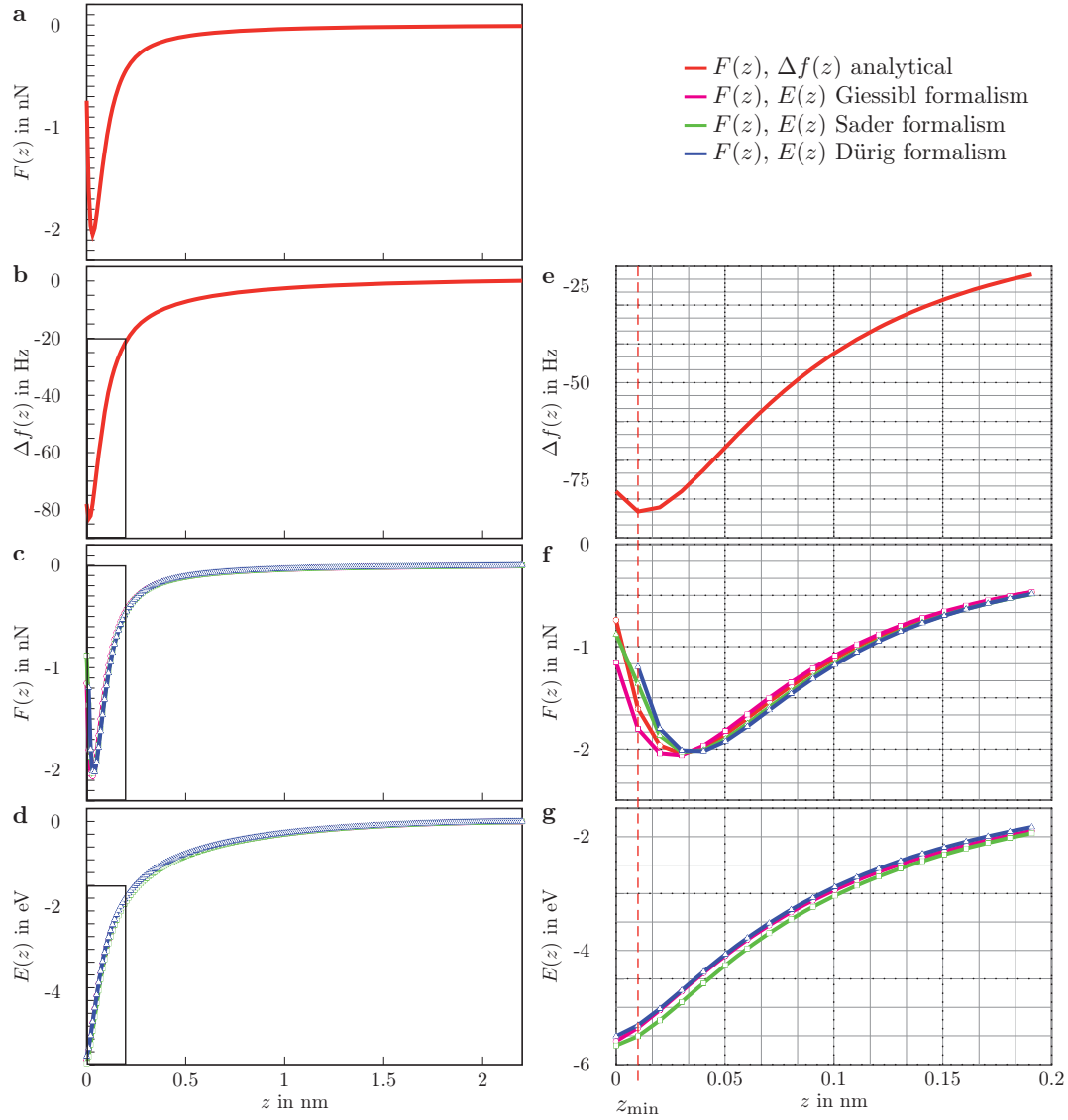


Figure 3.8: **a** Analytically derived $F(z)$ -curve. **b** Corresponding $\Delta f(z)$. Comparison of three deconvolution methods for $\Delta f(z)$ leading to force in **c** and interaction potential in **d**. **e-f** present close-ups of **b-d**, respectively. The red dashed line denotes the minimum position z_{\min} of the $\Delta f(z)$ -curve, which is not equivalent to the minima in $F(z)$ and $E(z)$.

CHAPTER 4

INSTRUMENTATION AND PREPARATION

4.1 Set-up

Acquiring topography and three-dimensional force fields with atomic resolution requires not only stable tips, but also sufficient stability of the microscope (the z -feedback is switched off during acquisition), high sensitivity to forces, high vertical resolution, and a high lateral (spatial) resolution. The time to record 3D-FFS data sets is longer than for regular topographic images, up to several hours compared to some ten minutes, respectively, depending on the desired resolution. Piezo voltage creep (due to the non-linearity of the deflection versus voltage characteristic of the piezo material) and electronic drift of electronic components in the detection circuit can lead to severe problems, such as uncontrollable tip crashes eventually leading to loss of magnetic sensitivity. The demanding task of performing MExFM and 3D-FFS with magnetic sensitivity was achieved using a home-built microscope, operated at low temperatures and in ultra high vacuum (UHV).

The microscope (so-called *Hamburg design* [79]) (see figure 4.1a and b) is equipped with a superconducting split-coil magnet and is operated at a temperature of 8.1 K with variable magnetic fields of up to 5 T flux density perpendicular to the sample.

To reach the low base temperature, the instrument is placed in an UHV compatible liquid helium bath cryostat providing cooling of microscope and magnet. The design of the cryostat allows easy access from the side through a shutter system for fast *in situ* tip and sample exchange (see figure 4.1c). The cantilever deflection detection system is realized by a FABRY-PEROT interferometer.

The UHV system with a base pressure in the low 10^{-11} mbar regime includes four different UHV chambers giving the possibility to prepare and characterize sample and tip *in situ*. A fast-entry lock is attached to the system to introduce

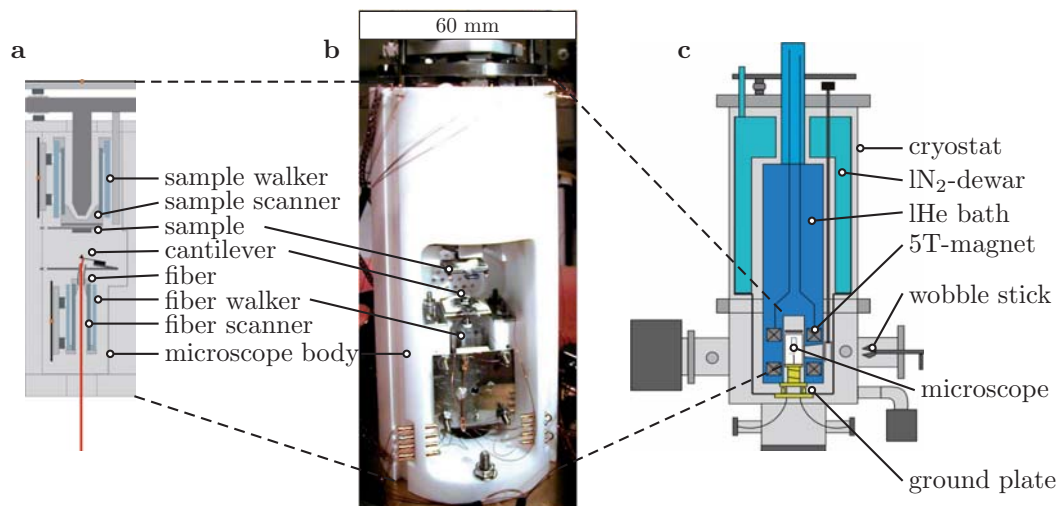


Figure 4.1: **a** Side view and **b** photograph of the microscope. **c** The cryostat-chamber housing the microscope.

samples and tips without breaking the vacuum. Treatment of tip and sample is performed in a preparation chamber equipped with an electron beam heater, an Ar⁺-sputter gun, a resistive heating, and different metal evaporators, that is, the evaporant is heated by electron bombardment. The evaporators contain a chromium crucible and rods of iron and others. A second chamber contains surface analysis tools, such as low energy electron diffraction and Auger electron spectroscopy, as well as an additional commercial microscope combining AFM and STM at room temperature [92], equipped with sample and tip storage. The benefit of the room temperature microscope is the possible pre-characterization of several samples on a short time scale. Thus it is used for growth studies before inserting the as prepared samples into the low-temperature AFM.

Exact positioning of tips and samples during preparation is assured by *xyz*-manipulators. This is necessary, for example, during evaporation of thin magnetic films onto substrate and tip. To get reproducible preparation results, the evaporation rate of the metal evaporators is calibrated prior to any preparation using a quartz crystal microbalance (QCMB). During metal deposition sample and tip can be heated up to 900°C promoting diffusion of the evaporated metal atoms on the surface, thus leading to specific growth results. The third chamber is the cryostat chamber containing another sample and tip storage and the low-temperature AFM. A fourth chamber is equipped with a molecule evaporator used to deposit molecules from the vapor phase onto a sample, which again is heatable during deposition [93]. Samples and tips are transferred between the chambers by means of magnetic linear and rotary motion drives and mechanical hands.

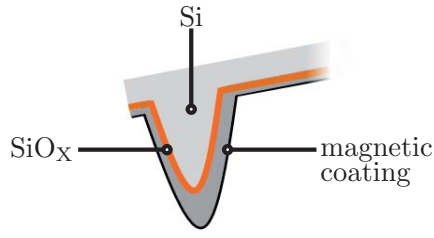


Figure 4.2: The cantilevers, made of Si, are covered with an insulating native oxide layer of unknown crystallographic structure (SiO_x). Prior to any experiments the cantilevers are coated with magnetic material from top and side, leading to a closed metallic layer.

As the AFM is very sensitive to external noise sources, such as mechanical, acoustic and electric noise, sufficient vibration isolation of the microscope is achieved by pneumatic damping legs decoupling the UHV system from its foundation, which in turn is separated from the main building foundation. Thereby, mechanical noise sources such as underground railway, traffic and construction noise can be attenuated or even ruled out. During measurement, mechanical pumps and all unnecessary electronics are switched off. The data acquisition system is located in a neighbouring room to prevent further noise, such as acoustic noise due to talking experimentalists.

4.2 Tip Preparation

Measurements are performed using two different types of commercially available doped-silicon cantilevers with integrated pyramidal tips at their free end [46]. While in some experiments *SuperSharpSilicon*-type tips with dimensions $l = 225 \pm 5 \mu\text{m}$, $w = 38 \pm 5 \mu\text{m}$ and $t = 7 \pm 0.5 \mu\text{m}$ were used, cantilevers with $l = 250 \pm 10 \mu\text{m}$, $w = 71 \pm 7.5 \mu\text{m}$ and $t = 10.5 \pm 1 \mu\text{m}$ were mainly used in the exchange force related experiments. Both cantilevers are supersharp with a nominal tip radius of $< 2 \text{ nm}$, but they differ in spring constant. Following [94] the spring constant is calculated using the geometrical dimensions of the cantilever and its eigenfrequency,

$$c_z = 4\pi^2 M_e \rho l w t f_0^2, \quad (4.1)$$

with silicon density $\rho = 2330 \text{ kg/m}^3$ and normalized mass $M_e = 0.2427$. Spring constants of $c_z \approx 35 \text{ N/m}$ and $c_z \approx 140 \text{ N/m}$ are calculated, respectively. Hence, the larger cantilevers (high- c cantilevers) are less sensitive to force but smaller tip-sample distances are adjustable without a snap-to-contact¹.

¹According to [87] and using a typical experimental amplitude of $A = 3 \text{ nm}$, the force should exceed $3 \text{ nm} \times 140 \text{ N/m} = 420 \text{ nN}$ in close proximity of tip and sample to lead to a snap of the high- c cantilever to the surface, while it should only exceed $\approx 100 \text{ nN}$ for a low- c cantilever.

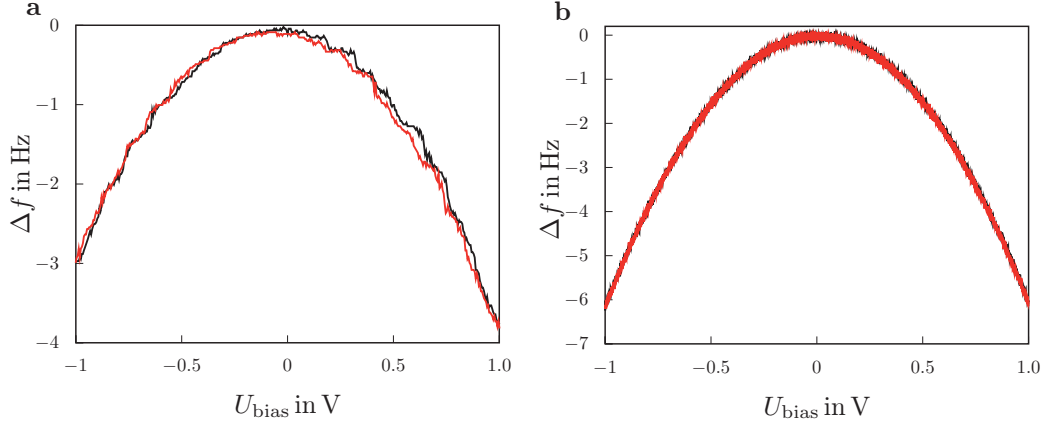


Figure 4.3: $\Delta f(U)$ -curves of a non-conductive tip in **a**, showing single tunnelling events between trapped charge states in the tip, and a conductive tip in **b** showing a smooth parabolic curve without hysteresis in trace and retrace.

Parameters: **a** $\Delta f = -1$ Hz, $c_z = 36.6$ N/m, $A = 5$ nm, $f_0 = 165$ kHz, Fe coated.
b $\Delta f = -0.5$ Hz, $c_z = 37.5$ N/m, $A = 5$ nm, $f_0 = 167$ kHz, Cr coated.

To be able to nullify long-range electrostatic forces, tip and cantilever should be conducting. Although doped to enhance conductivity, the used silicon cantilevers are covered with an insulating native oxide layer of unknown crystallographic structure (SiO_X) due to a wet etching procedure during production, cf. figure 4.2. Using argon ion sputtering to remove contaminations and the native oxide layer, as previously reported [17], eventually leads to a pure Si tip end, but results in blunter tips. This is an unwanted effect as blunt tips enhance the detection of long-range forces and, hence, true atomic (and magnetic) resolution is harder to achieve. In addition to SiO_X , cantilever and tip are contaminated by a water layer after storage in air. This layer can be removed by heating the tip *in situ*, but again, the tip will get blunter simultaneously. However, the conduction of doped Si is even worse at low temperatures. It turned out that, although reasonable film growth and film adhesion might be hindered by contaminations and by the water layer, *in situ* metal coated tips show higher conductivity than untreated silicon tips. Moreover, the coated tips preserve the essentially important small tip radius, cf. figure 4.2.

As coating material, iron or chromium are chosen with film thicknesses of 4-8 nm. The metals are deposited with about one atomic layer (AL) per minute on top and side of the tip, sketched in figure 4.2. While thin and smooth metal films are needed, Fe and Cr grow in a Stranski-Krastanov-like growth mode on SiO_X [95,96], which is, they wet the substrate but soon start to form three dimensional islands. The number of islands is increased with increasing number of nucleation centers, hindering the diffusion of the deposited metal. Due to its three dimensional growth, the tip coating might not be regular and smooth, and, hence, eventually might be non-conductive. Conduction is confirmed during the experiment by obtaining $\Delta f(U_{\text{bias}})$ -curves and a parabolic

shaped $\Delta f(U_{\text{bias}})$ -curve indicates a metallic tip (cf. chapter 3.5.1). When two $\Delta f(U_{\text{bias}})$ -curves, trace and retrace, respectively, are obtained, they should be congruent in the conductive case. If trace and retrace show a hysteresis, charges are induced into the tip by the applied voltage but decharging happens not instantaneously. This indicates a non-conductive tip. Not fully covered and thus not perfectly conductive tips can be further distinguished by abrupt jumps within $\Delta f(U_{\text{bias}})$ -curves. Here, localized states within the tip are charged and decharged and the jumps can be considered as single tunnelling events between such trapped charge states in the tip [97,98]. $\Delta f(U_{\text{bias}})$ -curves including trace and retrace of a non-conductive and a conductive tip are displayed in figure 4.3a and b, respectively. The non-conductive tip in a shows single tunnelling events.

Magnetically Sensitive Tips

To perform spin-sensitive experiments, the prepared tips should be magnetically sensitive, that is, the foremost tip apex atom should carry a net magnetic moment. Using Fe as tip material simplifies the system of tip and sample as only the exchange interaction between Fe atoms has to be considered, even after tip changes, whereby material might be transferred from the sample to the tip (cf. chapter 8). However, for Fe coated tips it is frequently observed that large amounts of material are spontaneously transferred from the tip to the surface in an avalanche like effect, which often results in a non-conducting tip, that is, all tip material gets lost.

Thus, a material with higher adhesion to SiO_x is chosen. From a simple approach using scotch tape to compare the adhesion of different metals on silicon, Ti and Cr turned out to be better candidates than Fe, as they adhere much better to Si. Titanium grows smoothly on Si but is non-magnetic. Anyway Ti might be additionally used as adhesion layer for magnetic material, but two layers of metal coating will lead to blunter tips, cf. figure 4.2. Since a magnetic material is needed, Cr is chosen. However, in contrast to Fe, Cr is antiferromagnetic. The structure of chromium is bcc with a lattice constant of 288.4 pm. Its Néel temperature amounts to $T_N = 311 \text{ K}$ [99]. The moment per atom in the bulk is $0.59 \mu_B$ [100,101].

Besides the better adhesion, Cr has no stray field. Thereby it limits the influence of magnetostatic interactions on the contrast formation in MExFM. Moreover, using Cr will lead to a stronger exchange signal at larger separation than Fe, according to theoretical findings: LAZO and co-workers [102] calculated the exchange forces between a single atom tip and different lattice sites of the Fe/W(001) surface, that is, on parallel (p) and antiparallel (ap) oriented atomic magnetic moments with respect to the tip magnetic moment. They included single atom Fe and Cr tips into their DFT calculations and the results actually show an increase of magnetic resolution at short distances for Cr in comparison to Fe. This can be understood in terms of a larger value of

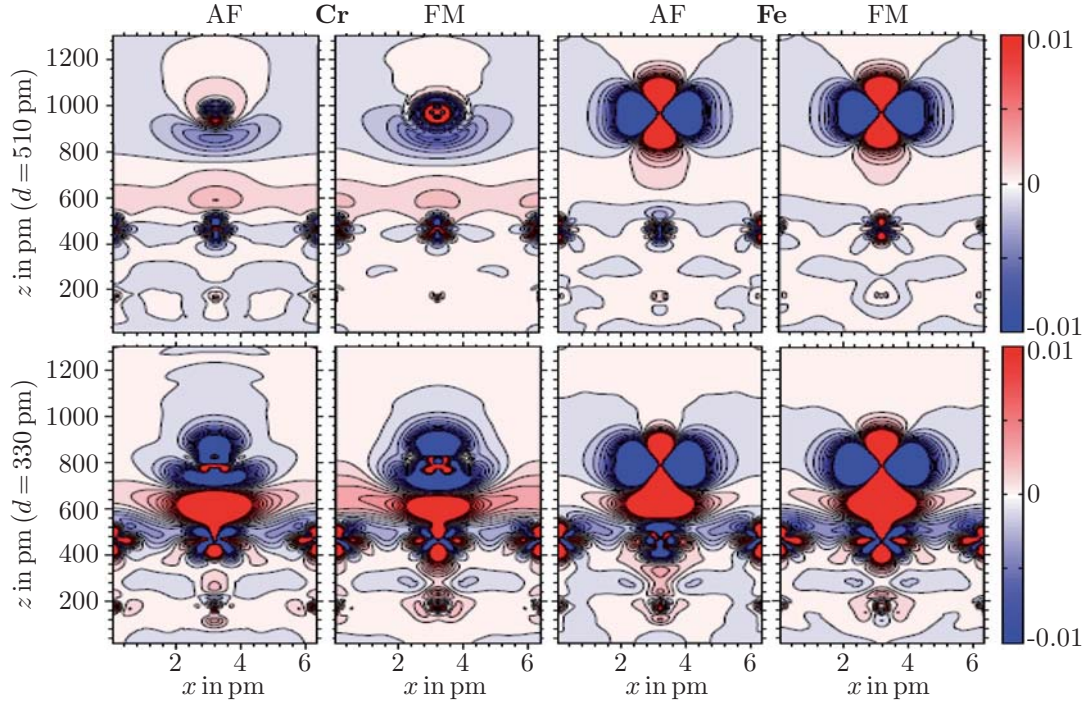


Figure 4.4: Total charge density difference plots for Fe and Cr tips at two tip-surface distances, $z = 510$ pm (upper panel) and $z = 330$ pm (lower panel), respectively. The plots show the charge redistribution in the system due to tip-surface interactions for ap- and p-alignment (AF- and FM-coupling, respectively). Zones in red and blue denote charge accumulation and depletion, respectively.

magnetic moment of the tip atom and also by a farther extension of the wave function of the $3d$ orbitals, that is, the delocalization of charge density. To study the nature of the magnetic exchange interaction, which can be traced to the different electronic interactions in the AF- and FM-configuration, LAZO analyzed charge-density difference (CDD) plots for these two types of coupling. The CDD is obtained by subtracting the charge density of the isolated monolayer and that of the isolated metal cluster tip from the charge density of the interacting system consisting of the metal cluster tip and the iron monolayer of Fe/W(001). Hence, the CDD plots allow the visualization of accumulation or depletion of charge. The results obtained are presented in figure 4.4 for Cr and Fe at two different distances, 330 pm and 510 pm, for both configurations, AF- and FM-coupling between probing atom and surface atom underneath, respectively.

At large separation (upper panel in figure 4.4) there is a small net charge accumulation between the tip atom and the surface Fe atom for both tips. Already at this height the interaction depends on the type of spin alignment. The charge accumulation due to tip-sample interaction is localized at the Fe surface atom and it has a node for the FM alignment with the Cr tip, while in the AF configuration for the Cr tip it has nodes on both the Fe surface

and the tip atom. For the Fe tip there is only a small charge accumulation at the tip atom. The accumulation at this distance is already largest for the Cr tip, indicating the splitting of the exchange forces on ap- (AF-coupled) and p-site (FM-coupled) to be detectable already at larger distance than with Fe tips. At closer distance of $z = 330$ pm (lower panel in figure 4.4) electronic charge strongly accumulates between the tip atom and the surface Fe atoms, implying a strong electronic interaction between tip and surface. The charge accumulation is strongest for the Fe tip in FM configuration, indicating strong bonding between tip atom and surface atom (thus clarifying the possibility of structural tip changes, as will be discussed in chapter 8). A large charge accumulation, although smaller than for Fe, is also observed for the Cr tip. Again the accumulation for the AF-coupling is larger than for the FM-coupling. The CDD plots also show that the charge density of the nearest-neighbor Fe atoms with respect to the probed surface atom is considerably redistributed upon approaching the tip. Therefore, the exchange coupling of these nearest-neighbor Fe atoms with the tip atom plays an important role in determining whether FM- or AF-coupling is more favorable.

4.3 Sample Preparation

For the MExFM and MExFS experiments presented in the forthcoming chapters, the aim is to prepare large and clean areas of the 1st layer of iron on tungsten in the (001) orientation, as it has unique magnetic properties, that is, the monolayer orders antiferromagnetically. Hence, little more than one atomic layer (AL) iron is deposited onto a clean W(001) surface by means of an electron beam evaporator [103] at a rate of one AL/min.

In order to prepare clean W(001) surfaces, a procedure of consecutive annealing and flashing cycles is necessary. This procedure requires high temperatures of about 2000 K of the tungsten crystal surface. To reach these high temperatures, a special electron beam heater is used. Unlike other set-ups [104], the crystal, fixed on a holder, is hooked to a tungsten wire, thus reducing the heated surface to an absolute minimum and leading to lower pressure during annealing and flashing. The crystal holder additionally exhibits a central hole directly underneath the crystal, whereby the mass of the holder is reduced and the crystal is directly hit by the electron beam. This in consequence reduces the power needed to heat the sample. As thermal expansion leads to stress within the wire, relative movement between crystal and heater might occur. To provide exact positioning the filament is mounted on a xyz -stage and a distance of 2 mm between heater and crystal is adjusted prior to any heating. Using this set-up, a voltage of $U_{HV} = 1200$ V and a filament current of $I_{fil} = 3$ A lead to 75 mA emission current between filament and crystal and a power of 90 W, which equals a temperature of 2170 K at the sample surface, as verified by an external infrared thermometer [105]. Figure 4.5a shows

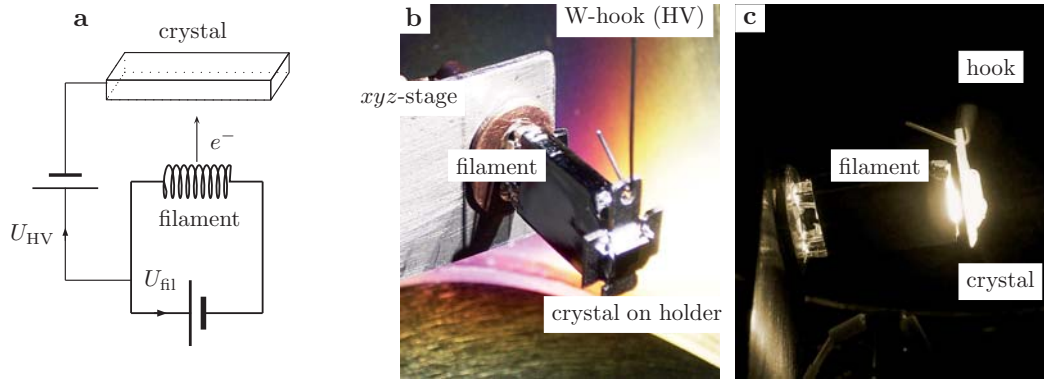


Figure 4.5: **a** Sketch of the tungsten stage. Electrons emitted from a filament are accelerated to the backside of the tungsten crystal. The crystal easily reaches temperatures > 2600 K, while already 2170 K are sufficient to clean its surface. **b** The stage after aligning crystal and filament with a distance of 2 mm between crystal backside and filament and **c** during a flash.

a sketch of the working principle of the tungsten e-beam stage. Figure 4.5**b** and **c** present images of the stage within the UHV chamber after alignment of crystal and filament and during flashing, respectively.

Prior to the preparation of Fe/W(001), any filaments (electron beam heater filament, evaporator filament), heaters (heating stage for post-annealing), and shuttles (transport shuttle) used during the preparation steps have to be thoroughly degassed. Moreover, already before the tungsten crystal is introduced into the UHV chamber system, it is useful to degas its sample holder and the transfer shuttle. The following listings cover all steps to be proceeded, before the crystal is ready for Fe deposition.

1. Degas of the tungsten sample holder to which the crystal will be mounted: $T > 2200$ °C for some minutes.
2. Degas of the stainless steel transport shuttle used to move the sample holder between different preparation stages: $T > 400$ °C for some minutes.

To clean the crystal for the first time after it has been stored in air, cycles of heating in oxygen and flashing are necessary. By heating high-purity tungsten under oxygen atmosphere with a partial pressure between 1×10^{-6} mbar and 5×10^{-8} mbar (depending on the contamination prior to cleaning) a maximum segregation rate of carbon, which is dissolved in the bulk as main impurity, from bulk to selvedge, that is, to the first two layers of tungsten below the surface, and a maximum diffusion from the selvedge to the (001) surface are achieved [106]. Once in the surface, refractory tungsten carbides are oxidized, thus forming volatile carbon monoxides and carbon dioxides which desorb thermally, leaving pure tungsten. Residual tungsten oxides are removed by a 10 s long

subsequent flash at a temperature of 2170 K. This temperature is found to be high enough to remove lesser contaminants, like sulfides, carbon monoxides and hydrogen, and old Fe films, while a temperature of > 2500 K, known in literature as good value to clean the W(001) crystal surface [107,108], enhances the contamination of the tungsten surface with material from the selvedge. Moreover, flashing the crystal too high in temperature leads to a bunching of step edges on the stepped substrate surface and even produces dislocation lines within the crystal, along which carbon segregation might be enhanced. After several annealing and flashing cycles a carbon depletion layer is formed between selvedge and bulk. Summing up, the cleaning of W(001) is as follows:

Cleaning of W(001)

1. Dose oxygen into the chamber with a partial pressure between 1×10^{-6} mbar and 5×10^{-8} mbar.
2. Heat the W(001) crystal: $T = 1570$ K for 10 minutes.
3. Crystal cool down for about 15 minutes.
4. Close the oxygen valve.
5. Flash the crystal: $T = 2170$ K for 10 seconds.
6. Continue with point one until the crystal is clean.

The cleaning cycles lead to clean surfaces with no traces of oxygen or carbon contaminations according to Auger electron spectroscopy data. The crystal is now ready for Fe deposition. To gain high quality iron films the base pressure prior to the preparation of Fe/W(001) should be on the order of 1×10^{-10} mbar or better, as all following preparation steps are carried out within the same chamber. To enhance pumping speed, a cryogenic pump located within the ion getter pump pumping the chamber is activated for the time of preparation using liquid nitrogen. Additionally the chamber is equipped with a passive pump [109].

First of all, the crystal is flashed again to assure a clean surface. During flashing the pressure should not exceed 3×10^{-9} mbar. If the pressure is higher, either the crystal or the immediate surrounding (sample holder, electron beam filament) should be considered as dirty and the flashing should be repeated. As long as the crystal cools down after the last flash, the metal evaporator is heated up. During the transfer of the crystal from the flashing stage to the evaporation position, for which the transport shuttle is used, the pressure decreases to below 2×10^{-10} mbar with the evaporator operated (the evaporator shutter is still closed). When shuttle and crystal reach slightly elevated temperatures of ≈ 320 K, the evaporator shutter is opened and iron is deposited onto the warm surface at a pressure of better than 2×10^{-10} mbar. After about

one minute of evaporation (the evaporator is shut off), shuttle and crystal are annealed to about 570 K to further enhance the surface diffusion of iron. During annealing the pressure further decreases and reaches base pressure, if not even better. After 10 minutes of annealing preparation is done and the sample might be transferred into the microscope.

The single steps of preparation are listed in the following.

Fe deposition

1. Start at a base pressure $<1 \times 10^{-10}$ mbar.
2. Flash the crystal: $T = 2170$ K for 10 seconds.
3. Crystal cool down: $T \approx 320$ K.
4. Deposit Fe.
5. Post-annealing: $T = 570$ K for 10 minutes.

The transfer of the crystal into any microscope should be performed with care, that is, the manipulators should not produce too much dirt due to mechanical friction. After about 30 minutes of overall preparation time the sample is introduced into the cold microscope.

If, after some time, a fresh Fe layer has to be prepared, the old one is simply removed by a 10s short flash, and the preparation follows the given recipe. However, any filaments (electron beam heater filament, evaporator filament), heaters (heating stage for post-annealing), and shuttles (transport shuttle) used during the following preparation steps have to be thoroughly degassed prior to any Fe deposition. After several flashes prior to Fe deposition, the surface is contaminated again due to slow but steady segregation of carbon and the cleaning of the W(001) crystal has to be repeated. Typically five cycles of glowing and flashing again lead to a clean surface. The role of pressure and temperature on the growth of iron is discussed in the following.

Film Quality

Due to its miscut of 0.1° the stepped W(001) surface used in the experiments exhibits terraces with widths between 20 nm and 150 nm (the calculated mean terrace width is 90 nm). The steps are running along the $[010]$ direction of the substrate. The bcc tungsten single crystal has a bulk lattice constant of 316.5 pm. Considering the (001) surface, the height of an ideal monatomic W step is 158.3 pm. Iron grows pseudomorphically in a Stranski-Krastanov mode on W(001) up to the fourth layer [107], hence the substrate is covered by a single AL (wetting layer) and excess Fe forms second layer islands on terraces and second layer stripes along step edges of the underlying substrate in a thermal induced step flow growth behaviour, that is, the elevated substrate

temperature during the evaporation enhances the diffusion of Fe atoms on the W surface. First and second layer iron show a fourfold symmetry due to the bcc structure of the underlying crystal surface.

The quality of the growth of iron on tungsten strongly depends on the purity of the tungsten substrate, temperature during growth, and on the annealing temperature afterwards. Moreover, the pressure during the different preparation steps strongly influences the cleanliness of the surface.

If preparation conditions are bad, for instance, if the tungsten substrate is dirty or if the pressure exceeds 2.5×10^{-10} mbar during evaporation or annealing, the monolayer typically exhibits many defects and contaminations, hindering the step flow growth. For this reason, second layer iron is not diffusing to the step edges but is pinned to nucleation centers on the monolayer. Figure 5a shows an example of 1.4 AL Fe/W(001), where second layer islands are pinned and do not grow with fourfold symmetry. Additionally, many defects are visible in the first layer. The pressure during the evaporation did not exceed 1.5×10^{-10} mbar, which regularly leads to large and clean areas of monolayer iron. Hence, the substrate has to be considered as dirty and needs cleaning with oxygen (step 5). Figure 5b shows 1.25 AL Fe/W(001) prepared on a clean tungsten crystal at a pressure of 1.1×10^{-10} mbar during the evaporation. However, second layer iron cannot flow to the step edge, though the islands grow with fourfold symmetry.

The fourfold island symmetry indicates a clean tungsten substrate, but different to other preparations this sample was not post-annealed but held at 570 K during the evaporation, demonstrating the temperature dependence of the step flow growth. Figure 5c shows a preparation at good pressures, however the coverage is 1.7 AL Fe/W(001) and the area of first layer iron is rather small to conveniently perform exchange experiments: coverages of less than 1.3 AL Fe with large, clean and defect free Fe monolayer areas as in figure 5d are much better suited for MExFM.

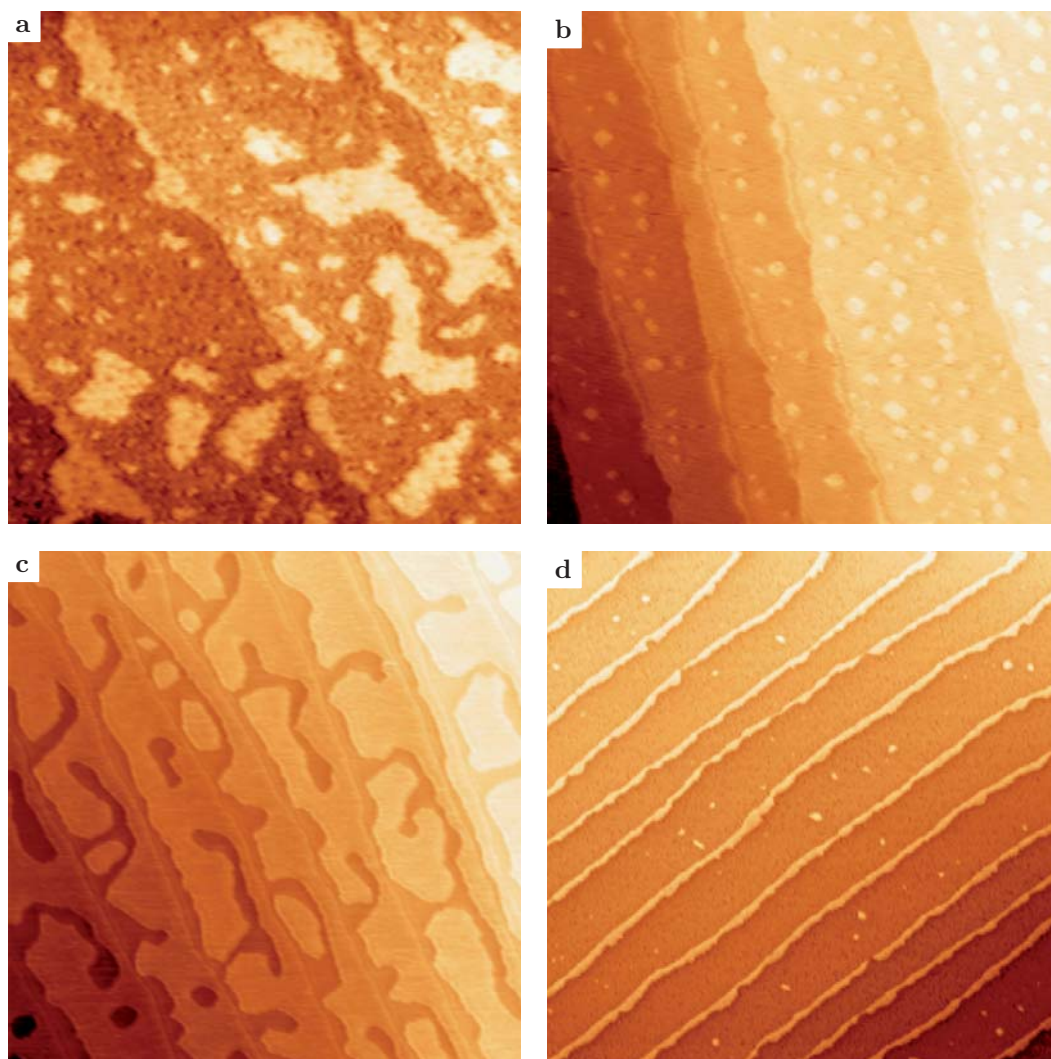


Figure 4.6: Four different Fe/W(001) samples prepared with different parameters and different pressures during the preparation.

CHAPTER 5

GROWTH AND PROPERTIES OF 1st AND 2nd LAYER FE ON W(001)

When mapping the prepared surface with a coverage between 1 and 2 AL iron on W(001) it turns out that this system is structurally, electronically and magnetically inhomogeneous. Since force microscopy detects all electromagnetic forces simultaneously, imaging of inhomogeneous samples is particularly challenging. On one hand, a wealth of information can be obtained, but on the other hand, the forces are often difficult to separate from each other. However, Fe/W(001) is covered by only one chemical species and the long-range van der Waals force does not vary locally, hence, it does not lead to an image contrast. On atomic length scales even the total long-range force does not vary locally and the image contrast is dominated by short-range interactions such as chemical and exchange forces. A detailed analysis of the different properties of the highly strained Fe film on W(001) is presented in the following.

5.1 Structural Properties

The overall resulting topography of ≈ 1.3 AL Fe/W(001) obtained using non-contact FM-AFM is displayed in figure 5.1 with the corresponding line section along the white dotted line displayed above the image. The measured height of 128 pm between first and second layer iron grown on the same W terrace fits well to a theoretically predicted value of 120 pm [110]. The surface unit cell of the first AL iron has a $p(1 \times 1)$ structure with respect to the underlying W(001) with a measured lattice constant of 320 pm, see colored close-up III in figure 5.1. Every protrusion herein represents chemically identical iron atoms. Numerous defects, such as missing atoms, are revealed within the wetting layer, showing that the first layer does not fully cover the tungsten surface. This effect can be especially seen along step edges as vacancies between second layer stripe and single iron layer on the upper terrace. A step edge vacancy is colored in area

II in figure 5.1. Wires of atomic width connect wetting layer and second layer stripe. On the second layer an additional four-fold symmetry can be seen (see colored close-up I in figure 5.1). Atomic trenches and protruding atomic rows appear due to high strain induced by the large lattice misfit of $f = (a_{\text{layer}} - a_{\text{substrate}})/a_{\text{substrate}} = 9\%$ between iron and tungsten. Height differences of 10-13 pm are measured between trenches and protrusions compared to height differences of 10-15 pm between second layer iron stripes and first layer iron on the upper terrace. A detailed analysis of the further growth of iron on tungsten up to several monolayers can be found in [111].

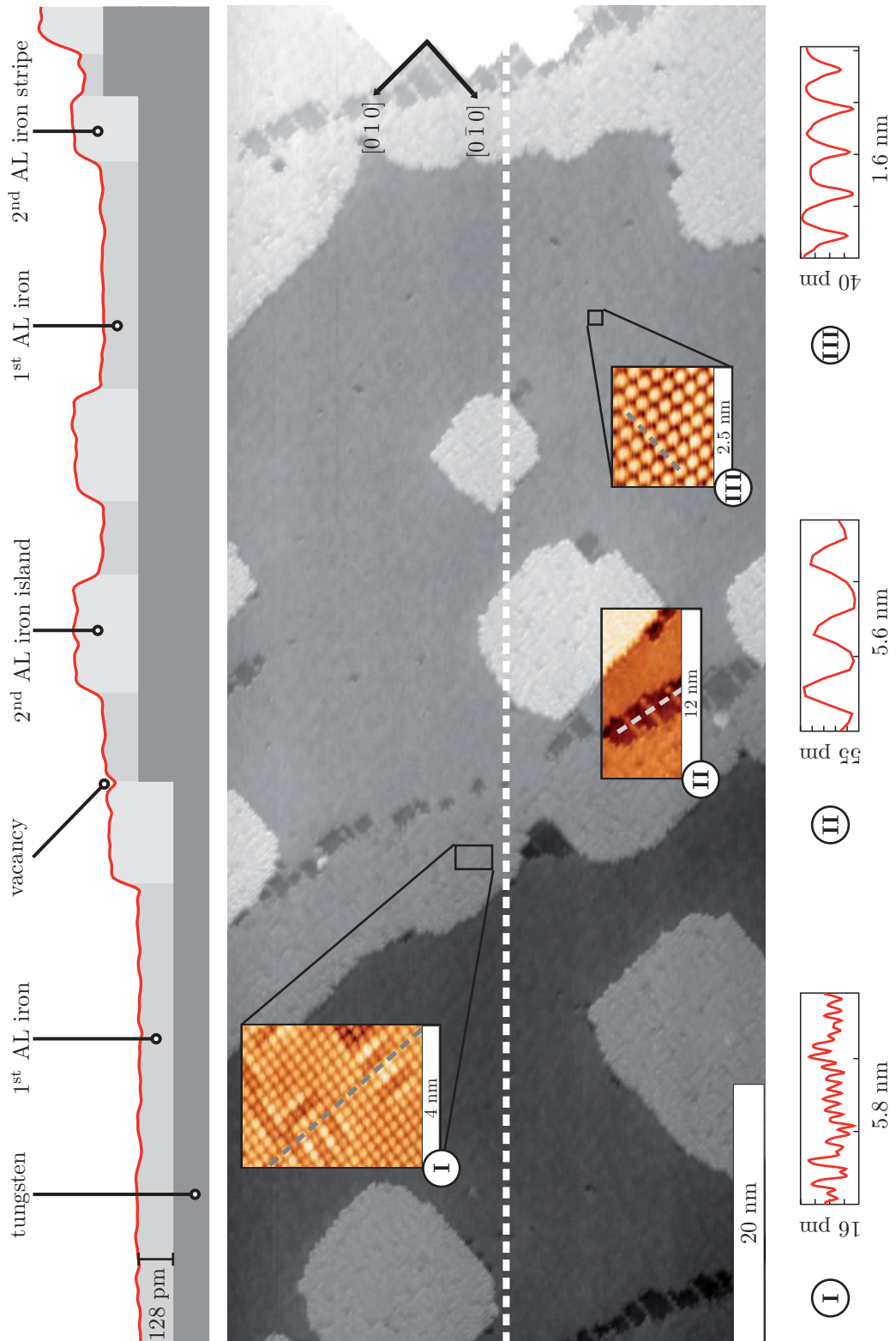


Figure 5.1: Morphology of ≈ 1.3 AL iron pseudomorphically grown on W(001).

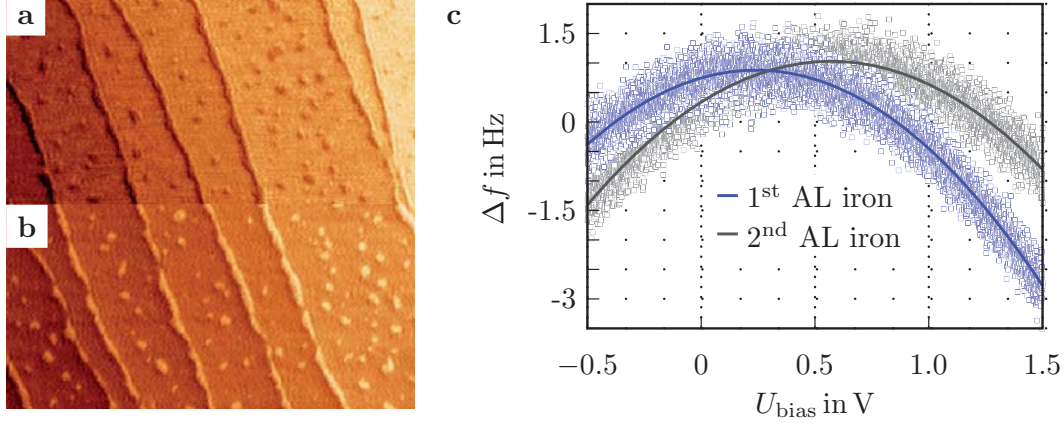


Figure 5.2: Bias voltage dependent contrast on ≈ 1.2 AL Fe/W(001) obtained with FM-AFM on a $500 \times 500 \text{ nm}^2$ area at $U_{\text{bias}} = 0.5 \text{ V}$ in **a** and $U_{\text{bias}} = 0 \text{ V}$ in **b**. **c** $\Delta f(U_{\text{bias}})$ -curves taken on first (blue) and second (gray) layer iron. The CPD relative to the tip is $U_{\text{CPD},1^{\text{st}}} = +0.24 \text{ V}$ and $U_{\text{CPD},2^{\text{nd}}} = +0.57 \text{ V}$. The resulting work function difference between 1st and 2nd layer Fe is 0.33 eV.

5.2 Electronic Properties

When imaging Fe/W(001) at different bias voltages, an electrostatic contrast with different bias dependent apparent step heights of first and second AL iron is observed. Figure 5.2a and 5.2b show the surface of ≈ 1.2 AL Fe/W(001) recorded at different bias voltages of $U_{\text{bias}} = 0.5 \text{ V}$ in **a** and $U_{\text{bias}} = 0 \text{ V}$ in **b**, respectively. Clearly, a contrast inversion is visible: dark areas in **a** (second layer Fe) appear elevated in **b** with respect to first layer Fe. By evaluating the two $\Delta f(U_{\text{bias}})$ -curves in figure 5.2c obtained on the first (blue squares) and second layer iron (gray squares), respectively, the work function difference $\Delta\Phi$ can be roughly determined with respect to the Fe coated tip. The curves were fitted by a parabola (solid lines) and the difference of the apices corresponds to $\Delta\Phi = 0.33 \text{ eV}$. Hence, the capacitive electrostatic force is different on first and second layer iron and the real topography is unknown a priori. The effect of the electrostatic force on the topography can be minimized by applying the mean CPD [50] $U_{\text{bias}} = U_{\text{CPD,mean}} = \frac{1}{2}(U_{\text{CPD},1^{\text{st}}} + U_{\text{CPD},2^{\text{nd}}})$ which is the crossing point of both curves in figure 5.2c. Hence, the real topography is obtained either at close tip-sample distance, or using KPFM to map the work function during imaging and compensate for the CPD on every data point, or by applying the mean CPD.

The KPFM images in figure 5.3 show a CPD-map of ≈ 1.7 AL Fe/W(001) in **a** and the simultaneously recorded topography in **b**. A line section through both data channels reveals the real topography with a step height of 128 pm between first and second layer iron and a height of 10-15 pm between second layer stripe and first layer iron on the upper tungsten terrace. These values

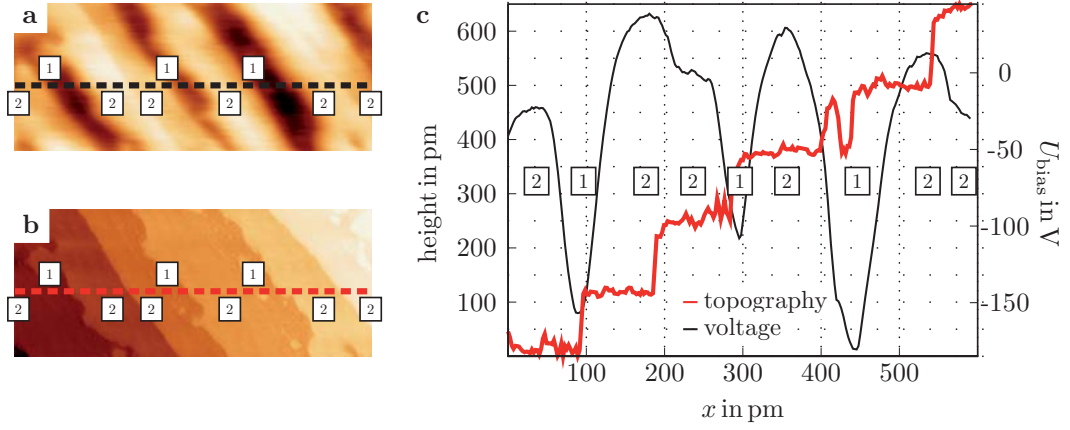


Figure 5.3: **a** CPD-map of ≈ 1.7 AL Fe/W(001) obtained with KPFM. **b** Imaged area with size $600 \times 250 \text{ nm}^2$ simultaneously measured with AFM and nullified CPD between tip and sample at every data point revealing the real topography. **c** Line section in black (potential) and red (topography) covering first and second layer. A potential difference of $\Delta\Phi \approx 0.15 \text{ V}$ between first and second layer iron and $\approx 0.035 \text{ V}$ between adjacent second layer stripes is measured.

are in agreement with the ones obtained at small tip-sample separation in figure 5.1 without locally compensated CPD. The potential difference of first and second layer iron is $\Delta\Phi \approx 0.15 \text{ V}$ and even between adjacent second layer stripes a surprising CPD of $\approx 35 \text{ mV}$ is determined. Theory predicts work functions values of $\Phi = 4.55 \text{ eV}$ for W(001), $\Phi = 4.53 \text{ eV}$ for a free standing iron monolayer, $\Phi = 5.12 \text{ eV}$ for the first iron layer and $\Phi = 4.65 \text{ eV}$ for the double layer [112]. This would result in a theoretical work function difference of $\Delta\Phi = 0.47 \text{ eV}$ between first and second layer iron, which is larger than the experimentally observed value.

However, interpretation of KPFM images is not always straightforward. It has been demonstrated [113] that the measured KPFM potential does not exactly match the surface potential of a given location. It rather is a weighted average of all the local potentials on the surface below the tip apex. As the electrostatic force has a long range nature, KPFM signals derive from the interaction of the surface with tip apex and bulk tip. Hence, the resolution of KPFM is always tip size dependent and, as in this case, the signal obtained on second layer iron islands is also island size dependent.

For all topographic images where the focus is put on properties of the single atomic iron layer, the contact potential difference between this very layer and the tip is always compensated by a suitable U_{bias} . Moreover, within the typical measurement distance between tip and sample of a few hundred pm during atomic resolution imaging, the short range chemical forces are much stronger than any long range electrostatic contribution, thus the height differences between first and second AL iron due to a work function difference of a

few hundred meV is negligible and the measured step heights can be considered as true step heights (cf. figure 5.1).

5.3 Magnetic Properties

First Layer

A lack of remanence of the first atomic layer Fe/W(001) was discovered by spin-resolved photoemission [114] and Kerr effect measurements [115] and later interpreted theoretically [23,112,116–118] as an antiferromagnetic ground state of the monolayer. This ground state has already been confirmed experimentally in 2005 bei KUBETZKA *et al.* using SP-STM [24,119]. The change of sign in the exchange interaction from ferromagnetic to antiferromagnetic iron is attributed to the nature of the $3d$ - $5d$ bond between the overlayer and the substrate [23]. Changing the Fe $3d$ band filling of the overlayer or the W $5d$ band filling of the substrate due to strong hybridization shifts the relative position of both bands and alters the character of the $3d$ - $5d$ bond which thus results in a change of sign in the exchange interaction $J_{\perp}(3d-5d)$.

In order to find the magnetic ground state KUBETZKA and co-workers calculated the total energy of the system as a function of interlayer distance between the monolayer and the tungsten surface, both, for the ferromagnetic and $c(2\times 2)$ antiferromagnetic configurations. They found that if the Fe monolayer is more than 317.4 pm away from the W surface, the interaction is small and the monolayer can be considered in good approximation as unsupported (UML). In this case the ferromagnetic solution has the lowest total energy. With decreasing distance, the energy difference to the antiferromagnetic solution becomes smaller until the solutions are degenerate at $d = 238$ pm. However, at lower interlayer distances the Fe-W hybridization increases and the $c(2\times 2)$ AF solution is the ground state. They found the moments for the relaxed ferromagnetic and $c(2\times 2)$ AF state to be $2.06\mu_B$ and $2.67\mu_B$, respectively.

The MAE, here defined as the energy difference between the two magnetization directions, in the film plane and perpendicular to it, has been evaluated including spin-orbit coupling. In agreement with the SP-STM experiment KUBETZKA *et al.* obtained an out-of-plane easy axis with a MAE of 2.4 meV/Fe atom for the AF ground state. For an Fe UML both AF and FM solutions possess an out-of-plane easy axis but with MAE of 3.2 and 1.0 meV/Fe atom, respectively. Due to symmetry the W atoms at the interface are not spin polarized, and their direct contribution to the MAE vanishes for the AF ground state. Thus, the magnetization axis remains out-of-plane as for the UML, with a smaller MAE because of Fe-W hybridization. The calculations performed in [24] further revealed that the states responsible for the magnetic contrast are mainly located in the Fe film and possess d_{z^2} and $d_{xz,yz}$ character at the Fe atoms with antiparallel magnetic moments. Therefore, maxima and nodes of

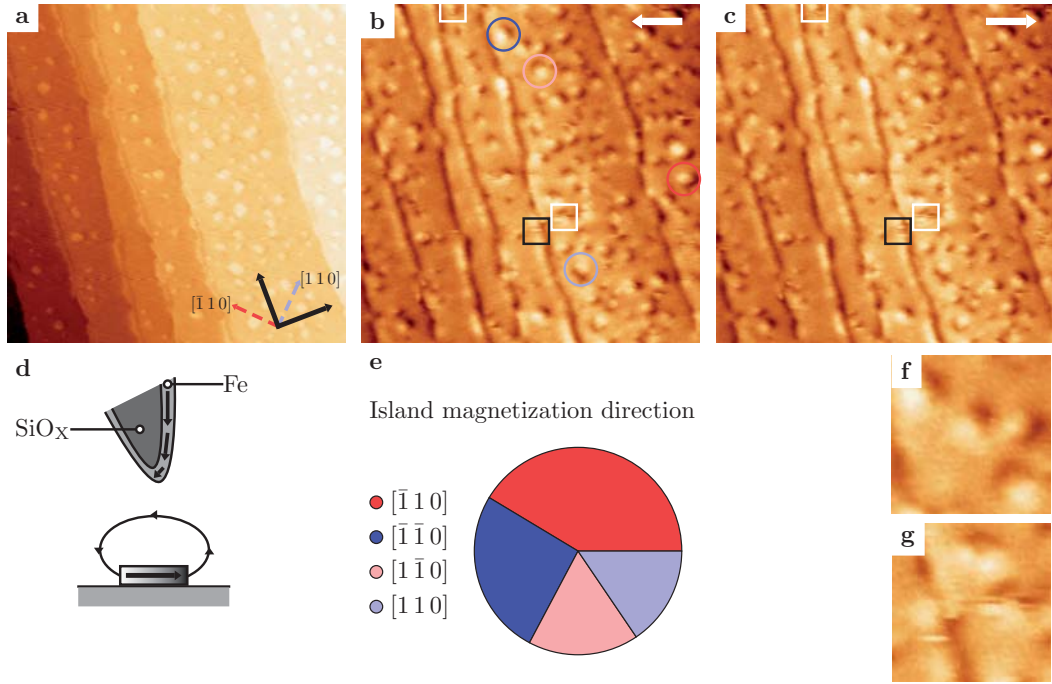


Figure 5.4: **a** $(500 \times 500) \text{ nm}^2$ topography of $\approx 1.2 \text{ AL Fe/W(001)}$ obtained at $\Delta f = -5.5 \text{ Hz}$, $U_{\text{bias}} = 0.4 \text{ V}$ and at zero external flux density. **b** and **c** MFM data in trace- and retrace-channel, respectively, obtained at larger distance, $h = 2 \text{ nm}$, showing a magnetostatic contrast on second layer iron patches: single islands exhibit a dark-bright contrast, while the first layer does not contribute any magnetic signal. The contrast appears due to an out-of-plane magnetic sensitive tip, as visualized in **d**. Evaluating the orientation of all 58 islands leads to the results displayed in **e**. **f** and **g** Close-ups taken from **b** showing islands of different orientation and switching of single islands and stripes, respectively.

the wave function are alternately probed in a SP-STM scan along the $[100]$ -direction and a measurable corrugation amplitude is obtained. The $c(2 \times 2)$ AF magnetic surface unit cell is also revealed in chapter 6 using MExFM.

Second Layer

From the above cited works and from an earlier SP-STM study [107] it is known that second layer iron atoms are ferromagnetically aligned and that second layer patches exhibit 4-fold in-plane anisotropy with the easy axis along $\langle 110 \rangle$ -directions. Thus, no long-range magnetostatic signal from the monolayer can be expected while the net magnetization of the second layer should result in a magnetostatic contrast in AFM images at larger distance when working with a metallic magnetic tip exhibiting a net magnetization. To assure a magnetic metallic tip the cantilever is coated with a thin ($\approx 6 \text{ nm}$ in thickness) layer of iron (see sketch in figure 5.4d) and the tip configuration is not changed throughout the experiments (cf. chapter 8).

When scanning 1.2 AL Fe/W(001) in MFM mode at a height of about 2 nm with respect to the distance used for acquiring topography, a magnetostatic contrast is indeed observed on second layer patches. AFM topography and MFM image are displayed in figure 5.4a and b, respectively. Figure 5.4b and c are trace- and retrace-channel of the same measurement. The second layer iron patches in figure 5.4b and c reveal a dark-bright contrast, although the islands are relatively small with about 1000 atoms each. As expected, the first layer does not contribute any magnetic signal at this tip-sample distance. As the islands show a clear dark-bright contrast, which is also visible in the close-up in figure 5.4f, it can be concluded that they are single domain particles¹, as visualized in the island orientation in figure 5.4d. The distribution of the orientation of the dipolar dark-bright contrast exhibits the previously reported [111, 114, 121] 4-fold symmetry of the anisotropy easy axis in $\langle 110 \rangle$ -directions (blue and red arrow in figure 5.4a). Larger islands in figure 5.4b and c are oriented mostly along $[110]$ and $[\bar{1}\bar{1}0]$ (blue colored in figure 5.4b and e), while smaller islands are mostly oriented along $[\bar{1}10]$ and $[1\bar{1}0]$ (red colored in figure 5.4b and e). In total, 100% of the islands are aligned within the easy axis. Furthermore, some single islands seem to switch their orientation during imaging, as within the white frames in figure 5.4b and c (the magnetic axis of the switching is not clear with ambiguity due to limited spatial resolution). By evaluating trace and retrace on the lines where switching occurs, it becomes clear that the islands are switching their magnetization direction while the tip magnetization stays stable. The black frame in figure 5.4b and c shows a single switching event within a second layer stripe. A switching island and stripe are shown in the close-up in figure 5.4g.

The switching of the magnetization direction (i) might be related to the island size and position of the islands and is a randomly occurring process: MULHOLLAN [114] stated that the disappearance of any magnetic polarization for layers with less than 1.5 ML coverage in his MOKE experiments indicates a superparamagnetic collapse, that is, second layer patches retain their ferromagnetic nature but no longer couple through the iron monolayer with each other. Thus, the moment of the patches would fluctuate along different easy axes such that the measurement-time-averaged magnetization becomes zero. NIU *et al.* stated that the energy barrier for the superparamagnetic rotation within the preferred 180°-direction should reflect the magnetostatic energy stored in the stray field of the particles in addition to their MAE [120]. (ii) The switching could be induced and enhanced by an exchange interaction between single islands: WU [112] found by theoretical considerations that the ferromagnetism of the first atomic layer might be restored below second layer patches due to exchange between first and second layer rather than by the enlarged inter-layer distance to the substrate. He calculated a magnetic moment of $2.43 \mu_B$

¹Single iron islands remain in a single domain state for diameters up to several hundred nanometers [108, 120].

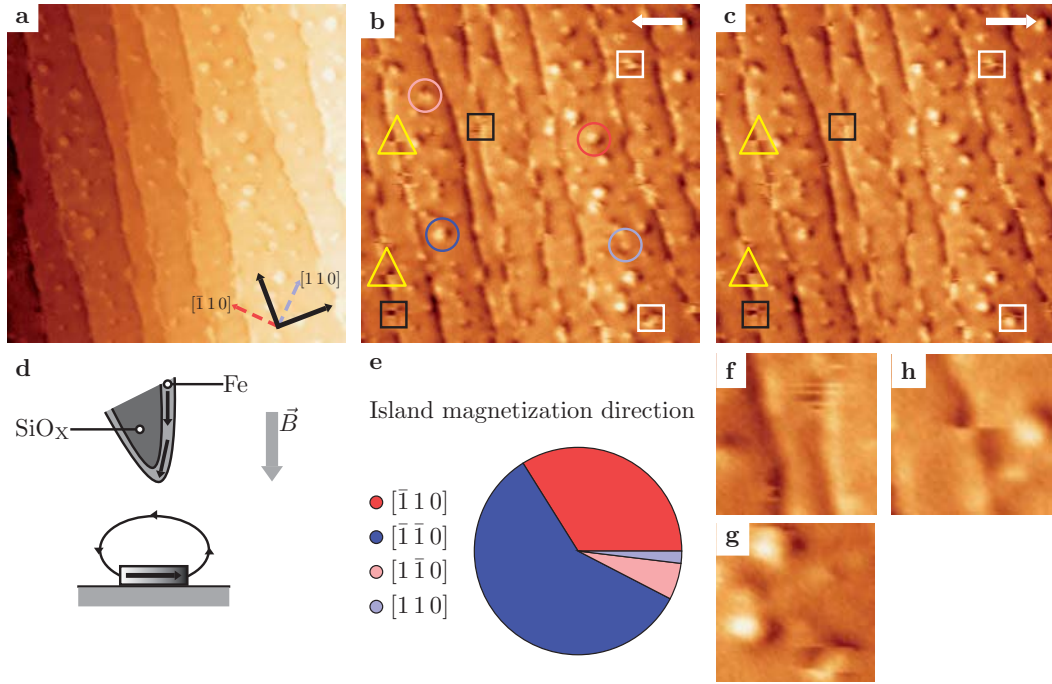


Figure 5.5: **a** Topography as in figure 5.4a obtained at $\Delta f = -5.5$ Hz, $U_{\text{bias}} = 0.4$ V but with 5 T external flux density applied perpendicular to tip and sample. **b** and **c** MFM data, trace and retrace, respectively, obtained at a distance of $h = 2$ nm. Again a magnetostatic contrast on second layer iron patches is observed. First layer iron still does not contribute any magnetic signal. Due to the applied field the out-of-plane magnetic sensitive tip changed its orientation slightly compared to the zero field tip, visualized in **d**. Evaluating the orientation of all 53 islands leads to the results displayed in **e**. **f-h** Close-ups taken from **b** showing switching of stripes and islands and a vortex, respectively. Moreover, islands of different orientation are visible.

for the second layer iron atoms, $0.95 \mu_B$ for the antiferromagnetic monolayer atoms and $1.68 \mu_B$ for the monolayer atoms below second layer patches. (iii) Switching could also be induced and mediated via the island stray field. If considered as single domain particles, second layer iron patches exhibit stray fields leaking from their sides [120]. (iv) The switching might also be induced by the tip stray field. Moreover, the tip stray field could be responsible for the unequal distribution of the island magnetization direction: 41.2% of the islands are oriented along the blue axes, while 58.8% are aligned along the red axes.

The image series in figure 5.4 has been obtained with zero external flux density applied. Scanning the surface with the same tip but an external flux density of 5 T applied perpendicular to the sample surface, the distribution of the 4-fold oriented islands changes, as can be seen in figure 5.5e where figure 5.5b and c (with the corresponding topography in figure 5.5a) have been eval-

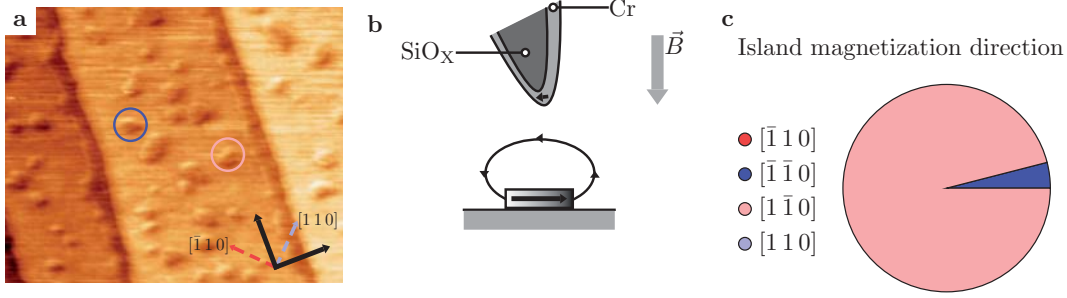


Figure 5.6: **a** $(350 \times 250) \text{ nm}^2$ MFM image obtained with a Cr coated tip at a height of 2 nm, $U_{\text{bias}} = 0.4 \text{ V}$ and with 5 T external flux density applied perpendicular to tip and sample. Surprisingly, a magnetostatic contrast on second layer iron patches is observed, while the first layer iron does not contribute any magnetic signal. Despite the applied field the tip still exhibits an in-plane component at its foremost tip end, visualized in **b**. Evaluating the island orientation leads to the results displayed in **c**. Interpretation of the data is found in the text.

uated according to figure 5.4. Now, 64.2% of the islands are oriented along the blue axes (blue colored in figure 5.5b and e), while 35.8% are oriented along the red axes (red colored in figure 5.5b and e). The switching count of single islands (as within the white frames and as shown in figure 5.5g) is decreased while switching of the second layer iron stripes (as within the black frames and as shown in figure 5.5f) is increased. This leads to the conclusion that the stripes are not oriented along the easy axes and that they are most likely not single domain. The perpendicular magnetic field leads to a canting of the tip magnetization into field direction (cf. figure 5.5d) thus decreasing the inhomogeneous magnetization at the tip end and its in-plane component, and furthermore decreasing the tip stray field. The observations made after applying the field are a strong indication that switching of second layer islands is induced by the in-plane component of the tip-magnetization and that the switching rate thus is reduced by applying a huge magnetic flux density perpendicular to the surface, that is, in terms of energy an increase of the ZEEMAN-energy, a lowering of the tip's stray field energy (relative to the in-plane component) and thus decreasing the total energy to a minimum below exchange energy, MAE and shape anisotropy of the FM islands. Additionally, the field promotes magnetization direction switching of the multi-domain stripes. Beyond switching of stripes and islands, vortices are observed along the step edges, which do not occur in zero field. The vortices, for example the ones marked by yellow triangles or as shown in the close-up in figure 5.5h, establish due to an interaction between pinning of the magnetization by impurities and enhanced energy within the domains.

By studying the sample surface with Cr coated tips instead of Fe coated ones with MFM, interestingly a magnetostatic contrast is detected as well. This is astonishing, because AF chromium has no stray field *a priori*. However, due

to the growth of chromium on silicon the symmetry of the thin film is broken and due to anisotropy terms Cr coated tips may exhibit a non-negligible net magnetic moment at the tip end and hence a stray field. Figure 5.6a shows an exemplary MFM image out of a series obtained with different magnetic field strengths applied and at different heights.

The main finding of the image series is a non-vanishing bright-dark contrast of the islands revealing the magnetostatic sensitivity of the AF tip. The topographic contrast varies in comparison to figures 5.4 and 5.5, because the tip exhibits a stronger in-plane component (see sketch in figure 5.6b), which does not change even with an applied magnetic field of up to 5 T, although both, iron and Cr coated tip, were prepared in the same way. Hence, the ZEE-MAN-energy is not sufficient to overcome the anisotropy of the thin Cr film. Statistics on the island magnetic orientation in figure 5.6c show a 96% orientation along $[1\bar{1}0]$ due to the strong in-plane component of the tip. The tip stray field, for example of an Fe coated tip, which can induce a field on the order of several hundred mT in close distance of a few nm above the surface [122] is obviously strong enough to change the island orientation thus indicating a weak coupling between first and second iron layer.

The most important implications of the presented magnetostatic survey with respect to a magnetic exchange study, however, are that external flux density and tip magnetic moment do not alter the alignment of the AF monolayer. Furthermore, neither electrostatic, nor magnetostatic, nor the element specific van der Waals force contribute to the observed contrast in close-distance AFM, where the short-range interaction forces dominate.

CHAPTER 6

MAGNETIC EXCHANGE FORCE MICROSCOPY ON Fe/W(001)

The proof of principle of MExFM has been demonstrated in 2007 on the antiferromagnetic insulator surface of NiO(001) by KAISER *et al.* [9, 123, 124]. On the strongly correlated NiO(001) the spin-carrying *d*-electrons of the nickel atoms are localized and interact via superexchange along the bridging oxygen atoms. The use of non-contact FM-AFM with Fe coated tips revealed the AF arrangement of magnetic moments with the magnetic signal being just above the noise level of the microscope. Calculations performed by Momida and Oguchi [125] predicted a significant magnetic exchange contrast between an Fe tip and Ni surface atoms of opposite magnetic moments in agreement with the experiment, but other predictions, like a change of sign of the magnetic exchange force already at relatively large tip-sample distances were not observed. However, in the calculations only a single Fe atom was employed to mimic the tip and relaxation effects were neglected.

On NiO(001) the magnetic exchange interaction is superposed onto the chemical interaction, where oxygen atoms are imaged as protrusions and nickel atoms are imaged as depressions. The superposition results in a height modulation on neighboring rows of nickel atoms reflecting the row-wise AF order of the NiO(001) surface [9]. Compared to NiO(001), MExFM on Fe/W(001) should reveal the $p(1 \times 1)$ surface unit cell on second and first layer Fe with a superposition of the contrast pattern of the first layer by the $c(2 \times 2)$ magnetic surface unit cell. But since on Fe/W(001) the spin-carrying *d*-electrons are delocalized and itinerant, they reach farther into the vacuum region than the localized *d*-electrons in NiO. Hence, significant differences in the distance-dependence of the exchange interaction on NiO(001) and on Fe/W(001) are expected. Moreover, Fe/W(001) is much better suited for density functional theory (DFT) than NiO, as NiO is a strongly correlated system: NiO has a partially filled 3*d*-band and strong Coulomb repulsion (a correlation effect) between the *d*-electrons makes NiO a wide-band gap insulator. Strongly correlated systems

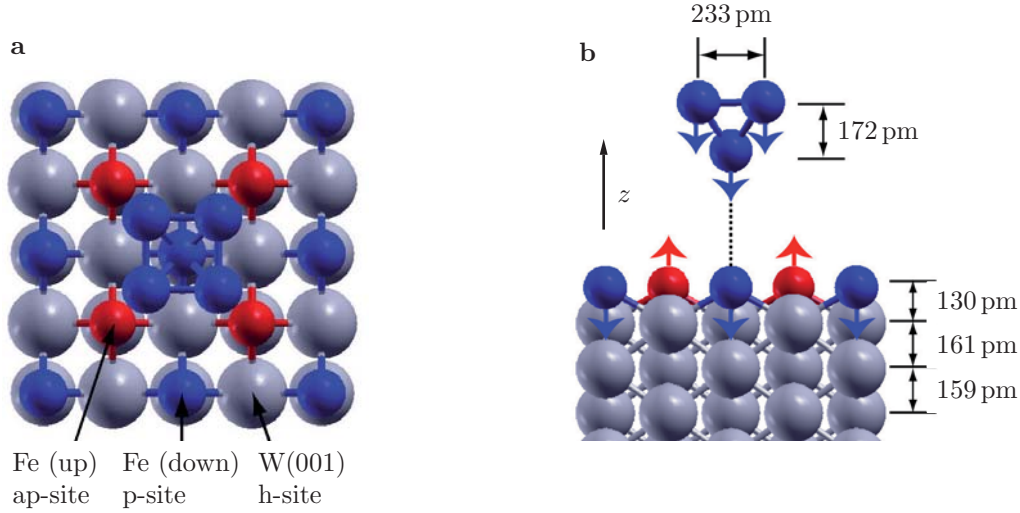


Figure 6.1: **a** Top view of a five Fe atom pyramidal tip and the Fe/W(001) surface. Sites with parallel (p-site) and antiparallel (ap-site) alignment between tip and surface Fe magnetic moments (indicated by arrows) are marked as well as the hollow-site (h-site). **b** Side view. Distances within independently relaxed tip and sample are denoted. z is defined as the tip-sample distance along the approach trajectory (dotted line) before considering relaxations due to tip-sample interactions.

have electronic structures that are neither simply free-electron-like nor completely ionic, but a mixture of both. Approximations of such systems using DFT is not straight forward.

Considering Fe/W(001), the $c(2 \times 2)$ magnetic surface unit cell of the first layer Fe has been obtained using SP-STM in 2005 [24, 119]. Having the magnetic ground state proven and the preparation at hand, Fe/W(001) is a perfect candidate to further study and understand the contrast patterns observable with MExFM. In experiment and theory notations following figure 6.1 are used. Here, a pyramidal shaped tip consisting of five Fe atoms is placed above the Fe/W(001) monolayer surface. Figure 6.1a and b show the top and side view, respectively. The positions of (anti)parallel aligned Fe atoms in tip and surface are denoted as ap-site and p-site. The visible tungsten surface atom is denoted as hollow-site (h-site).

All images presented in the following sections are considered to be acquired with magnetically sensitive and stable tips. Further tip related aspects are discussed in chapter 8.

6.1 MExFM using Ferromagnetic Tips

To simplify the system of tip and sample, Fe coated tips are chosen because if sample material is picked up by the tip, for example, during tip preparation (see chapter 8), the chemical composition remains unaltered. The tips exhibit

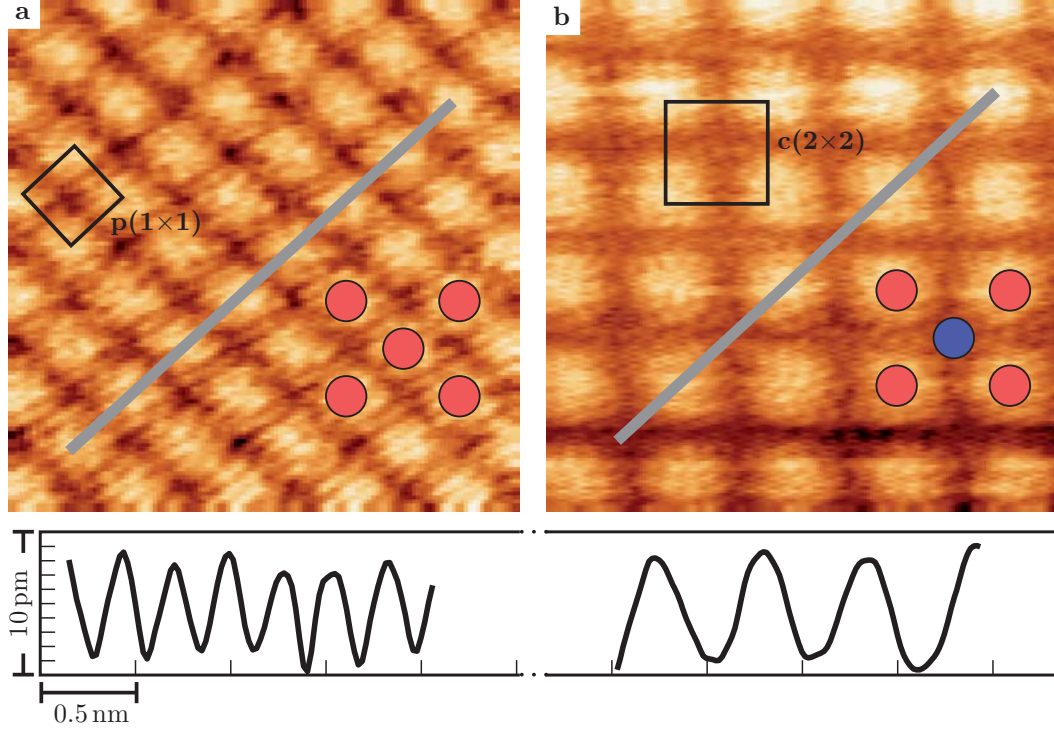


Figure 6.2: **a** Atomic resolution on a $(2 \times 2) \text{ nm}^2$ area of the Fe monolayer displaying the $p(1 \times 1)$ structural and chemical surface unit cell ($\Delta f = -28.5 \text{ Hz}$). Protrusions represent the positions of chemically identical Fe atoms (red circles). **b** MExFM image revealing a $c(2 \times 2)$ AF surface unit cell on the Fe ML ($\Delta f = -14.8 \text{ Hz}$). Only every second Fe atom appears as a protrusion (red circles). The corrugation amplitudes are about 8 pm cf. the line sections.

Parameters: $c_z = 32.5 \text{ N/m}$, $A = 5 \text{ nm}$, $f_0 = 156 \text{ kHz}$, $\vec{B} = 5 \text{ T}$.

a magnetic stray field and the foremost apex atoms carry a net magnetic moment with the spin-carrying d -electrons ranging into the vacuum region between tip and sample. To enhance the feasibility of detecting the exchange interaction between tip apex atom and sample atom and to maximize the strength of the interaction, both magnetic moments should be (anti)parallel aligned according to the HEISENBERG model (eq. 2.7). Therefore, an external magnetic field of 5 T flux density perpendicular to the sample surface is applied, that is a flux density higher than the saturation magnetic polarization of Fe, $\mu_{\text{sat}} = 2.15 \text{ T}$ [31], to align the tip magnetic moment (anti)parallel to the sample spins.

Figure 6.2 presents in **a** the chemical $p(1 \times 1)$ surface unit cell of the Fe monolayer, where all Fe atoms are chemically identical (marked in red). In **b** the monolayer is obtained with magnetic sensitivity. The spin up and spin down directions are marked in red and blue, respectively. The corrugation amplitudes in figure 6.2a and **b** are about 8 pm, each.

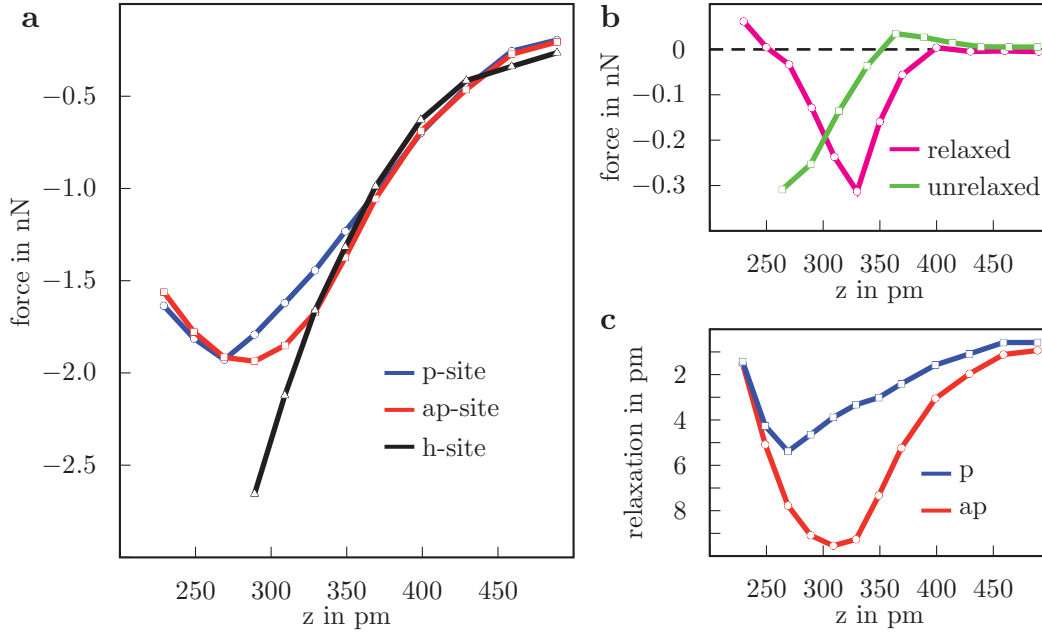


Figure 6.3: **a** Calculated force curves, $F(z)$, of a 5 atom Fe tip on h-, ap-, and p-site including relaxations. **b** Distance dependence of the magnetic exchange force $F_{\text{ex}}(z) = F_{\text{ap}}(z) - F_{\text{p}}(z)$ for the unrelaxed and the relaxed case. **c** Distance dependence of the tip apex atom relaxation towards the surface on the p- and ap-site.

Comparison to MExFM Data on NiO(001)

Different to the supermodulation contrast on NiO(001), the observed contrast in figure 6.2b is a pure $c(2 \times 2)$ structure with one spin species, either up or down, appearing as protrusion, while the other spin species (down or up, respectively) does not appear as depression or protrusion with less height, but with exactly the same corrugation as the h-site.

The magnetic corrugation amplitude on Fe/W(001) is five times larger than the previously reported value of 1.5 pm observed on NiO(001) [9], and even larger corrugations of up to 30 pm have been observed. The origin is the farther extension of the spin-carrying d -electrons of the Fe ML into the vacuum region, compared to the localized d -electrons in NiO. Moreover, the out-of-plane orientation of the magnetic moments of the Fe ML in comparison to the canted magnetic moments on NiO(001) accounts for the larger magnetic contrast. Since a rather small chemical corrugation amplitude is always observed in MExFM experiments on NiO(001), tips with a small chemical interaction might be required to approach close enough to the surface to probe the localized d -electrons.

From a practical point of view the resulting, much better SNR on Fe/W(001) in comparison to NiO(001) is very promising regarding the general applicability of MExFM to other systems. However, the contrast as shown in figure 6.2b,

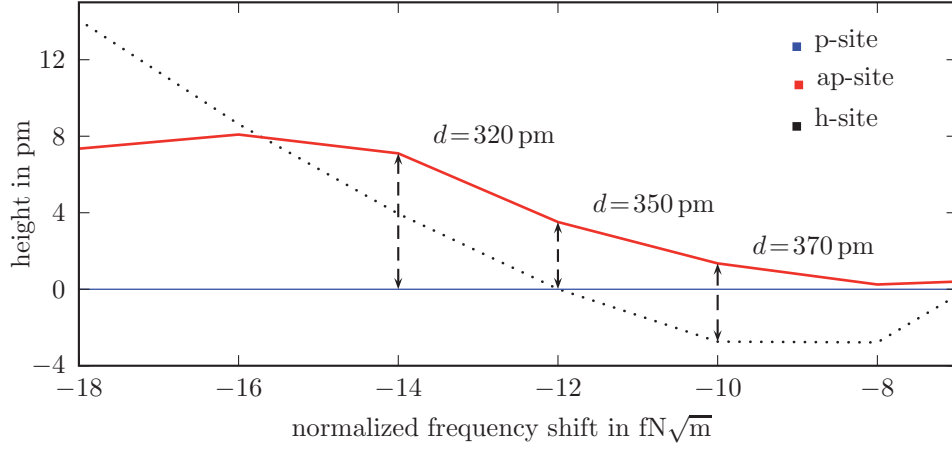


Figure 6.4: Calculated height difference between p-, ap- and h-site, respectively, depending on γ_c and hence d . The p-site defines the zero line. The black arrows indicate the maximum in corrugation amplitude at distance d .

which is the typically observed contrast in MExFM on Fe/W(001), does not simply reflect the superposition of chemical and magnetic interaction.

To understand the contrast formation on Fe/W(001) the forces acting between a multi-atom Fe tip and the sample are calculated utilizing DFT¹.

Theoretical Force-Distance Dependence

The calculations presented in figure 6.3a display an attractive interaction for the ap- and p-site up to a maximum force of -2 nN at about 270 pm tip-sample distance. On the h-site, the tip can approach the surface much closer before the repulsive regime is reached and the forces are much larger up to a maximum of -2.7 nN at about 290 pm distance. The splitting of the force curves on the p- and ap-site, as visible in figure 6.3a, defines the magnetic exchange force, that is, $F_{\text{ex}}(z) = F_{\text{ap}}(z) - F_{\text{p}}(z)$. Due to symmetry, the exchange forces on the h-site cancel out.

The data show that the ap-site of the Fe ML is energetically favorable for distances around 300 pm, that is, by about 10-60 meV for distances between 330 pm and 290 pm. This is expected following the Bethe-Slater curve in figure 2.3. However, here the AF coupling is due to the interaction of the foremost tip atom not only with the Fe atom directly underneath, but also with the four neighboring Fe surface atoms with opposite magnetic moments, which can dominate the total exchange coupling. To ensure that neither effect depends qualitatively on the tip size, calculations employing a larger Fe tip with an additional plane of 9 atoms above the previous 5 Fe atom pyramid were performed by LAZO and co-workers [102]. It could be confirmed that

¹Details on computation can be found in [102].

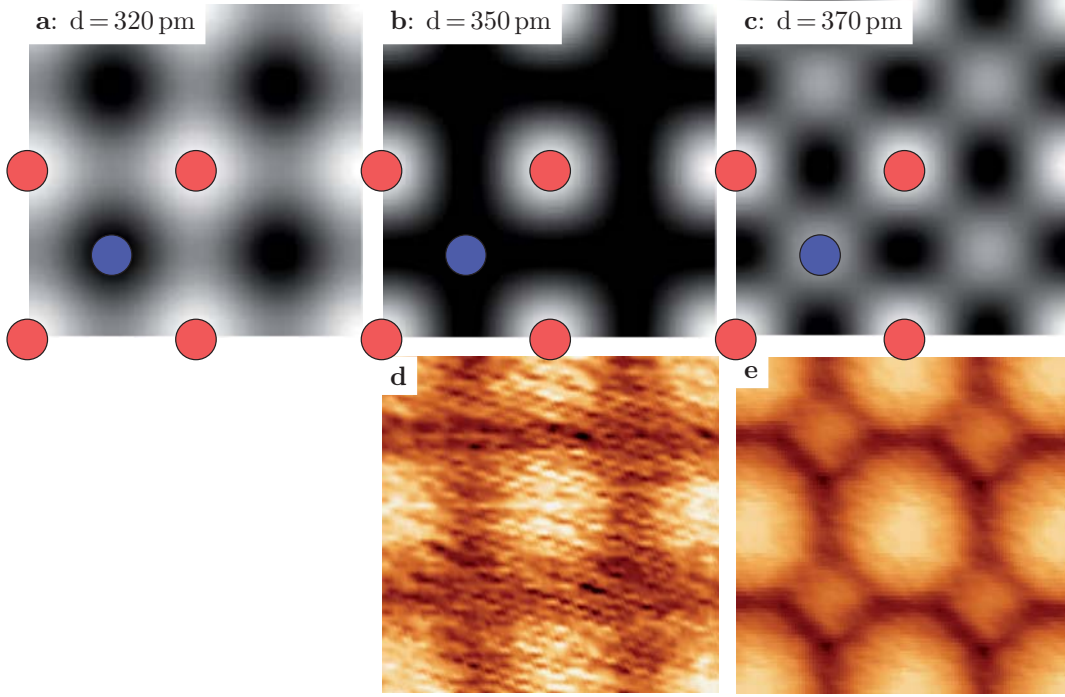


Figure 6.5: **a-c** Simulated MExFM images at $\gamma_c = -14 \text{ fNm}^{1/2}$ in **a**, $-12 \text{ fNm}^{1/2}$ in **b**, and $-10 \text{ fNm}^{1/2}$ in **c** corresponding to $d = 320 \text{ pm}$ in **a**, 350 pm in **b**, and 370 pm in **c**, respectively. **d-e** MExFM images displaying two different distance dependent contrast patterns of the AF $c(2 \times 2)$ surface unit cell using Fe and Cr coated tips, respectively. Parameters: **d** $\Delta f = -14.8 \text{ Hz}$, $c_z = 32.5 \text{ N/m}$, $A = 5 \text{ nm}$, $f_0 = 156 \text{ kHz}$, $B = 4.5 \text{ T}$. **e** $\Delta f = -8 \text{ Hz}$, $c_z = 146 \text{ N/m}$, $A = 3.83 \text{ nm}$, $f_0 = 187 \text{ kHz}$, $B = 5 \text{ T}$.

both, sign and distance-dependence of the magnetic exchange interaction, are unchanged.

Comparison with Simulated MExFM Images

To quantitatively compare calculated forces and experimental images it is necessary to simulate images using the theoretically derived distance dependence of the forces, since it is not possible to deduce tip-sample forces from the experimental images. For this simulation, performed by CACIUC and HÖLSCHER [50], long-range tip-sample interaction caused by the van der Waals forces acting between the macroscopic tip and the sample have to be considered. As in other studies [75, 86, 87] the macroscopic part of the tip is modeled by a sphere with radius R . The long-range van der Waals force is added corresponding to eq. 3.2 by $F_{\text{vdW}}(z) = -(A_H R)/(6z^2)$. The values assumed are $R = 8 \text{ nm}$ and $A_H = 0.1 \text{ aJ}^2$. The total tip-sample force $F_{\text{ts}} = F_{\text{sr}} + F_{\text{vdW}}$ is obtained, with $F_{\text{sr}} = F_{\text{p}}, F_{\text{ap}}$, or F_{h} at the three distinct lattice sites. Δf can

²Since there is no known better value for Fe, this typical value is used. The overall qualitative result does not change for reasonable values of R and A_H .

be calculated according to eq. 3.13. For simplicity, the normalized frequency shift γ is used, because this quantity is independent of the actual experimental parameters A , c_z and f_0 (cf. chapter 3.6). In order to simulate constant γ images a suitable value γ_c is chosen and the corresponding nearest tip-sample distance at the lower turnaround point of the cantilever oscillation, d as denoted in figure 3.1, is determined numerically by solving $\gamma(d) = \gamma_c$. As a result the corrugation amplitudes at the three distinctive lattice sites as a function of γ and hence d are obtained. In figure 6.4 the height of the ap- and h-site is plotted with respect to the p-site. Based on these curves complete MExFM images are simulated using the first two non-constant terms of a two-dimensional Fourier expansion [64].

The simulated images displayed in figure 6.5a-c clearly demonstrate that the magnetic contrast depends sensitively on the nearest tip-sample distance d . At large d , figure 6.5c, the chemical contrast dominates and the ap- and p-site appear as local maxima of only slightly different height due to a small exchange force of about 0.06 nN (c.f. figure 6.3b). At very small tip-sample distance, figure 6.5a, the magnetic forces dominate and Fe atoms with opposite magnetic moments appear as minima and maxima, respectively. At intermediate distance, p- and h-site exhibit nearly the same height level and become indistinguishable, figure 6.5b. At the crossing point in figure 6.4 they are exactly equal and only the ap-sites appear as maxima. Here chemical and magnetic forces are both present and of considerable magnitude, but the total forces at p- and h-site are equal. The contrast in figure 6.5b matches the experimentally observed magnetic $c(2 \times 2)$ surface unit cell in figure 6.2, indicating that the image has been obtained in the intermediate tip-sample distance regime. Up to now, using Fe and Cr coated tips, a contrast as in figure 6.5a was never obtained experimentally, probably because stable imaging is difficult at such close distances (cf. chapters 4.2 and 8).

However, contrast patterns similar to figure 6.5b and c are observed in different experiments. Figure 6.5d shows a contrast comparable to figure 6.5b with a corrugation of 10 pm, obtained with a Fe coated tip. Figure 6.5e shows a contrast comparable to figure 6.5c with a corrugation of 6 pm between ap- and p-site, and 10 pm between h- and ap-site, hence 4 pm between h- and p-site. For a better visualization figure 6.5e is unit cell averaged³.

Role of Relaxation

The forces on ap- and p-site are calculated with and without relaxation effects of tip and sample. The difference in force between ap- and p-site, that is, the exchange force, is plotted for both cases in figure 6.3b. Obviously, the curves exhibit a significantly different distance dependence: when relaxation is included, the onset of large magnetic exchange forces shifts towards larger

³An experimental image of a periodic surface typically contains many unit cells, which can be used to obtain an averaged unit cell with a much better SNR [9].

tip-sample distances, which facilitates their experimental detection. A change of sign at large tip-sample distances as it appears for the unrelaxed case is not observed for the relaxed case. The differences are caused by the relaxation of the tip apex atom which depends on its local magnetic configuration with respect to the approached surface atom. Figure 6.3c shows that the tip apex atom on the ap-site relaxes about 5 pm closer towards the surface atom than on the p-site which enhances the exchange interaction. The comparison emphasizes the importance of relaxation effects and hence the insufficiency of the one-atom-tips used in prior calculations for NiO [125].

Moreover, it could be shown that using only a single Fe atom as tip, the magnetic exchange interaction is qualitatively and quantitatively different from those with multi-atom tips. In particular, the magnetic exchange force is artificially enhanced at large tip-sample separation, but decreases in magnitude already at much larger distance than for multi-atom tips [102]. These differences are attributed to the unrealistic large and rigid magnetic moment of a single Fe atom due to the missing hybridization with base atoms. In addition, magnetic exchange interactions with base atoms of the tip contribute to the total exchange force on the tip. Therefore, it is crucial to use multi-atom tips and to include relaxation effects in order to obtain the correct sign and distance-dependence of the exchange interactions [102].

6.2 MExFM using Antiferromagnetic Tips

Discussed in chapter 4.2, Cr coated tips allow for a more stable detection of exchange forces, even in a wider distance range than Fe coated tips. However, the foremost tip atom of such tips might be either Cr or Fe, as tip modifications are frequently observed before an exchange contrast appears and Fe might be easily picked up during the experiment (see chapter 8). Atomic resolution and magnetic contrast obtained with a Cr coated tip are presented in figure 6.6a and b, respectively. Both contrasts are qualitatively and quantitatively comparable to figure 6.2. Confering the line section in figure 6.6 the corrugation amplitude is about 8 pm and, again, only every second Fe atom is imaged as protrusion within the MExFM image. This contrast is typically observed in MExFM images on Fe/W(001) when using Cr coated tips.

6.3 MExFM in Zero Field

A MExFM image of $(5 \times 5) \text{ nm}^2$ in size is shown in figure 6.7. The image has been obtained without applying an external magnetic field and using a modified Cr coated tip, which is, the tip already changed its state several times during the experiment due to slight tip modifications (cf. chapter 8). The $c(2 \times 2)$ magnetic surface unit cell is sketched. A magnetic defect is visible

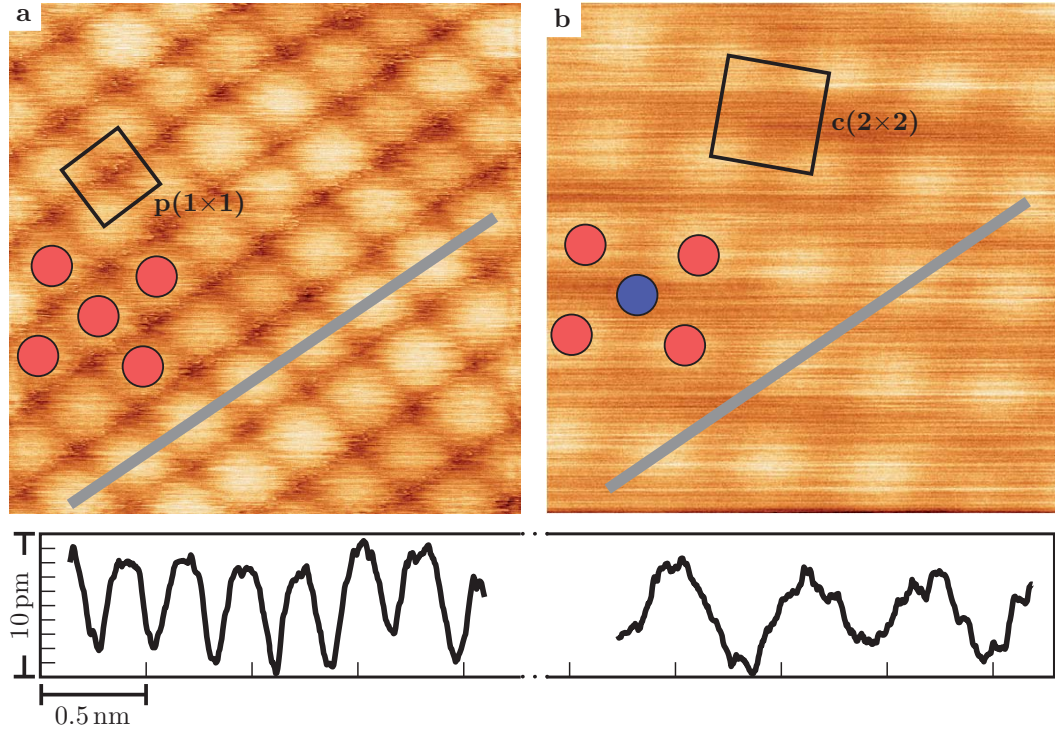


Figure 6.6: **a** Using a Cr coated tip, atomic resolution on a $(2 \times 2) \text{ nm}^2$ area of the Fe monolayer displaying the $p(1 \times 1)$ structural and chemical surface unit cell ($\Delta f = -17 \text{ Hz}$) is resolved. Protrusions represent the positions of chemically identical Fe atoms (red circles). **b** MExFM image of the $c(2 \times 2)$ AF surface unit cell on the Fe ML ($\Delta f = -27 \text{ Hz}$) obtained with the same Cr coated tip. Only every second Fe atom appears as a protrusion (red circles). The corrugation amplitude is about 8 pm cf. line sections.

Parameters: $c_z = 143 \text{ N/m}$, $A = 2.81 \text{ nm}$, $f_0 = 185 \text{ kHz}$, $B = 4.5 \text{ T}$.

in the lower part of the image. The data demonstrates that the external field is not necessary to align the magnetic moment of the foremost tip atom (anti)parallel to the surface atoms to achieve magnetic contrast. Instead, a controllable manipulation of the magnetic moment of the foremost tip atom whilst scanning the surface in close distance will eventually lead to a magnetic sensitive tip and the detection of magnetic exchange forces. Such tip related aspects are further discussed in chapter 8.

6.4 MExFM near Structural Defects

Numerous types of defects of the Fe monolayer, for example, point defects and contaminations, are known from atomic resolution studies. Such defects are of huge interest, because they are able to locally change the electronic structure of the surface, leading to a change of the local exchange interaction and hence

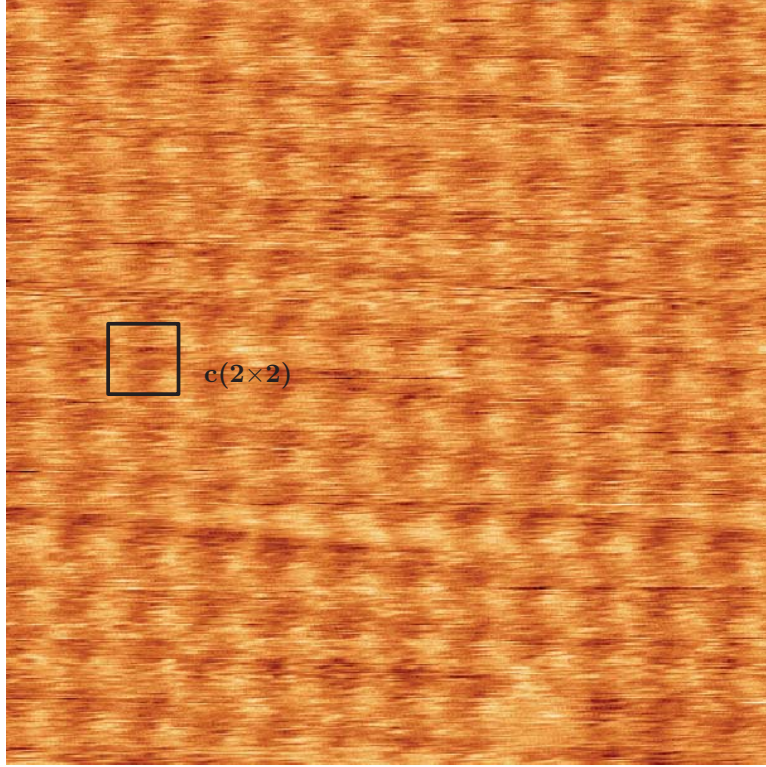


Figure 6.7: $(5 \times 5) \text{ nm}^2$ MExFM image obtained using a Cr coated tip in zero field. A defect is visible in the lower part of the image.
Parameters: $\Delta f = -33.3 \text{ Hz}$, $c_z = 154.2 \text{ N/m}$, $A = 3 \text{ nm}$, $f_0 = 193 \text{ kHz}$, $B = 0 \text{ T}$.

to uncompensated spins. Understanding the influence of defects on the local magnetic exchange might help to clarify phenomena like the exchange bias (EB): while its underlying physics are well described in literature [43, 44], its small size can only be explained by a vast inactive majority of AF surface spins, because only a few uncompensated spins contribute to the effect [126, 127]. Possible sources of uncompensated spins are spin-flop coupling [128, 129], grain size [130, 131], domains due to interface roughness [132], and non-magnetic defect sites [133, 134]. Indeed, as the EB tends to be smaller in epitaxial bilayers than in polycrystalline ones, defects seem to play an important role in the pinning of the magnetization direction of the interface spins.

Figure 6.8b and c show $(130 \times 160) \text{ pm}^2$ close-ups of the two most frequently observed magnetic defects in the Fe monolayer, recorded without a tip change in between, hence with identical tip state, as can be seen from the full image in figure 6.8a. The defects can be distinguished unambiguously from adsorbates, which can be moved along atomic rows on the surface when the short-range forces overcome the forces keeping them in place, as shown in the lower right of figure 6.8a: the adatom of 120 pm height jumps right behind the tip from one p-site to the next p-site down below.

To correlate the defects in figure 6.8**b** and **c** with the lattice structure, ap- and p-site are marked in red and blue, respectively. In figure 6.8**b** the defect appears as bright protruding area while in **c** the defect appears elongated and depressed. The origin of the defects is unclear, as no correlation can be made directly with the chemical structure due to the magnetic contrast, where only one spin species is obtained. Besides the possibility, that magnetic and non-magnetic impurities are measured, in **b** two p-site atoms might be missing and a circular structure of charge accumulation is obtained. While p-site atoms are missing, the maxima (ap-sites) above and below the missing atoms seem to approach towards each other by 100 pm. The relaxing maxima are marked by yellow circles. On the other hand, a h-site defect (W-vacancy) might exist. Whether the defect is filled with Fe or stays empty, in both cases, neighbouring Fe atoms would relax towards the vacancy. Since the AF structure of Fe is induced by hybridization with the substrate, the atoms on top of the vacancy act like the unsupported Fe monolayer or like second layer iron. Both are FM aligned and four maxima with reduced corrugation show up. In **c**, two ap-site atoms might be missing, hence a triangular shaped depletion of charge is obtained as marked by yellow triangles. Even one and the same single point defect might be measured, but in **b** the missing atom is just a single p-site atom, while in **c** a single ap-site atom could be missing.

A further, profound analysis of magnetic defects has not yet been performed and comparison with theory aiming to further characterize the magnetism and structure at the tip apex as well as to understand the contrast formation and the exact shape of the defects will be necessary.

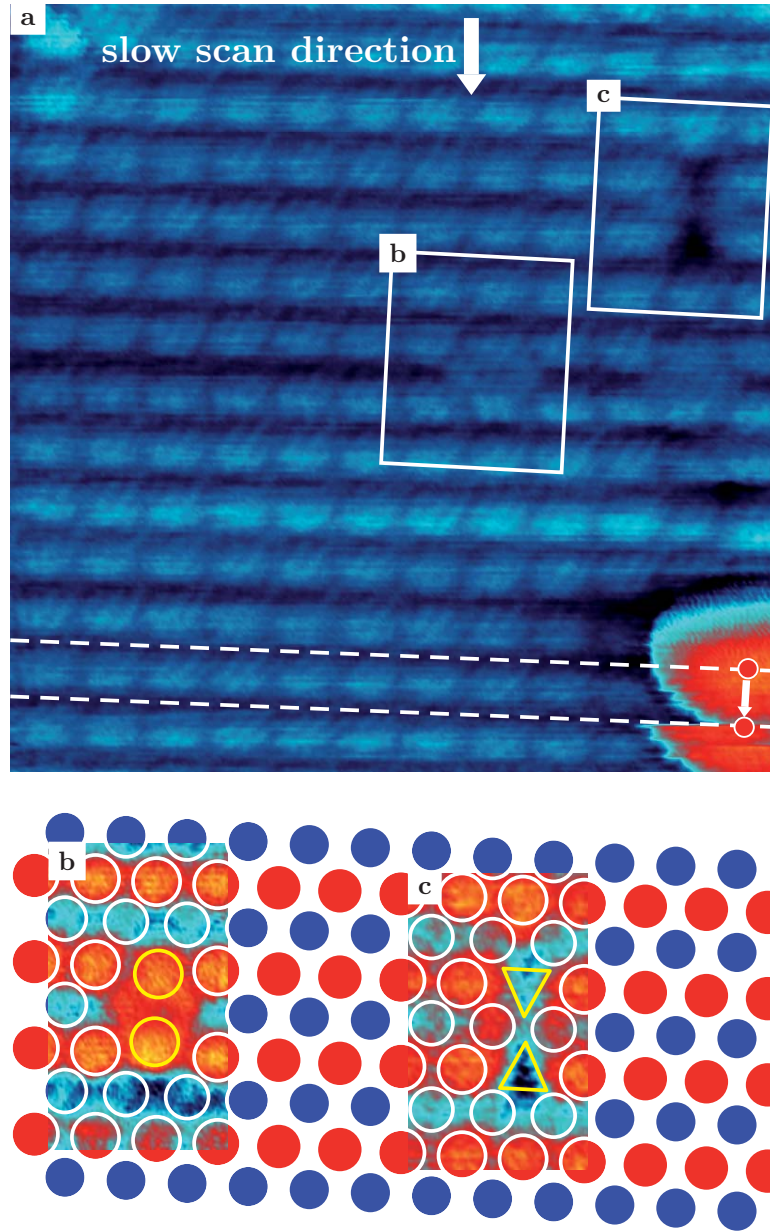


Figure 6.8: **a** $(5 \times 5)\text{nm}^2$ MExFM image obtained using a Cr coated tip. Whilst keeping its magnetic sensitivity, the tip drags an adsorbate from one p-site to another along the slow scan direction. **b** and **c** $(130 \times 160)\text{pm}^2$ MExFM close-ups of the defects in **a**. The lattice structure with spin-up and spin-down atoms is sketched. The resulting defect induced structure is purely spin-dependent. Parameters: $\Delta f = -20.7\text{ Hz}$, $c_z = 33.9\text{ N/m}$, $A = 2.7\text{ nm}$, $f_0 = 159\text{ kHz}$, $B = 4.5\text{ T}$.

6.5 Distance Dependence of MExFM Contrast

Using different Cr coated tips contrast patterns similar to figure 6.5b and c are observed in different experiments.

A contrast as simulated in figure 6.5a was not observable experimentally up to now, most probably due to too strong short range interactions causing instabilities at the tip end leading to an irreversible loss of the exchange contrast. Even a smooth change of the observed contrast when approaching the surface from chemical resolution beyond 370 pm (compare figure 6.3a), to the magnetic exchange interaction emerging as supermodulation at 370 pm tip-sample distance, and to a domination of the exchange interaction induced contrast at 320 pm distance and even closer was not observable experimentally.

The consecutive images in figure 6.9 are recorded using the same Cr coated tip, but each image is obtained at different Δf , hence at different tip-sample distance. The corrugation amplitudes measured at larger separation, 6.9a-c, are only little above the noise level. The data have been evaluated along different crystallographic axes and the averaged corrugation amplitudes between p-, ap- and h-site were plotted versus the normalized frequency shift as in figure 6.4. The normalized frequency shift has been calculated according to eq. 3.15 using $A = \pm 2.81$ nm, $f_0 = 185$ kHz and $c_z = 143$ N/m. Simulated data, figure 6.4, and experiment, figure 6.9h, are qualitatively in reasonable agreement concerning the contrast variation between ap- and p-site. However, the corrugation amplitude on the h-site has a very low signal and is even not directly visible in the images.

While for the theoretical evaluation presented in figure 6.4 only one specific tip, namely Fe, in a specific orientation, namely pyramidal with the four atom base being parallel to the surface lattice (cf. figure 6.1), has been considered, the real tip used within this experiment might look different. Confering to chapter 8, the tip might be either Fe or Cr terminated, it might be of asymmetric structure and it might be unstable. Actually, a magnetically unstable tip leads to the shifting of the contrast in 6.9g. Unstable tips leading to changes in contrast are further discussed in chapter 8.

Consequently, the differences in quantity of ap- and p-site between figures 6.4 and 6.9h and the nearly total lack of signal on the hollow-site in figure 6.9h might be due to tip instabilities leading to a more pronounced relaxation of the foremost tip apex atoms. Such relaxations lead to different results in the calculated force, as indicated in figure 6.3c. A strong relaxation will further lead to a misinterpretation of the closest tip-sample distance d and, hence, to a misinterpretation of the experimentally obtained γ -values.

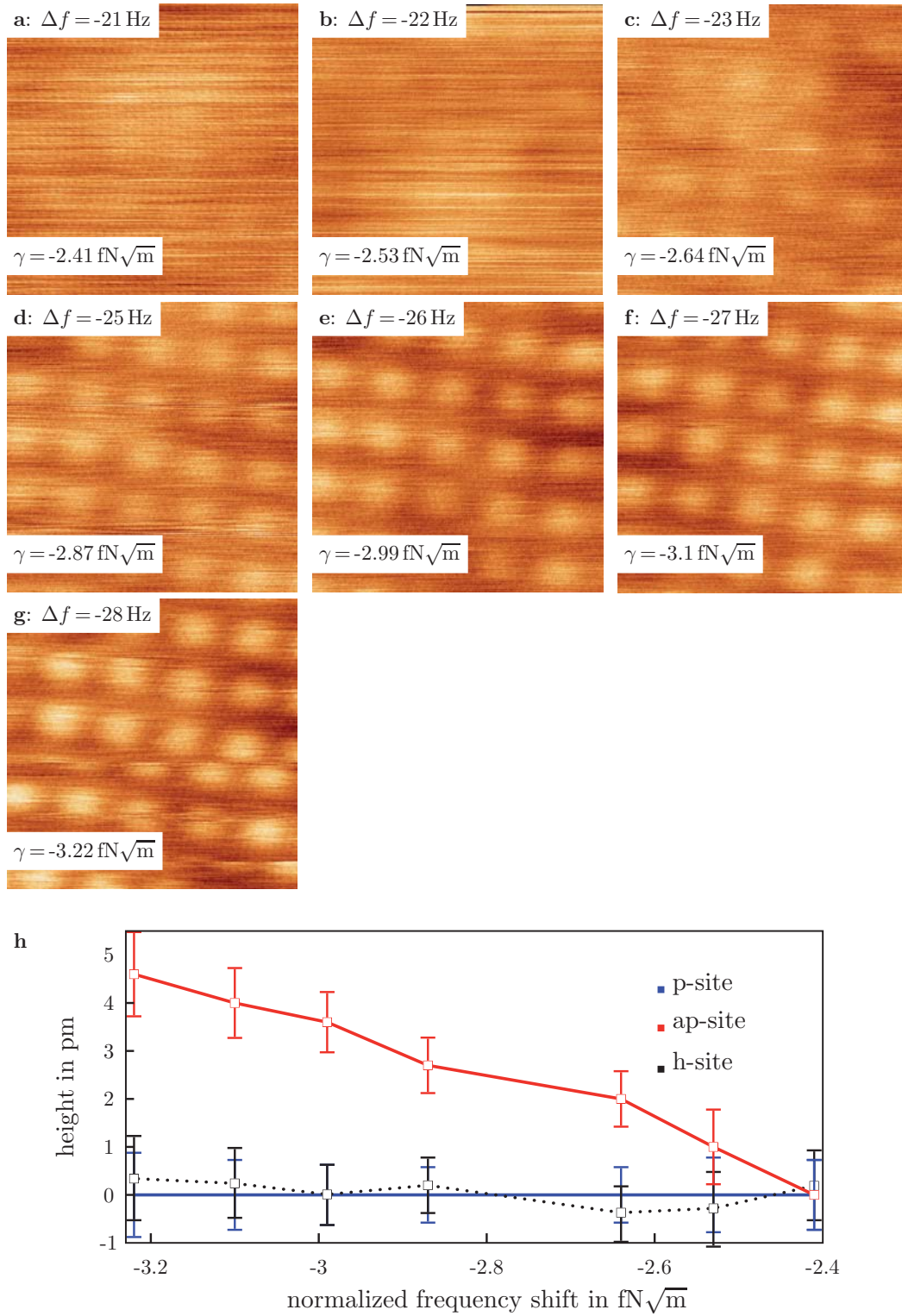


Figure 6.9: **a-g** Consecutive MExFM images of the same surface area obtained using the same Cr coated tip but with increasing tip-sample interaction (decreasing tip-sample distance) from $\Delta f = -21$ Hz in **a** to $\Delta f = -28$ Hz in **g**. **h** Corrugation amplitudes of ap- and h-site with respect to the p-site versus normalized frequency shift.

Parameters: $c_z = 143$ N/m, $A = 2.81$ nm, $f_0 = 185$ kHz, $B = 4.5$ T.

CHAPTER 7

MAGNETIC EXCHANGE FORCE SPECTROSCOPY ON Fe/W(001)

Up to now, magnetic exchange interactions across a vacuum gap for a tip-surface geometry were considered only theoretically utilizing density functional theory (DFT) [10,102,125,135]. However, it is possible to directly measure the distance dependence of the magnetic exchange interaction across a vacuum gap by applying the spectroscopic mode of MExFM, that is, magnetic exchange force spectroscopy. Here, the feasibility of MExFS is demonstrated for the first time: recording $\Delta f(z)$ on Fe atoms with different spin orientation, $\Delta f_{\text{ap}}(z)$ and $\Delta f_{\text{p}}(z)$, allows to directly access the magnetic exchange energy between ap- and p-site of the surface magnetic moments across the vacuum gap between tip and sample (cf. chapters 3.5 and 3.6).

The main prerequisite to perform MExFS is a structurally stable tip that shows magnetic sensitivity. Such a tip can be easily identified according to chapter 8. To allow for precise and direct determination of single spectroscopy curves obtained on the ap- and p-site of the Fe/W(001) monolayer, three dimensional sets of spectroscopy curves (cf. chapter 3.5) are recorded with high lateral bit resolution. Further using the knowledge of the direction of the atomic spin from chapter 6, $\Delta f_{\text{ap}}(z)$ and $\Delta f_{\text{p}}(z)$ can be unambiguously identified and extracted.

7.1 MExFS using Stable Tips

In figure 7.1 a 3D- $\Delta f(z)$ -data set obtained using the spectroscopy acquisition method (i) is displayed. The atomically resolved $c(2 \times 2)$ checkerboard spin structure of the iron monolayer is visible at the bottom in the MExFM data. The slice through the $\Delta f(x, y, z)$ -field along the $[100]$ -direction reflects the spatially resolved distance dependence of the tip-sample interaction. Note that a larger attractive tip-sample interaction corresponds to maxima in topography

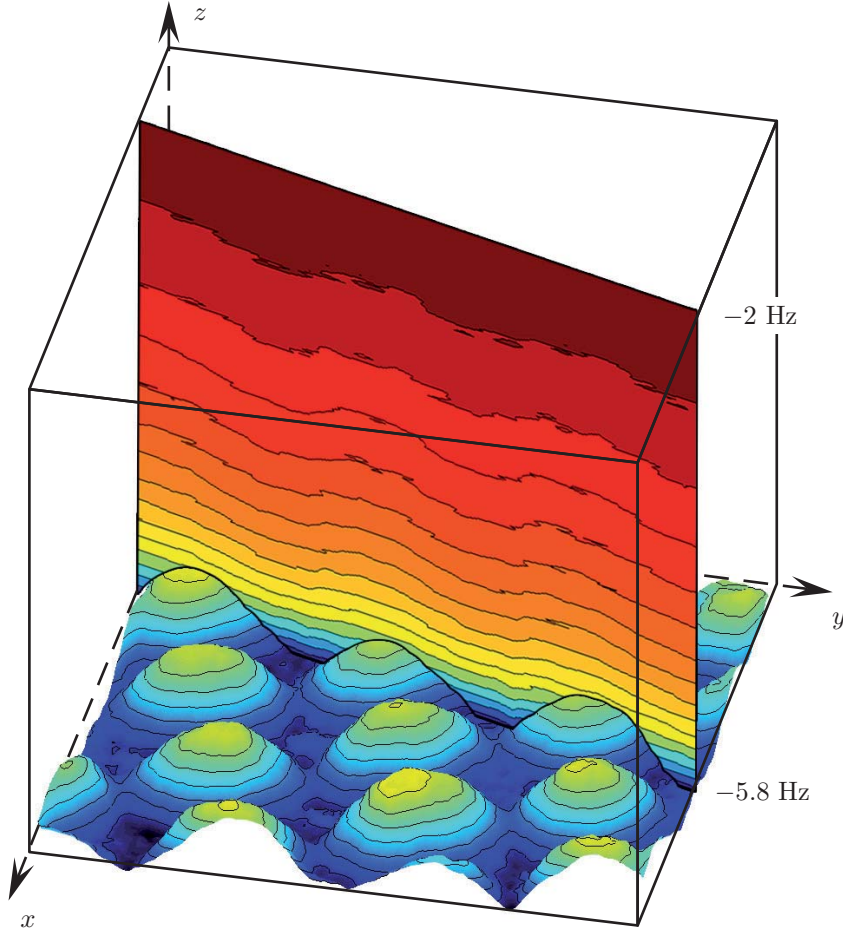


Figure 7.1: 3D magnetic exchange force spectroscopy data (3D-MExFS). The topography visualized at the bottom is recorded with 256×256 data points on $(1.5 \times 1.5) \text{ nm}^2$. Hence the bit resolution is about 6 pm per data point. At $\Delta f_{\text{stab}} = -5.8 \text{ Hz}$ the topography reveals the AF structure of the monolayer with a corrugation amplitude of 15 pm. The slice through the $\Delta f(x, y, z)$ data set (32×32 curves with $\Delta z = 1.17 \text{ pm}$ ranging from $z_{\text{start}} = 0 \text{ pm}$ to $z_{\text{end}} = 300 \text{ pm}$) along oppositely oriented atomic magnetic moments in $[100]$ -direction shows the site and distance dependence of the magnetic exchange interaction. The data have been obtained using a Cr coated tip.

Parameters: $c_z = 145.5 \text{ N/m}$, $A = 3.83 \text{ nm}$, $f_0 = 187 \text{ kHz}$, $Q = 318000$, $B = 5 \text{ T}$.

and minima in frequency shift. Using such a 3D-data set, the individual $\Delta f(z)$ -curves on surface atoms with oppositely oriented atomic magnetic moments are unambiguously identified.

Figure 7.2 shows two such curves obtained above maximum ($\Delta f_{\text{max}}(z)$: red) and minimum ($\Delta f_{\text{min}}(z)$: blue). The data has been acquired using the spectroscopy acquisition method (ii), hence the magnetic exchange induced frequency shift (black) is directly extracted according to eq. 3.12. This fre-

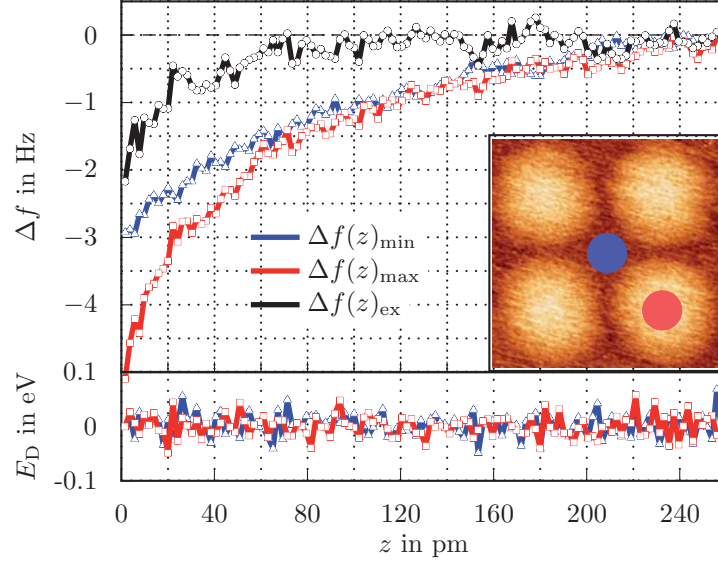


Figure 7.2: Two individual $\Delta f(z)$ -curves recorded on Fe atoms with oppositely oriented magnetic moments, indicated in the corresponding topography in red and blue on maximum and minimum, respectively, using spectroscopy acquisition method (ii). The curves split smoothly into two branches at small tip-sample distance, allowing to obtain the black difference curve, which is a measure of the magnetic exchange interaction. The simultaneously recorded dissipation shows no loss of energy into non-conservative interactions indicating a stable tip.

Parameters: $\Delta f_{\text{stab}} = -2.5$ Hz, $\Delta z = 2$ pm, $c_z = 145.5$ N/m, $A = 3.83$ nm, $f_0 = 187$ kHz, $B = 5$ T, $Q = 318000$.

quency shift is used to calculate the magnetic exchange energy $E_{\text{ex}}(z)$ using the DÜRIG [85] algorithm presented in chapter 3.6. In the lower part of the image the simultaneously recorded dissipation E_D is plotted. The dissipation shows no additional non-conservative force occurring between tip and sample on approach. Furthermore, the topography in the lower right part of the image, used to indicate the single spectroscopy locations, either maximum (red) or minimum (blue), shows symmetrical atom shapes. The quality of the MExFM image and zero dissipation on approach indicate a stable tip apex.

Figure 7.3 again shows two curves obtained above maximum ($\Delta f_{\max}(z)$: red) and minimum ($\Delta f_{\min}(z)$: blue). This data set has been acquired using the spectroscopy acquisition method (i), hence the curves are shifted with respect to each other according to the difference in z_{start} , that is, to the corrugation measured in the MExFM data (cf. figure 3.7). Already being cut-off at largest tip-sample distance, on shortest tip-sample approach the data hence deviate in z by the corrugation amplitude. After shifting the data the magnetic exchange induced frequency shift is extracted according to eq. 3.12 ($\Delta f_{\text{ex}}(z) = \Delta f_{\max}(z) - \Delta f_{\min}(z)$: black) within the overlapping region and can again be used to calculate the magnetic exchange energy $E_{\text{ex}}(z)$ using

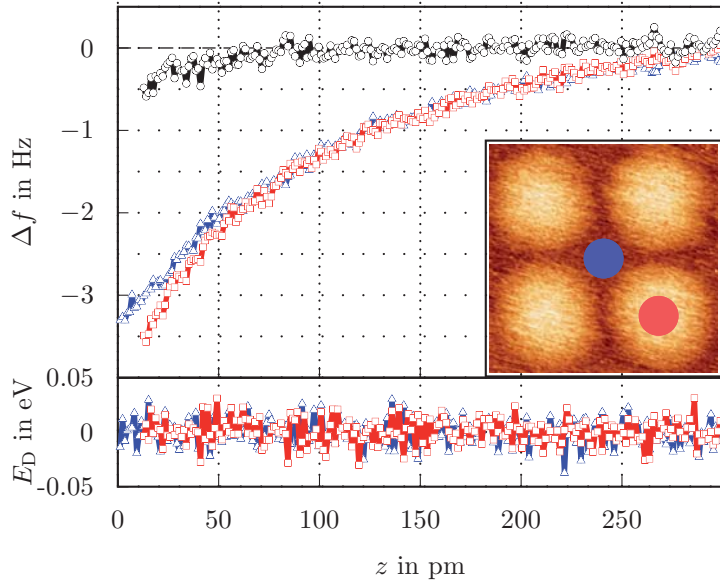


Figure 7.3: Two individual $\Delta f(z)$ -curves recorded with a non-dissipative tip on Fe atoms with oppositely oriented magnetic moments, indicated in the corresponding topography in red and blue on maximum and minimum, respectively, using spectroscopy acquisition method (i). The curves split smoothly into two branches at small tip-sample distance, allowing to obtain the black difference curve, which is a measure of the magnetic exchange interaction.

Parameters: $\Delta f_{\text{stab}} = -5.8$ Hz, $\Delta z = 1.17$ pm, $c_z = 145.5$ N/m, $A = 3.83$ nm, $f_0 = 187$ kHz, $B = 5$ T, $Q = 318000$.

the DÜRIG [85] algorithm. The simultaneously recorded dissipation E_D shows no additional non-conservative force occurring between tip and sample on approach and the topography in the lower right part of the image is similar to figure 7.2. Again, the quality of the MExFM image and zero dissipation on approach thus indicate a stable tip apex.

Magnetic Exchange Energy in AF Iron

The exchange energies obtained experimentally using both methods in three 3D-MExFS data sets show qualitatively the same results, with the only difference being the range of the obtained data, as displayed in figure 7.4. The orange curve is taken from figure 7.2. The blue curve is taken from figure 7.3. The red curve is taken from another data set and has been averaged over several $\Delta f_{\text{ex}}(z)$ -curves. The frequency shift data are fitted prior to the energy conversion to avoid artifacts due to noise (cf. chapter 3.6). The magnitude of the magnetic exchange interaction closest to the surface is about 60 meV, which is the largest magnetic exchange interaction observed. Trying to adjust smaller tip-sample separations frequently resulted in instable conditions and irreversible tip changes. Note that the relative spin orientation with respect

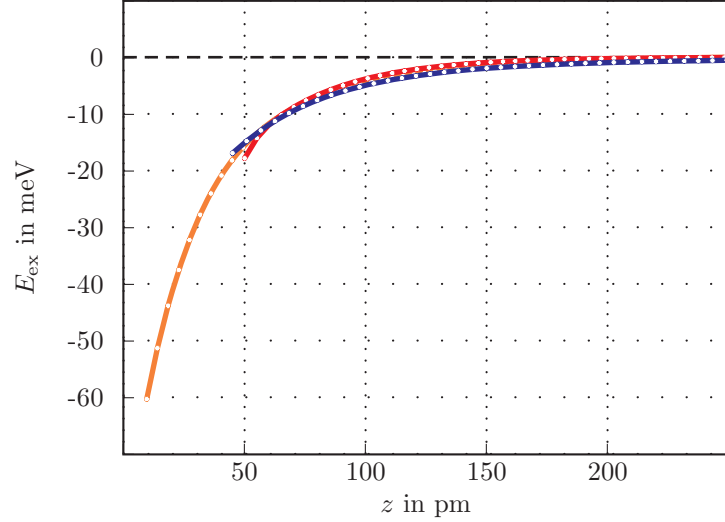


Figure 7.4: Exchange energy, E_{ex} , obtained from three 3D-MExFS data sets. The curves have a different range, but are cut off at 250 pm, where the exchange interaction is approaching zero. Note that $z=0$ pm is arbitrarily chosen and the corresponding z -scales are shifted with respect to each other until the curves overlap. The orange curve is taken from figure 7.2, while blue and red are taken from figures 7.3 and 7.7, respectively. At small tip-sample distance all energies are negative indicating antiferromagnetic exchange. No sign change is visible in all curves and the curves show the same slope, but differ only in acquisition range. The maximum exchange energy value obtained is $E_{\text{ex}} \approx 60$ meV.

to the tip is not known *a priori* from the experiment. However, using the assignment of ap- and p-site as suggested by theory already in chapter 6 leads to a negative exchange energy when performing the subtraction according to eq. 3.12. Negative exchange energy indicates antiferromagnetic coupling between the Fe atoms. Hence the assignment of ap- and p-site within the MExFM data is justified by comparison with theory.

As will be demonstrated in chapter 8, the tips used to perform 3D-MExFS do eventually change their tip state from magnetically insensitive to magnetically sensitive either spontaneously, or by intentionally induced tip changes in close proximity to the surface, leading to a re-configuration of foremost tip apex atoms prior to the spectroscopy. Hence, it is not clear with unambiguity, which species, either Fe or Cr, really terminates the tip. To allow for a comparison with theoretical energy data, LAZO and co-workers [136] performed first-principles DFT calculations using more realistic multi-atom tips: the tips are modeled by a square-based pyramid of 14 atoms, instead of five as presented in chapter 6.1. Four different tip apices are considered: (i) a pure Cr apex, (ii) an Fe terminated Cr apex, (iii) a pure Fe apex, and (iv) a Cr terminated Fe apex. They reflect structurally probable tip states, which could occur after collision between the used Cr coated tips and the Fe monolayer.

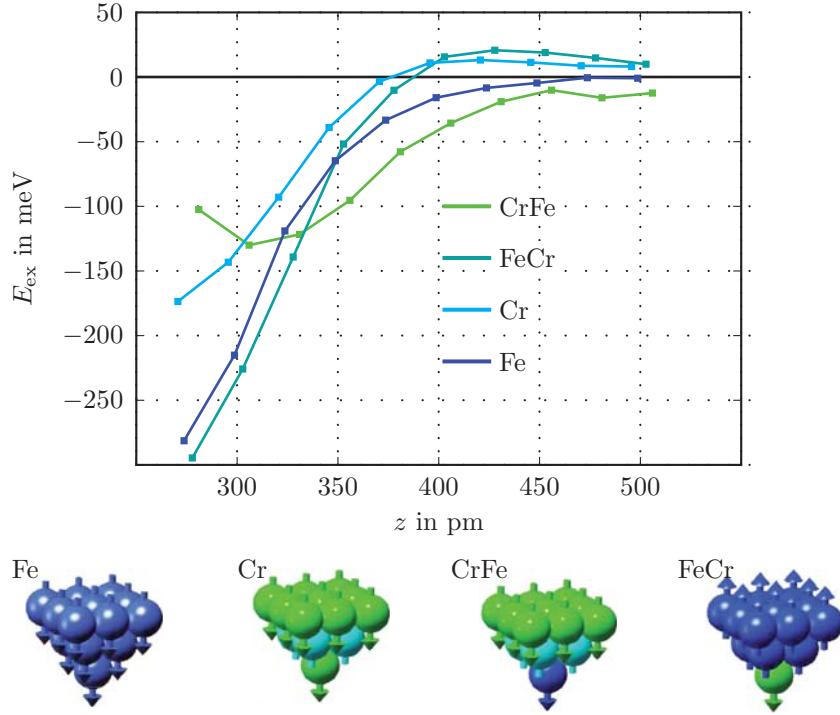


Figure 7.5: Magnetic exchange energy E_{ex} for four different tips containing either Cr or Fe or both. While only Cr-terminated tips exhibit a sign change, Fe-terminated tips show pure antiferromagnetic coupling (negative exchange energy). The tip models used within the DFT calculations performed by LAZO and co-workers [136] are sketched below.

Tip and surface are initially relaxed independently before considering the coupled system. Note that as in the experimental situation the separation z in the coupled system is defined as the distance between the tip apex atom and the Fe surface atom underneath before considering relaxations.

To calculate the magnetic exchange energy $E_{\text{ex}} = E_{\text{ap}} - E_{\text{p}}$ the total interaction energy is first determined on top of a surface Fe atom with parallel (E_{p}) and antiparallel (E_{ap}) orientation of the magnetic moment, respectively. This approach is equivalent to subtracting the data obtained on minima and maxima in the experimental data, where the relative spin orientation is not known *a priori*. Upon approaching the tip to the surface along the z -direction, all Fe atoms of the monolayer, the first layer of W atoms, and the five foremost apex atoms are allowed to relax at every tip-sample distance. This procedure is performed for all four tips and the results are presented in figure 7.5.

The theoretically derived energies in figure 7.5 are on the order of -100 meV at a distance range of 300 pm to 350 pm, hence favouring antiferromagnetic alignment. Moreover, only Cr-terminated tips exhibit a characteristic change of sign at large distances due to a transition from a direct to an indirect exchange mechanism [137]. A detailed analysis of the calculations shows that

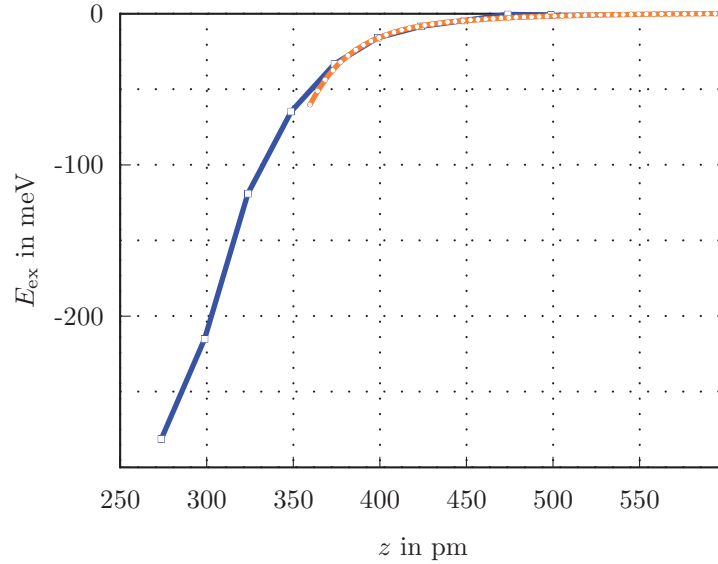


Figure 7.6: Comparison of the experimentally obtained magnetic exchange curve with largest energy and the theoretical curve for a pure Fe tip. Distance dependence and energy range are in very good agreement. Note that the absolute z -scale is only known for the theoretical data. Hence, the experimental data is shifted to obtain best overlap.

second layer tip atoms, which are AF coupled to the terminating tip apex atom, contribute with opposite sign to E_{ex} [10,102,136], resulting in a relatively weak distance dependence for the pure Cr tip and the Fe terminated Cr base tip. On the other hand, Fe base atoms contribute much less than Cr base atoms to the total E_{ex} . Therefore, both tips with an Fe base exhibit a stronger distance dependence at small distances than those with Cr base [138].

In none of the performed spectroscopic experiments a sign change was ever observed, indicating that surface Fe atoms have been picked up, hence forming an Fe tip apex. Thus, the Cr-terminated tips are excluded for a direct comparison of experiment and theory due to their transition from FM to AF coupling. Moreover, comparing the slope of the experimental curve with the slope of both Fe-terminated tips shows that the experimental curve nicely fits to the pure Fe tip, but deviates from the CrFe tip in the energy regime between 0 meV and 20 meV. For a direct comparison the experimentally obtained curve with largest exchange energy hence is plotted together with the pure Fe tip in figure 7.6. Due to the unknown absolute z -position of the experimental curve, it is shifted in z -direction with respect to the theoretical curve so that the regions coincide where E_{ex} starts to deviate significantly from zero.

7.2 Tip State Switching during Spectroscopy

As will be discussed in detail in chapter 8, the tips used within the MExFM studies are structurally unstable by a chance of 50%. Unstable tips are recognized easily, as an increase of dissipation is measured simultaneously on approach during imaging and spectroscopy. Moreover, some tips are able to switch magnetically without showing additional dissipation contrast in MExFM experiments. Performing 3D-MExFS with both types of unstable tips is experimentally possible, while the evaluation is not straightforward for structurally unstable tips.

7.2.1 Magnetically Unstable Tips

Figure 7.7 shows two $\Delta f(z)$ -curves obtained on one single Fe atom. While scanning the atom from right to left and back, the tip switches the direction of its magnetic moment several times, thus imaging the atom as either maximum or minimum, as shown in the corresponding $(400 \times 400) \text{ pm}^2$ MExFM zoom in the lower right. Magnetic switching of the tip apex in MExFM is presented and discussed in detail in chapter 8 (cf. figure 8.11). The tip shows no distance dependent dissipation as plotted in the lower part of figure 7.7. Such non-dissipative tips are classified as structurally stable, however, the tip is magnetically unstable. The spectroscopy curves are depicted right next to each other above maximum ($\Delta f_{\text{max}}(z)$: red) and minimum ($\Delta f_{\text{min}}(z)$: blue). The data has been acquired using the spectroscopy acquisition method (i). After correcting the z -scale by the corresponding topography value (corrugation of 6 pm), the magnetic exchange induced frequency shift (black) is extracted. The derived magnetic exchange energy $E_{\text{ex}}(z)$ is plotted in red in figure 7.4.

Though the tip switches magnetically, the derived exchange interaction is qualitatively and quantitatively the same as obtained with a stable tip. This indicates, that structurally the tip can be considered as Fe pyramid, but the magnetic orientation of the foremost atom (or the whole apex cluster) is able to flip by 180° without additional loss of energy. Thus, the tip apex can be considered as magnetically free standing cluster.

Theory shows that not only the front apex atom contributes to E_{ex} and that it is crucial to include relaxation effects, because otherwise even pure Fe tips would exhibit a sign change [102], which is experimentally not observed. As it will be discussed in chapter 8, small relaxation effects can already change the magnetic alignment in small magnetic clusters.

However, using a magnetically switching tip still allows to obtain smooth spectroscopy curves without additional loss of energy.

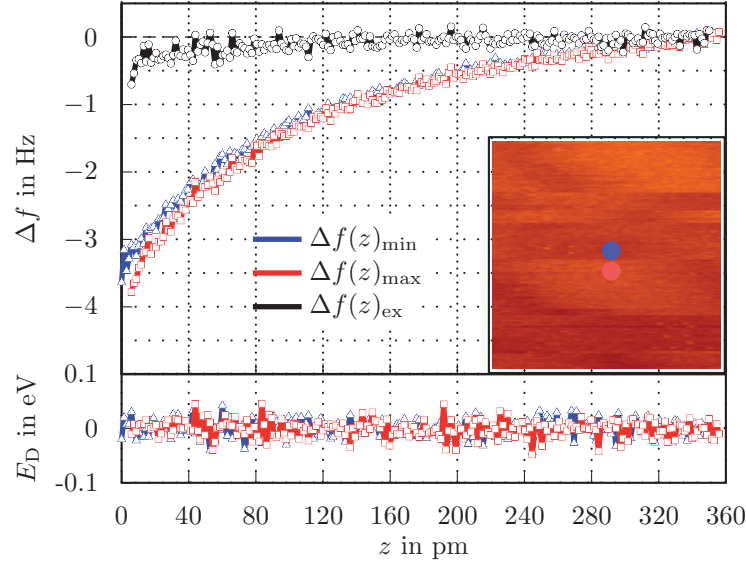


Figure 7.7: Two individual $\Delta f(z)$ -curves recorded with a non-dissipative but magnetically unstable tip on one single Fe atom, indicated in the according topography. Red and blue indicate the spectroscopy points. The tip images the atom as either maximum or minimum, respectively. The curves split smoothly into two branches at small tip-sample distance, allowing to obtain the black difference curve, which is a measure of the magnetic exchange interaction.

Parameters: $\Delta f_{\text{stab}} = -5.6$ Hz, $\Delta z = 1.46$ pm, $c_z = 145.5$ N/m, $A = 3.83$ nm, $f_0 = 187$ kHz, $B = 5$ T, $Q = 318000$.

7.2.2 Structurally Unstable Tips

Figure 7.8 shows two individual $\Delta f_{\text{ap}}(z)$ - and $\Delta f_{\text{p}}(z)$ -curves obtained on a maximum and minimum, respectively, using spectroscopy acquisition method (i) with an initially Cr coated tip. The atoms in the corresponding topography in the lower right of figure 7.8 appear distorted and the image exhibits a worse SNR than figures 7.2, 7.3 and 7.7. The curves do not deviate from each other in the distance regime between 20 pm and 90 pm, but at about 20 pm the curve obtained on the maximum shows a sudden steep decrease of the frequency shift. About 12 pm closer to the surface, the minimum curve shows a comparable sudden decrease. Moreover, the dissipation recorded simultaneously shows a strong increase at exactly the same vertical positions above the surface. The measured energy loss at closest tip-sample distance is on the order of $E_D = 3$ eV.

The points where the tip instabilities occur are indicated by arrows. Obviously, the dissipation is site specific and magnetically sensitive, that is, it is different on ap- and p-site. Thus, as soon as energy is dissipated, the tip apex is structurally different on ap- and p-site. A direct comparison and subtraction of both curves would only be possible in the regime, where all forces contributing to the frequency shift, conservative and non-conservative, are identical. This

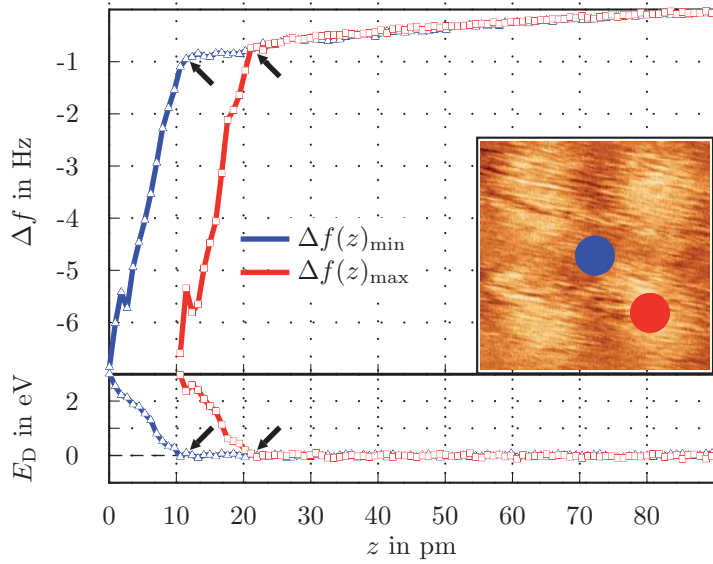


Figure 7.8: Two individual $\Delta f(z)$ -curves recorded with a dissipative (unstable) tip on Fe atoms with oppositely oriented magnetic moments, as indicated in the topography in red and blue on maximum and minimum, respectively. The curves exhibit a sudden step decrease at a certain tip-sample distance, separated by about 12 pm, that coincides with a sudden increase in dissipation. Arrows mark the points of tip instabilities. Structural instabilities and dissipation are site specific, hence, both curves cannot be easily subtracted from each other to obtain the exchange interaction induced frequency shift.

Parameters: $\Delta f_{\text{stab}} = -6.5$ Hz, $\Delta z = 0.88$ pm, $c_z = 151$ N/m, $A = 3.89$ nm, $f_0 = 190.5$ kHz, $B = 5$ T, $Q = 275190$.

is exactly the regime, where the curves do not deviate from each other. In consequence, the tip does not show any exchange interaction related contrast as long as its apex is structurally stable. With the onset of dissipation, the exchange interaction arises as well. Background to these phenomena is the hysteretic motion of apex atoms which is different on ap- and p-sites, as will be discussed in detail in chapter 8. However, the discussed results strongly indicate that structurally unstable tips are not regular pyramids, and that they do not allow for a quantitative measurement of exchange forces, because subtracting curves recorded on p- and ap-site, respectively, only reveals the pure magnetic exchange interaction, if the tips are structurally identical. Otherwise, non-magnetic contributions do not cancel out.

The successful direct measurement of the magnetic exchange interaction across a vacuum gap has been shown for the first time using 3D-MExFS. Whenever a stable spin-sensitive tip is used, acquisition and evaluation of the experimental data is straightforward and agrees very well with theoretical findings. Although the used tips were initially Cr coated, comparison with theory reveals that the tip apices finally became pure Fe clusters during a

standard tip modification prior to the spectroscopy experiment (cf. chapter 8). Such a direct access to the exchange interaction is of great importance, as magnetic exchange is fundamental to all magnetic ordering. Its precise knowledge can be utilized to tailor magnetism on the atomic scale, for instance, to switch the magnetic state of atoms, clusters or molecules in a controlled fashion by varying the tip-sample distance.

CHAPTER 8

TIP MODIFICATIONS

Achieving exchange contrast and hence spin sensitivity within an MExFM experiment is straightforward: whatever the real configuration at the tip apex is, if atomic resolution is obtained in the non-contact regime, one can at least infer that the tip apex is atomically sharp, which is one prerequisite. This prerequisite most often is not given straight from the beginning, but the tip end has to be modified to achieve the desired state.

Another prerequisite to achieve spin sensitivity is a magnetically sensitive tip end with stable spin. However, using a magnetically coated tip is no guarantee that the same tip is able to detect single magnetic moments as the moment of a magnetic cluster at the tip apex might rotate randomly (paramagnetically) on a much faster time scale than the data acquisition time, which is about 1 ms per data point. In the same way as for the achievement of atomic resolution, modifications of the tip apex at small tip-sample separation can be provoked to achieve spin sensitivity.

In 2006 CACIUC and co-workers [139] presented first-principles simulations for a Si(111)-type tip revealing a mechanism for the sharpening of an initially blunt tip via short-range chemical forces. This process is accompanied by an irreversible structural change of this type of tip at its foremost end. In 2007 HOFFMAN *et al.* [140] found that, using KBr terminated tips, (reversible) structural tip changes cannot only occur directly at the tip end, but slightly above the foremost tip atom as well. GHASEMI *et al.* [66] considered pure Si tips with the tip apex atoms forming covalent bonds. They found that the tip cluster is in a frustrated state, and that frustrated tip structures facilitate hysteretic atomic rearrangements of the tip atoms when tip and surface potential overlap. Amongst others [141, 142], these are just some recent examples discussing the possibility of tip apex modifications during FM-AFM experiments. Indeed, it is widely known to experimentalists that in non-contact FM-AFM the tip apex can change (even drastically) in an uncontrollable way, that is, surface material is picked up by the tip or tip material is deposited onto the surface or structural changes happen at the unstable tip end. Tip modifications can

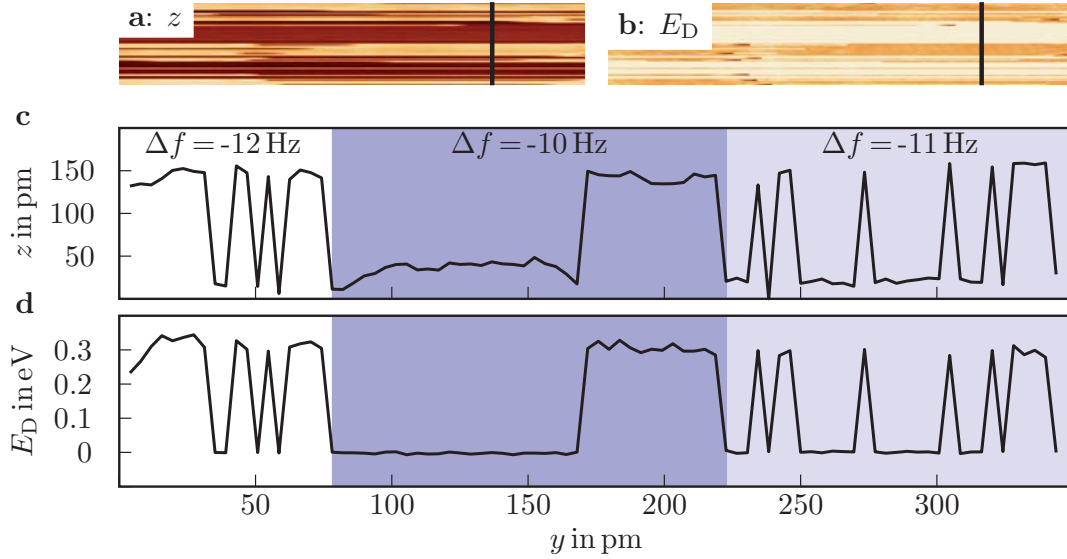


Figure 8.1: **a** (2×0.35) nm^2 topography image obtained using a Cr coated tip spontaneously changing between two states. **b** Energy dissipated per oscillation cycle with respect to the intrinsic dissipation obtained simultaneously to **a**. **c** and **d** Line section along the slow scan direction (vertical black lines) in **a** and **b** showing the z -value, which corresponds to the tip length, and the energy dissipated per oscillation cycle, E_D , respectively. At smaller tip-sample separation, that is, at more negative Δf , the switching rate increases.

Parameters: $c_z = 143.6 \text{ N/m}$, $A = 3 \text{ nm}$, $f_0 = 185.8 \text{ kHz}$, $Q = 77000$.

be provoked in experiments to achieve atomic resolution with spin sensitivity. However, some tips might become structurally and/or magnetically unstable, while others do not. Finally, numerous modifications lead to blunt tips and hence to limited cantilever lifetimes.

8.1 Dissipation of Energy

Whenever tip instabilities or tip changes occur due to hysteretic atomic rearrangements, they are detectable via the energy loss within single cantilever oscillation cycles: experimentally it is observed that changes in dissipation are often accompanied by changes in atomic scale contrast [17, 143, 144] and vice versa.

Figure 8.1 shows topography z and dissipation E_D recorded simultaneously. It further shows line sections of both channels along the slow scan direction y . While the amplitude stays constant throughout the image (not shown), sudden changes (bright and dark) in z and E_D are visible. The line sections are divided into three parts. While the first 20% of the topography are recorded at a stabilization frequency of $\Delta f = -12 \text{ Hz}$, the next almost 50% are recorded at $\Delta f = -10 \text{ Hz}$, and the last third is recorded at $\Delta f = -11 \text{ Hz}$. Each switching



Figure 8.2: **a** $(3 \times 1.4) \text{ nm}^2$ MExFM image obtained using a Cr coated tip. The left side of the image represents raw data, while the right is flattened for better visualization. The image shows slight changes in z , while the magnetic contrast remains unchanged. **b** Simultaneously recorded dissipation showing no measurable contrast. **c** Line section along the white dashed line in **a**. Structural tip changes are indicated by black arrows.

Parameters: $\Delta f = -6.1 \text{ Hz}$, $c_z = 145.5 \text{ N/m}$, $A = 3.83 \text{ nm}$, $f_0 = 197 \text{ kHz}$, $Q = 318000$.

between dark and bright as it can be seen in figure 8.1a is equivalent to a tip change and the tip-sample distance is increased (bright) or decreased (dark) when the tip gets longer (or the interaction force becomes stronger) or shorter (or the interaction force becomes weaker), respectively, as the feedback loop adjusts the tip-sample distance to keep the Δf_{stab} -value constant within the specified regions of constant frequency shift. The corresponding z -value is plotted in figure 8.1c.

From the data in **a** and **c** it is obvious, that the tip changes between two possible states separated by about 120 pm in z . The changes may be correlated to tip material, most probably a single atom¹, jumping from the side of the tip to its end (the tip gets longer) and back again (the tip gets shorter). Note that this process is structurally reversible. The switching rate further depends on the interaction strength, hence on the frequency shift setpoint value. While at $\Delta f = -12 \text{ Hz}$ the switching rate is $\approx 0.6 \text{ Hz}$, it decreases to $\approx 0.5 \text{ Hz}$ at $\Delta f = -11 \text{ Hz}$ and it nearly vanishes at $\Delta f = -10 \text{ Hz}$, where a switching rate of $\approx 0.1 \text{ Hz}$ is obtained and the lifetime of both states is about equal². The two tip states are also visible in the dissipation image in figure 8.1b and in the corresponding line section in figure 8.1d. While the tip is in its shorter state, the energy dissipated during a single oscillation cycle is set to $E_D = 0 \text{ eV}$. When the tip gets longer, the difference in energy dissipation is on the order of $E_D = 0.3 \text{ eV}$. Hence, in its longer state, the foremost tip apex atom is able to hysteretically relax towards the surface within every single cantilever oscillation cycle, possibly due to a low coordination at the tip end. The hysteretic motion leading to an additional loss of energy is different in the shorter tip state, where the foremost tip atom sensing the surface might have a higher coordination. Such tip changes and the onset of dissipation presented in figure

¹The covalent radius of a single Cr atom is about 140 pm [145], that of Fe is about 116 pm [146].

²The switching rate is calculated counting the single events and using the time of 0.7 s/line along the x -direction during scanning.

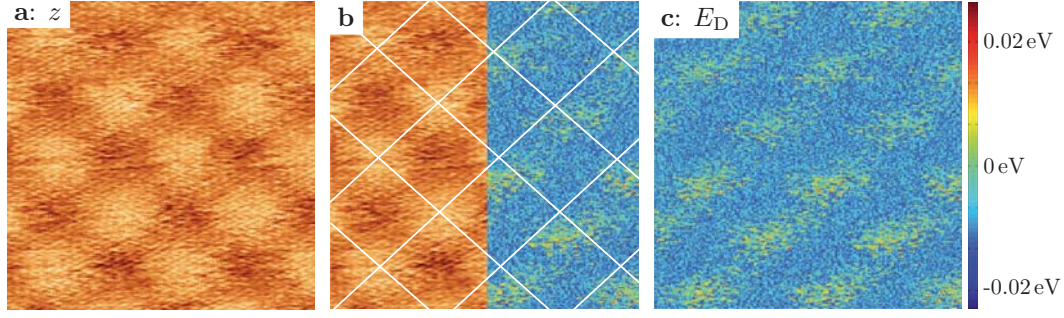


Figure 8.3: **a** $(1 \times 1) \text{ nm}^2$ atomic resolution obtained using an Fe coated tip. **c** Simultaneously recorded dissipation. Both data channels show the chemical surface unit cell. For comparison of the lattice structure phase shifted between topography and dissipation, **b** is tiled into topography on the left and dissipation on the right. Parameters: $\Delta f = -21 \text{ Hz}$, $c_z = 37 \text{ N/m}$, $A = 5 \text{ nm}$, $f_0 = 166.3 \text{ kHz}$, $Q = 144000$.

8.1 indicate that the foremost tip atom can be in an unstable configuration, and that its motion correlates with tip-sample interaction strength.

In contrast to changes in dissipation that can be correlated to changes in tip structure, figure 8.2 shows an MExFM image of the iron monolayer representing structural tip changes, but no change in the dissipation signal is measured. The image in **a** reveals the $c(2 \times 2)$ magnetic surface unit cell. While the right part of the image is flattened for a better visualization of the spin contrast, the left part represents raw data. Herein, a change from darker to brighter contrast and vice versa indicates that the tip changes structurally and that the interaction strength increases or decreases, respectively. The line section along the white dotted line is presented in figure 8.2c. Every arrow indicates a structural tip change, while the tip remains magnetically stable and spin-sensitive. The changes in z are between 10 and 20 pm, hence much smaller than presented in figure 8.1. However, the changes are not accompanied by additional energy dissipation. Since the contrast remains unchanged, a structural change above the tip apex atom may be likely, where an atom is eventually moving laterally and not vertically [140]. In any of the observed states, the foremost tip apex atom is not able to reversibly relax towards the surface as shown in figure 8.1. Hence, the different stable states of the tip apex atom indicate that up to a certain amount vertical movement of the foremost tip atom towards the surface is crucial to lead to dissipation of energy. On the other hand not only single atoms might flip, but the whole tip apex structure could be involved in the dissipation process, similar to the frustrated states reported for Si-tips [66].

8.1.1 Atomic Scale Dissipation Contrast

In [60] it has been observed by simulations using a virtual AFM set-up that apparent damping might increase due to tip-surface interactions, but this is mainly caused by the macroscopic van der Waals interaction, which does not

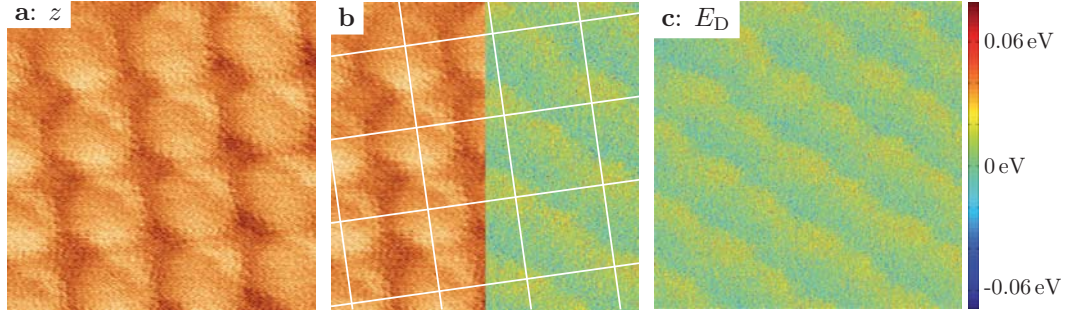


Figure 8.4: **a** $(1.5 \times 1.5) \text{ nm}^2$ MExFM image obtained using a Cr coated tip. **c** Simultaneously recorded dissipation. While the topography shows the magnetic surface unit cell, the dissipation shows the chemical surface unit cell. For comparison of the lattice structure phase shifted between topography and dissipation, **b** is tiled into topography on the left and dissipation on the right.

Parameters: $\Delta f = -7.6 \text{ Hz}$, $c_z = 145.3 \text{ N/m}$, $A = 3 \text{ nm}$, $f_0 = 186.8 \text{ kHz}$, $Q = 140000$.

contribute to the chemical contrast. Only when non-conservative interactions are included into the simulations, the contrast in atomic scale dissipation images shows large corrugation. This proves that an experimentally observed atomic-scale damping contrast occurs due to physical dissipative tip-surface interactions and is not necessarily an artefact of instrumentation, as soon as the dissipated energy is larger than $E_D = 1 \text{ meV}$.

The authors in [60] also find that topography and dissipation images may not necessarily show the same contrast pattern, as this depends, for instance, on the distance of closest approach, hence $\Delta f(z)$. Furthermore, they found that the lateral scanning velocity has little effect on topography and dissipation images, when dissipation occurs due to non-conservative tip-surface interactions. In figure 8.3a and c topography and dissipation, recorded simultaneously using an Fe coated tip, are shown. The topography reveals the chemical $p(1 \times 1)$ surface unit cell of the iron monolayer. The same contrast is visible in the dissipation, but figure 8.3b, tiled into topography on the left and dissipation on the right, shows that there is a slight shift of the atomic lattice between both channels. Possible explanations for the shift are tip changes, for example, due to instabilities of the positions of the tip apex atoms, that affect the spatial correlation between topography and dissipation image. A weakly bound foremost tip atom laterally and vertically moving along an asymmetric tip apex during the vertical approach of tip and sample is the most simple structure coming into mind to explain the observed contrast patterns [17]. If the motion of the atom is reversible and occurs at different tip-sample distances during approach and retract of single cantilever oscillation cycles, this motion is hysteretic and leads to dissipation of energy.

This example demonstrates the strong dependence of the dissipation contrast on structure and state of the tip apex.

8.1.2 Chemical and Exchange Interaction Induced Dissipation

Considering a structurally unstable tip apex, the system of tip apex and sample is moving between two or more minima on the potential energy landscape. Thus, any tip-sample interaction on the atomic scale is able to influence the dissipation contrast. As, for instance, the short-range chemical interaction is element specific, dissipation phenomena will in general be element specific as well. Eventually, the short-range magnetic exchange interaction contributes to atomic rearrangements when a magnetic tip-sample system is considered: the effect of the exchange interaction on the chemical bonds of single atoms has already been proven theoretically, cf. figure 6.3c. Even magnetic exchange between single atoms within the tip apex is able to change the energy landscape of atomic magnetic moments, when their chemical bonds are stressed or rearranged. Composition, magnitude and distance dependence of the interaction, however, strongly depend on the chemical and structural composition of the tip apex. Hence, considering a spin sensitive tip end showing relaxation effects whilst scanning the AF surface of Fe/W(001), E_D is expected to be site dependent.

Figures 8.4 and 8.5 show MExFM examples which reveal the $c(2 \times 2)$ magnetic surface unit cell of the monolayer, while in the dissipation channel the $p(1 \times 1)$ atomic contrast, phase shifted to the magnetic contrast, is visible. While the contrast in figure 8.4c appears to be a linewise contrast with slight atomic variation and only a slight shift with respect to the magnetic contrast, the contrast in figure 8.5 shows a clear chemical resolution with even higher dissipation. In both cases, the magnetic surface unit cell in the topography channel appears to be slightly distorted with a SNR worse than in figure 8.2a, that is, the atoms are not symmetric: in figure 8.4 the atoms appear with a half-moon shape superstructure, while the magnetic contrast in figure 8.5 even appears as zig-zag-structure.

One explanation for the dissipation contrast is an asymmetric tip apex with the spin sensitive part being non-dissipative, while a second part of the apex is magnetically non-sensitive but structurally unstable and hence dissipative. Both parts are laterally separated but contribute to the overall signal. Hence, the dissipation occurs only due to chemical interaction, not due to magnetic exchange.

Another, more complex tip structure might also lead to the observed contrast in dissipation and topography: as the dissipation is not spin sensitive, the foremost tip atom might be considered as unstable and flips its magnetic orientation on every single Fe atom due to changes of its chemical bond length. Hence, it is able to orient parallel to the surface spins and magnetic contrast appears only due to the interaction of the tip base with the surface spins (cf. chapter 6.1), which does not contribute to any non-conservative interaction.

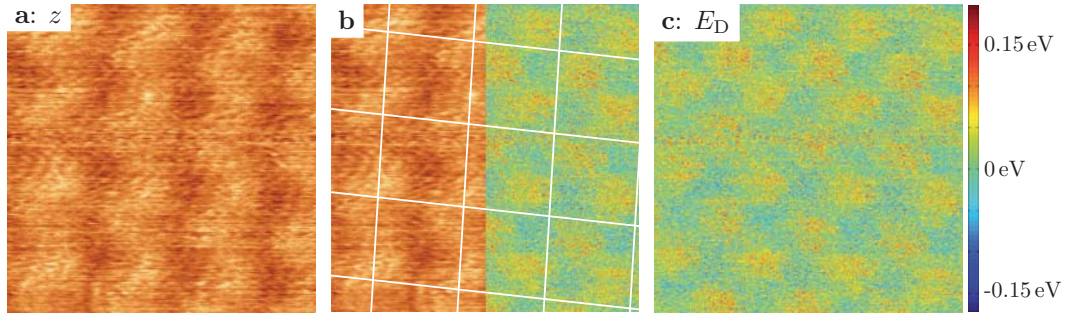


Figure 8.5: **a** $(1.5 \times 1.5) \text{ nm}^2$ MExFM image obtained using a Cr coated tip. **c** Simultaneously recorded dissipation. While the topography shows the magnetic surface unit cell, the dissipation shows the chemical surface unit cell. For comparison of the lattice structure phase shifted between topography and dissipation, **b** is tiled into topography on the left and dissipation on the right.

Parameters: $\Delta f = -22 \text{ Hz}$, $c_z = 152.2 \text{ N/m}$, $A = 3 \text{ nm}$, $f_0 = 191.3 \text{ kHz}$, $Q = 42561$.

A slightly asymmetric tip base might furthermore lead to the superstructure in the atoms or the zig-zag-structure shown.

Figure 8.6 presents an example of a magnetic contrast showing up in topography and dissipation simultaneously. Both contrasts are shifted with respect to each other, as indicated in figure 8.6b, and, again, the atoms are certainly not symmetric, but show triangular shape in topography and rectangular shape in dissipation. Here, the dissipation is spin sensitive as well, and the short-range magnetic exchange interaction contributes to atomic rearrangements at the tip apex. Moreover, the asymmetry again indicates a structurally highly asymmetric tip apex. The different shapes of the atoms in topography and dissipation, respectively, within the presented figures 8.4, 8.5, and 8.6 might be explained by an asymmetry in lateral stiffness of the tip apices. In the case of a highly asymmetric tip the relaxation of unstable atom positions is strong on the side of an atom and weaker, when the tip is positioned on top or on the other side of the atom.

8.1.3 Tip Classification

On the first approach it is not clear with unambiguity, whether true atomic scale dissipation is induced by instabilities of tip or of sample atoms. As previously discussed [147], the absence of dissipation features when using different tips on the same surface suggests that the as presented dissipation data are induced by non-conservative interactions due to structural and magnetic relaxation of tip apex atoms.

The experiments performed with respect to magnetic exchange allow for a classification of the different tip apices using the as presented survey on dissipation and atom shape: from 24 successful MExFM experiments on Fe/W(001) using either Fe or Cr coated tips, eleven tips showed up with a topographic

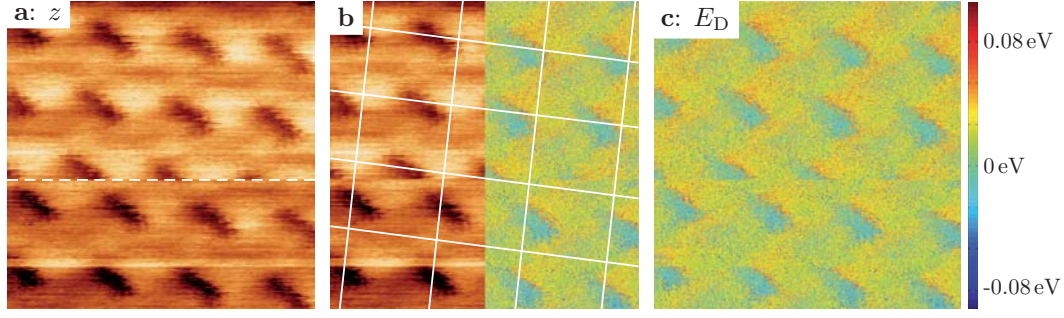


Figure 8.6: **a** $(1.5 \times 1.5) \text{ nm}^2$ MExFM image obtained using a Cr coated tip. **c** Simultaneously recorded dissipation. Both data channels show the magnetic surface unit cell. For comparison of the lattice structure phase shifted between topography and dissipation, **b** is tiled into topography on the left and dissipation on the right. Atom shape and dissipation indicate a highly asymmetric tip apex. Parameters: $\Delta f = -5 \text{ Hz}$, $c_z = 145.3 \text{ N/m}$, $A = 3 \text{ nm}$, $f_0 = 186.8 \text{ kHz}$, $Q = 140000$.

contrast comparable to figure 8.2a. Here, the atoms are of circular shape. Furthermore, the SNR is much better compared to the other 13 tips, showing a topographic contrast comparable to figure 8.5a, where the atoms appear distorted with a much worse SNR. Moreover, all tips revealing circular shaped atoms while being spin sensitive did not show any dissipation (non-dissipative tips), different to the thirteen tips showing distorted atoms while being spin sensitive (dissipative tips).

Thus, the non-dissipative tips are classified as stable, while dissipative tips are unstable. In comparison with the spectroscopic data presented in chapter 7, non-dissipative tips show only a variation in $\Delta f(z)$ on approach of tip and sample, while dissipative tips show a variation not only in $\Delta f(z)$, but also in $E_D(z)$.

As indicated in the beginning of this chapter, the used tips have to be modified to achieve atomic resolution with spin-sensitivity. However, the modifications often create unstable tips. To clarify the processes at the tip end during a tip modification, different types of modifications are discussed in the following.

8.2 Spontaneous Tip Modifications

Models exist [148], where a hard tip alters a soft surface, that is, one or more surface atoms are pulled away from the surface on retraction of the tip resulting in a tip change. The fundamental ideas can be applied vice versa: a hard surface alters the atomic structure of an approaching tip, that is, tip apex atoms might jump to the surface. Both effects result in an irreversible tip change.

Whether or not the tip-sample system will return to its original state on retraction of a single oscillation cycle is found to depend on temperature and

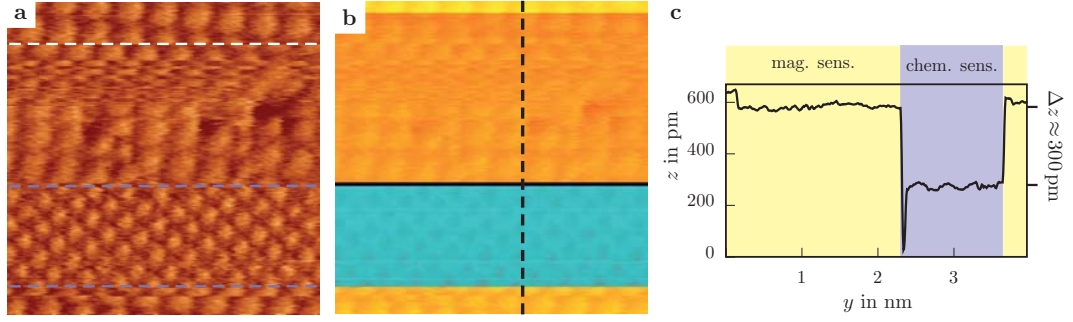


Figure 8.7: **a** $(4 \times 4) \text{ nm}^2$ topography obtained using a Cr coated tip spontaneously changing between chemical and magnetic sensitivity. **b** Raw data of the flattened image in **a**. **c** Averaged line section along the slow scan direction.

Parameters: $\Delta f = -19 \text{ Hz}$, $c_z = 150 \text{ N/m}$, $A = 3.49 \text{ nm}$, $f_0 = 190 \text{ kHz}$, $B = 0 \text{ T}$.

tip velocity [148], as both have a strong influence on the energy barrier crossing within the model of adhesion hysteresis. Obviously, low temperatures and a high tip velocity as in the present experiments might lead to irreversible tip changes, when the adhering atoms are not able to reconfigure to a more stable position at the tip end, but stay on the surface or vice versa. This leads to spontaneous and irreversible structural and even magnetic tip changes at close tip-sample distances.

8.2.1 Structural Changes

Structural modifications of the tip state are recognized by abrupt changes in topography, that is, in the atomic scale contrast by a change in corrugation amplitude or by achieving or loosing atomic sensitivity. The same accounts for the gain or loss of magnetic sensitivity. Figure 8.7a shows a $(4 \times 4) \text{ nm}^2$ surface area of the Fe monolayer obtained using a Cr coated tip. The surface is resolved with the contrast changing between chemical and magnetic sensitivity. Chemically identical iron atoms within the $p(1 \times 1)$ surface unit cell appear smaller in size than within the magnetic $c(2 \times 2)$ arrangement when obtained with a magnetic sensitive tip. The changes in contrast can be directly related to spontaneous modifications of the tip state, they occur without changing any external parameters. While in figure 8.7a the image has been flattened to visualize both contrasts, **b** represents color coded raw data. Turquoise areas therein are apparently less high than orange areas. A change from orange to turquoise and vice versa in figure 8.7b corresponds to a change in z . These changes are again equivalent to a change of tip length or tip-surface interaction strength: the z -scanner approaches tip and surface on a shortening of the tip or when the interaction strength is decreased, hence the topography appears depressed (turquoise), while it retracts tip and surface, when the tip gets longer or when the interaction strength is increased, hence the topography appears

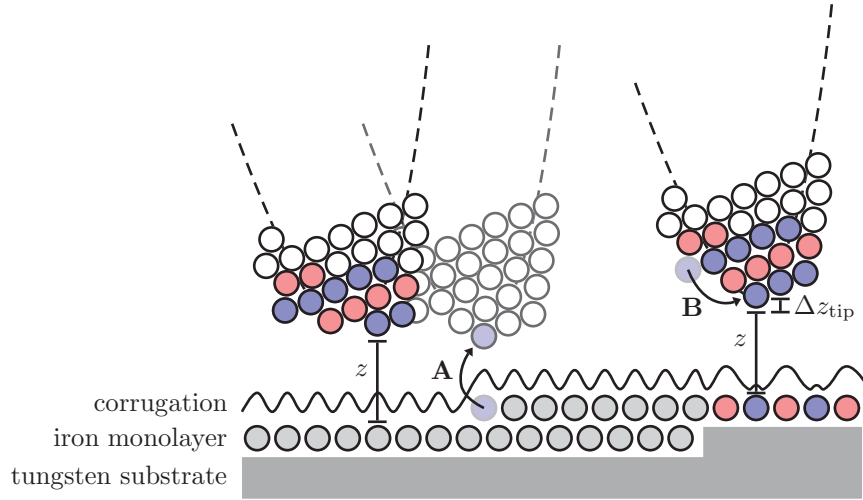


Figure 8.8: Sketch of two possible irreversible processes leading to structural modifications at the tip end. The initial Cr coated tip is non-magnetic. By increasing the tip-sample interaction a sample atom or cluster is picked up, cf. event A. Instead of picking up an atom or cluster, a modification within the apex may take place, cf. event B. After any of the modifications the tip is closer to the surface by Δz_{tip} . Though the composition of the apex might have changed, a magnetically sensitive tip is assumed in the end, thus revealing the AF structure of the Fe monolayer.

elevated (orange). Confering to figure 8.7c (averaged line section along the slow scan direction in **b**), every change in z corresponds to a change of the tip state from chemical to magnetic sensitivity and back. When z gets larger by ≈ 300 pm, the tip simultaneously becomes magnetically sensitive, while it loses its magnetic sensitivity when it gets shorter.

As the tip lengthens (or the tip-surface interaction strength increases), when it gets magnetically sensitive, it either picks up atoms from the surface (e.g., one or several Fe atoms or adsorbates), or material from the tip, that is, one or several Cr atoms or adsorbates move from the side of the tip to its end.

Two possible processes taking place during a tip modification are sketched within figure 8.8. Initially, the foremost tip apex atoms, for example, AF Cr, are in an unknown magnetic state and the surface is scanned with chemical resolution. As soon as the tip-sample-interaction becomes stronger, either material from the surface is picked up, event **A**, or tip material from the apex side is transported to the apex end, event **B**. Within any of the two events, the magnetic ground state of the apex is supposed to be altered, as along with the structural modifications the local anisotropy of the AF or paramagnetic cluster at the apex is altered as well. After the modification the foremost tip apex atom is able to sense the exchange interaction and magnetic contrast appears. Moreover, the tip-sample distance in figure 8.8 is finally changed by Δz_{tip} , according to figure 8.7.

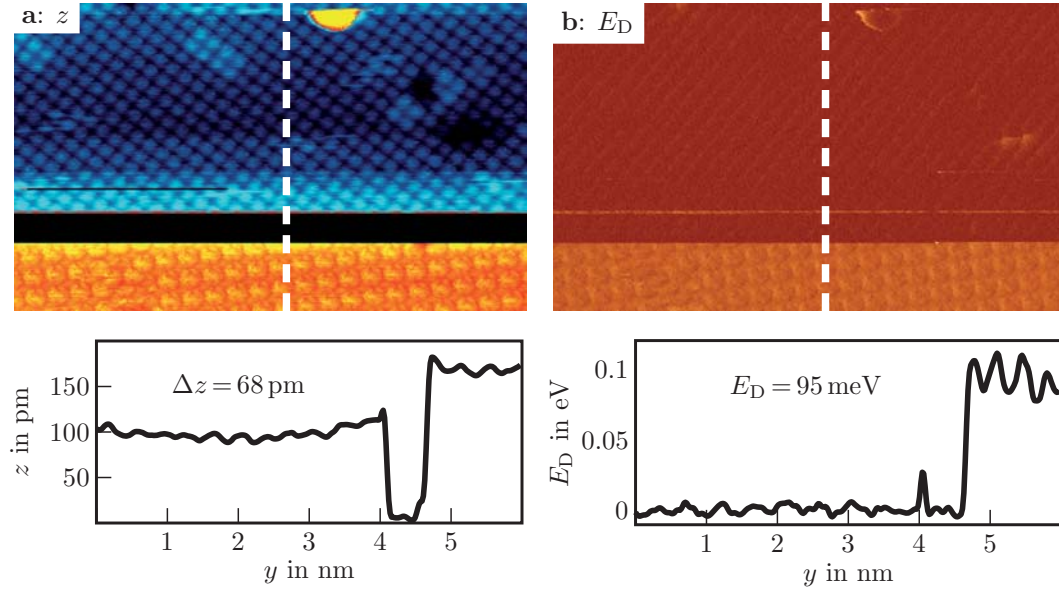


Figure 8.9: **a** $(10 \times 6) \text{ nm}^2$ MExFM image showing a spontaneous tip change during scanning in close proximity to the surface. Due to the modification the tip-sample distance is increased by 68 pm. Simultaneously, the tip state changes from chemically to magnetically sensitive. Along with the structural change, the dissipation increases by 95 meV as shown in **b**.

Parameters: $\Delta f = -9.8 \text{ Hz}$, $c_z = 150 \text{ N/m}$, $A = 3 \text{ nm}$, $f_0 = 190 \text{ kHz}$, $B = 5 \text{ T}$, $Q = 202797$.

Along with the change to a magnetic sensitive tip an increase of the dissipation is additionally observed as presented in figure 8.9. Actually, such an increase (decrease) in dissipation always occurs, whenever the tip changes from chemically to magnetically sensitive (or vice versa). Figure 8.9a shows a $(10 \times 6) \text{ nm}^2$ surface area scanned utilizing a Cr coated tip. A change from chemical to magnetic sensitivity is observed with the tip being elongated by $\Delta z = 68 \text{ pm}$. The simultaneously recorded dissipation in **b** shows an increase of E_D on the order of 95 meV. However, as the atoms in topography and dissipation are of the same shape and no lateral shift of the atomic lattice exists between both channels, apparent damping due to crosstalk cannot be excluded.

8.2.2 Magnetic Changes

During scanning in MExFM using unstable tips, the direction of the magnetic moment at the tip end is able to switch even without a structural modification: a shift of the magnetic contrast by half the lattice constant, that is, an inversion of the contrast, indicates that the tip state switched into a state with its moment rotated by 180° , now imaging the Fe atoms with opposite magnetic moment as protrusions, while protruding atoms are always antiparallel to the tip magnetic moment according to theory (cf. chapter 6.1). Such changes of the

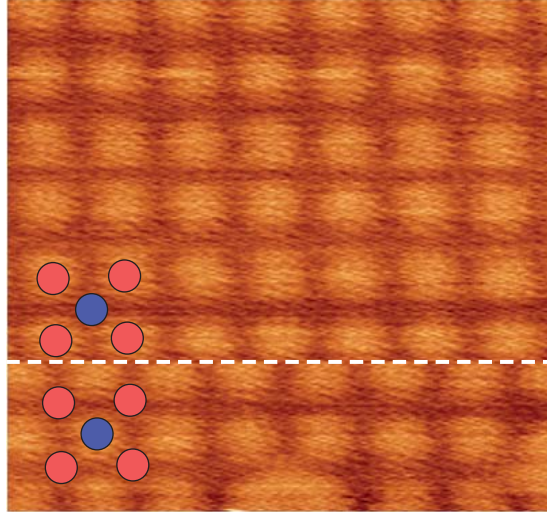


Figure 8.10: $(2 \times 1.8) \text{ nm}^2$ MExFM image obtained using an Fe coated tip. Along the white line the tip magnetic moment rotates spontaneously by 180° and the contrast appears inverted.

Parameters: $\Delta f = -14.8 \text{ Hz}$, $c_z = 32.5 \text{ N/m}$, $A = 5 \text{ nm}$, $f_0 = 156 \text{ kHz}$, $B = 5 \text{ T}$.

magnetization direction can be easily identified during scanning in MExFM, as shown in figures 8.10 and 8.15b. The shift of the contrast is visible along the white lines in the latter two images. The surface magnetic unit cell in figures 8.10 and 8.15b is sketched using red and blue circles. Below the white line the tip senses the former p-site as protrusion while the contrast pattern itself does not change and nicely corresponds to figure 6.5d. The figures represent raw data. Thus, a change of tip length can be excluded. Furthermore, a structural jump of the foremost tip atom from one binding site to another along the tip apex without changing the tip length, which might also lead to a shift of the contrast, can be excluded from figure 8.15b, where an adsorbate is imaged simultaneously. If a foremost tip apex atom would change its binding site along the apex, the adsorbate would be shifted in position as well, but it is not. Moreover, the jump of a tip apex atom to a new binding site along the apex should lead to an abrupt change in dissipation [140], which is absent, for instance, in figure 7.8b. Note that, although the contrast is shifted, these shifts do not correspond to an AF domain wall of the Fe monolayer. Such domain walls exist, but they include several atoms [119].

As it is energetically implausible that a mesoscopic tip switches its magnetic orientation, the switching must occur within the nanotip. Because thin film tips and not bulk tips are used, the magnetic coupling between the sharp tip apex region and the broad tip base might be rather weak, supporting the switching of a single cluster at the apex, weakly coupled to the bulk magnetic material. This situation is sketched in a very simple picture in figure 8.14, where the apex is considered as AF Cr. Note that the apex might also be an

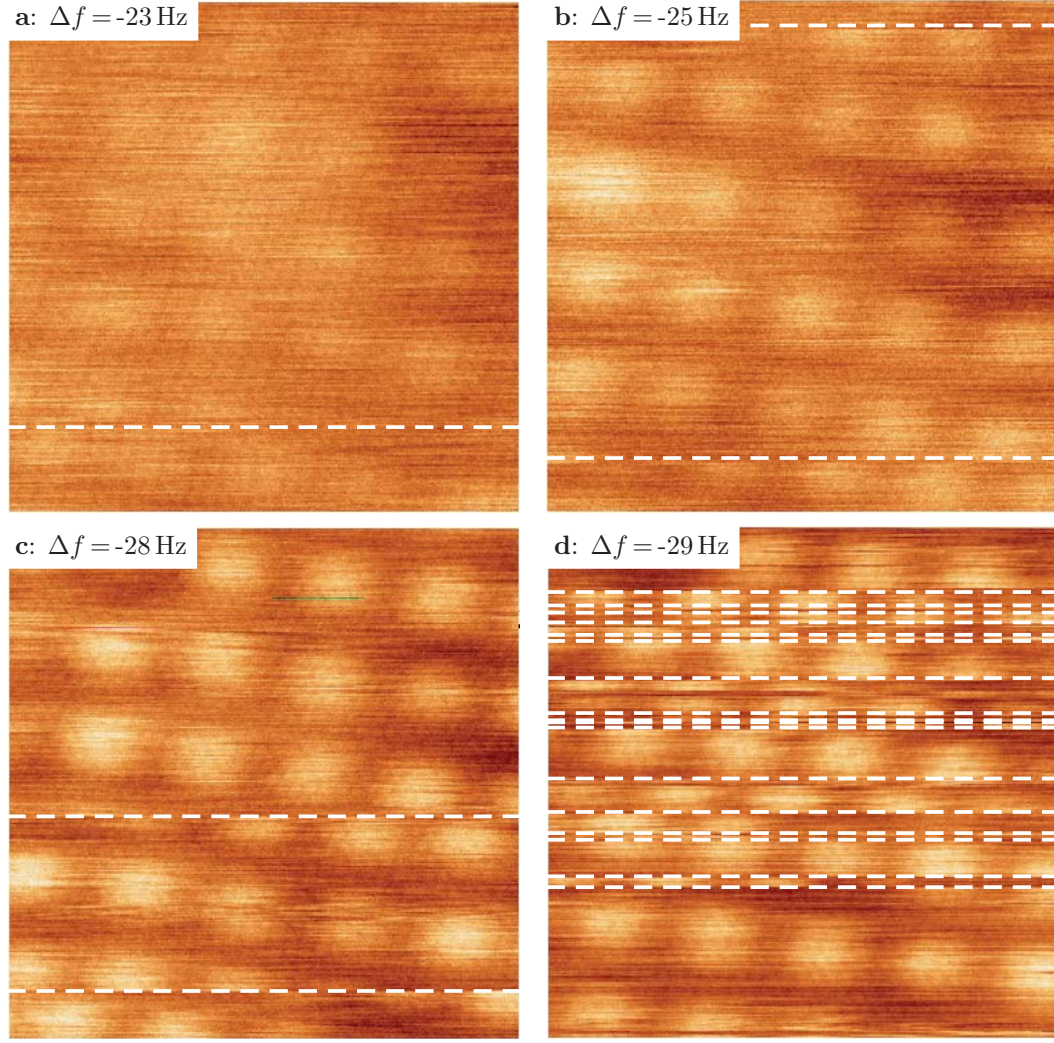


Figure 8.11: **a-d** Consecutive $(2 \times 2) \text{ nm}^2$ MExFM images obtained using a Cr coated tip with decreasing tip-sample distance, starting from $\Delta f = -23 \text{ Hz}$ in **a** to $\Delta f = -29 \text{ Hz}$ in **d**. Every white line corresponds to a tip magnetic moment switching by 180° ; the number of switching events increases with increasing tip-sample interaction strength.

Parameters: **a-d** $c_z = 143 \text{ N/m}$, $A = 2.81 \text{ nm}$, $f_0 = 185 \text{ kHz}$, $B = 4.5 \text{ T}$.

Fe cluster, which is easily switchable due to a strong exchange interaction. Of course, larger amounts of magnetic material could be deposited onto the tip to achieve a more bulk-like situation and magnetically more stable tips, but this would lead to blunter tip apices, which in turn are less suitable for atomic resolution imaging.

However, a weak coupling between apex and base combined with the relaxation of the tip apex atom towards the sample in close proximity, as shown by theory (cf. figure 6.3c), enhances the role of the magnetic exchange interaction

(either within the apex or mediated by the sample) on the anisotropy energy of the magnetic moment of the foremost tip atoms and hence on their orientation. Thus, the rate of magnetic switching should depend on the strength of the interaction, that is, on tip-sample distance. Besides the interaction strength, variation of temperature and tip velocity also allow for a decrease or increase of the energy barrier and should be considered. In figure 8.11a-d four consecutive MExFM images are obtained using an initially Cr coated tip in a magnetic field of 4.5 T. The tip-sample distance is decreased from image to image, starting at $\Delta f = -23$ Hz in **a** and ending at $\Delta f = -29$ Hz in **d**. The tip-sample interaction strength increases, respectively. Every white dashed line within the images corresponds to a switch of the tip magnetic moment by 180° . With increasing tip-sample interaction strength the number of switching events increases as well. While there is only one event at $\Delta f = -23$ Hz, 17 events are counted at $\Delta f = -29$ Hz. However, the number of switching events does not increase linearly with increasing tip-sample interaction and two events are counted at $\Delta f = -25$ Hz and $\Delta f = -28$ Hz. The tip-sample exchange interaction strength is estimated to be on the order of 5 to 10 meV, according to figure 7.6, within all images, but it is smallest at $\Delta f = -23$ Hz and largest at $\Delta f = -29$ Hz. The variation of the interaction strength from $\Delta f = -23$ Hz to $\Delta f = -29$ Hz, however, is small, as the contrast appearance is identical in all four images (cf. figure 6.5), but it is obviously large enough to lower the energy barrier E_b between the two magnetic tip states significantly on approach. The mean lifetime $\bar{\tau}$ of the two tip states with respect to the frequency shift is plotted in figure 8.12 for $\Delta f = -23$ Hz, -25 Hz, -28 Hz and -29 Hz, respectively. Up to three images for every frequency shift setpoint are evaluated therein. While $\bar{\tau} = 33.7$ s at $\Delta f_{\text{set}} = -29$ Hz, it increases to $\bar{\tau} = 348.2$ s at $\Delta f_{\text{set}} = -23$ Hz.

Considering the foremost tip apex as free standing magnetic cluster switching its magnetization direction, the NÉEL [149] and BROWN [150] model of thermal switching of the magnetization of a single domain particle might be applied. NÉEL and BROWN both state that in zero external field a single-domain particle has two equivalent ground states of opposite magnetization separated by an energy barrier E_B . Thermal energy could overcome the energy barrier, leading to superparamagnetic behaviour of the particle. An external field, however causes the two stable positions to have different energies. According to the Néel-Brown law, the mean lifetime $\bar{\tau}$ of the magnetic particle switching between the two states, up and down, respectively, can be written as

$$\bar{\tau} = \frac{1}{\nu_0} \cdot \exp \left[-\frac{E_b}{k_B T} \right], \quad (8.1)$$

with ν_0 being the attempt frequency. If an external field is applied, the energy barrier E_B is lowered and one of the two states should be favoured. Statistical analysis of the switching events in zero field, figure 8.13a, and in a flux density of 4.5 T, figure 8.13b, where the two directions of the tip magnetic moment

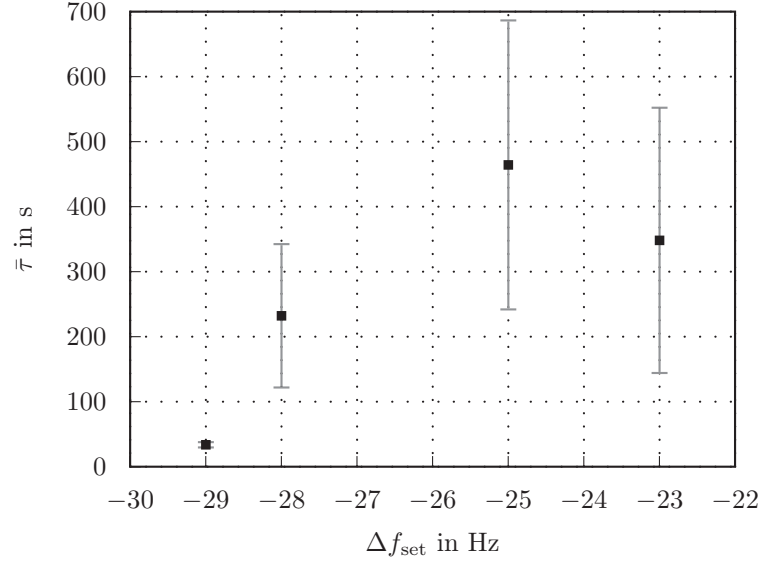


Figure 8.12: Mean lifetime $\bar{\tau}$ of the tip state as function of frequency shift. A more negative Δf_{set} indicates a smaller tip-sample distance, but the exact relation is unknown and non-linear.

are considered as state $\langle 0 \rangle$ and state $\langle 1 \rangle$, respectively, shows that the lifetime of both states as obtained in zero field is nearly equally distributed, that is, the probability of the tip magnetic moment to stay in state $\langle 1 \rangle$ corresponds to $61 \pm 9\%$. Considering the thermal energy of $k_B T = 0.69 \text{ meV}$ at 8 K and the mean lifetime of $\bar{\tau} = 23.85 \text{ s}$ (27 events are counted during 644 s of scanning time), the energy barrier can be calculated. It can be assumed that the switching most probably occurs at smallest tip-sample distance, which is a 190435 times per second, according to the resonance frequency. Hence, assuming $\nu_0 = f_0$ and applying the Néel-Brown law results in an energy barrier of $E_B = 4.6 \text{ meV}$. This is very well on the order of the MAE of single adatoms and adatom clusters on metallic surfaces [151–157]. For example, CABRIA *et al.* calculated the MAE for a Cr adatom on Ag(001) to be on the order of 5 meV. However, within small clusters, the MAE is even lower. Considering a cluster of four Fe atoms on Ag(001), the MAE is on the order of 0.12 meV/atom. Though comparison of the tip apex, that can be assumed as a single atom residing on a base of several atoms, with the theoretical models considered in the literature to calculate the MAE seems realistic, a direct comparison with the presented results, as well as a rough estimate of atoms involved in the switching at the tip apex is not possible.

Applying an external field perpendicular to the sample, the probability of the tip magnetic moment to stay in state $\langle 1 \rangle$ drastically decreases to $27 \pm 7\%$, hence state $\langle 0 \rangle$ is energetically more favourable: in state $\langle 0 \rangle$ the magnetic moment of the foremost tip atom should be aligned collinear with the field. The shift of the switching probability between zero flux density and 4.5 T

is sketched within the energy landscape of both states in figure 8.13. The change of the energy barrier E_b should correlate with the Zeeman energy at 4.5 T, which is about $E_Z = 1.27$ meV in the case of a single Fe atom and $E_Z = 1.5$ meV for a single Cr atom within the FM Cr(001) surface, but only $E_Z(4.5 \text{ T}) = 0.34$ meV within bulk Cr. This results in $E_b - E_Z$ for $\langle 1 \rangle$ and $E_b + E_Z$ for state $\langle 0 \rangle$. Determination of the mean lifetime of state $\langle 0 \rangle$ and $\langle 1 \rangle$ from figure 8.13b results in $\bar{\tau} = 57.6$ s and $\bar{\tau} = 22.3$ s, respectively. Again assuming an attempt frequency on the order of f_0 and considering the thermal energy of 0.69 meV results in an energy barrier of $E_b = 4.85$ meV for state $\langle 0 \rangle$ and $E_b = 4.56$ meV for state $\langle 1 \rangle$. Hence, the energy barrier without Zeeman contribution can be estimated to $(4.85 \text{ meV} + 4.56 \text{ meV})/2 = 4.7$ meV. This value is consistent with the already derived value of $E_b = 4.6$ meV. The additional energy contribution due to the Zeeman energy hence is about $4.85 \text{ meV} - 4.56 \text{ meV} = 0.29$ meV, a value comparable to the Zeeman energy of a bulk Cr atom.

However, the slope of $\log \tau(\Delta f)$ in figure 8.12 is not linear as expected following eq. 8.1. This inconsistency with the simple Néel-Brown model can be attributed to a wrong interpretation of the x -axes, where Δf is plotted instead of temperature or even energy. Δf does not scale linearly with energy. A translation of single Δf values into energy is not possible, as absolute z -values corresponding to each Δf -setpoint were not recorded during the measurements. Moreover, a complex structure of the tip apex cluster, an existing influence of the tip base on the magnetism of the tip end, the non-linear influence of the exchange energy on the energy barrier, and other anisotropy effects have to be considered as well. Additionally, only about 60 switching events are evaluated in maximum at $\Delta f(z) = -29$ Hz. Such a bad statistics might not allow for the determination of E_b and the attempt frequency of the switching ν_0 . Only a number of at least a thousand events would lead to a good statistics [158].

A true quantitative comparison of the data obtained in zero field and at 4.5 T is also not possible, as the data are acquired using different tips, and different tip geometries have to be taken into account. These might lead to different results. Additionally, according to chapter 8.1.3, the tip end in figure 8.13a is structurally more unstable than the tip end in figures 8.11 and 8.13b. Hence, relaxation effects and the role of non-conservative interactions on the anisotropy energy have to be considered differently. A determination of E_b would only be possible if exactly the same, stable tip would be used for a field or temperature dependent determination of the switching rate, if the total interaction energy between tip and sample is determined simultaneously, and if a few thousand events are recorded.

Assuming identical tips within the experiments presented in figure 8.13a and b, the energy barrier between 0 T and 4.5 T is shifted by roughly 50% when applying the field, according to the shift in lifetime from 50% to 25%. Hence, by further assuming a Zeeman energy of 1.27 meV for a single Fe atom

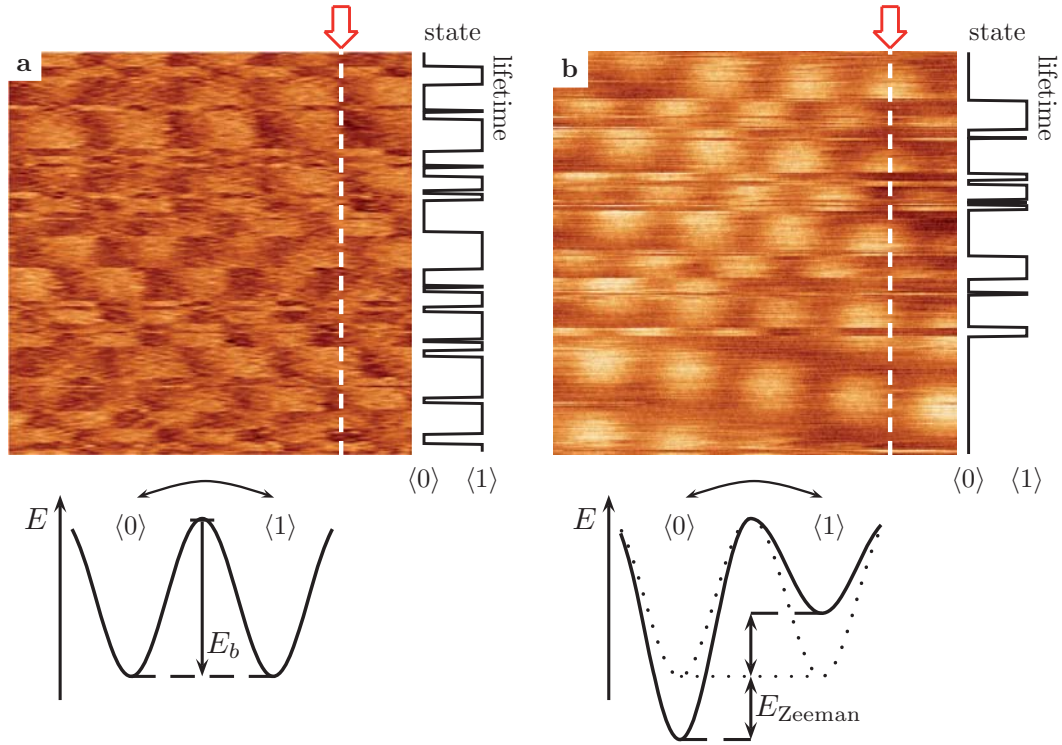


Figure 8.13: $(2 \times 2) \text{ nm}^2$ MExFM images obtained with two different tips with a switching magnetic moment at the tip end. The lifetimes of state $\langle 0 \rangle$ and state $\langle 1 \rangle$ are evaluated by the averaged line sections along the slow scan direction. **a** is recorded in zero flux density, **b** at 4.5 T. The change of the energy landscape by lowering the energy barrier E_b due to the onset of the Zeeman energy, hence favoring state $\langle 0 \rangle$, is sketched below: at 0 T the probability for the tip to stay in state $\langle 1 \rangle$ is $61 \pm 9\%$, at 4.5 T the probability for state $\langle 1 \rangle$ is decreased to $27 \pm 7\%$.

Parameters: **a** $\Delta f = -18 \text{ Hz}$, $c_z = 150 \text{ N/m}$, $A = 3.49 \text{ nm}$, $f_0 = 190 \text{ kHz}$, $B = 0 \text{ T}$.

b $\Delta f = -29 \text{ Hz}$, $c_z = 143 \text{ N/m}$, $A = 2.81 \text{ nm}$, $f_0 = 185 \text{ kHz}$, $B = 4.5 \text{ T}$.

at the tip end, the anisotropy energy in zero field would be on the order of $2.5 \text{ meV} = 100\%$. The barrier height scales with the amount of atoms within the tip apex cluster. Considering the thermal energy of 0.69 meV at 8 K this energy is not sufficient anymore to cross the barrier. However, the energy between tip and sample at the distance where magnetic exchange forces are measured is on the order of 5 to 10 meV and hence large enough to switch the magnetization direction of at least single atoms at the tip apex. This qualitative discussion shows that the tip apex might be considered independently of the tip base as single magnetic particle or cluster.

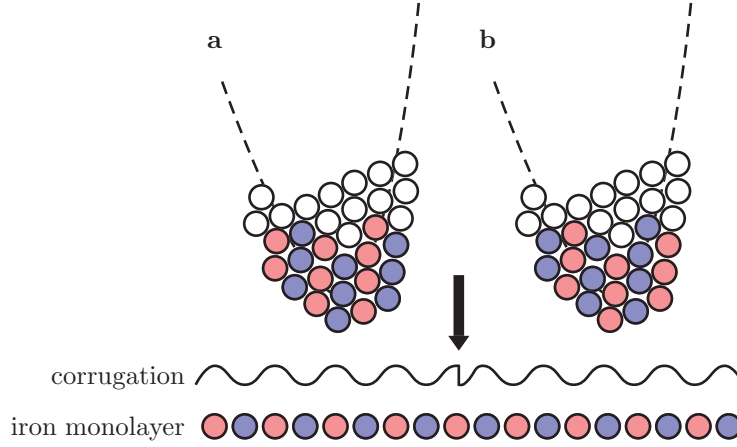


Figure 8.14: A sharp line of contrast inversion within an MExFM image can be explained by a simple model. **a** A magnetically sensitive tip apex (here AF Cr) scans the surface in close distance. **b** Due to strong magnetic exchange interaction with the sample the orientation of the magnetic moment of the cluster at the tip apex (or of a single atom, not sketched) might rotate by 180° . The obtained contrast changes abruptly, indicated by the black arrow.

8.3 Intended Tip Modifications

To deliberately induce modifications at the tip end, the tip-sample distance has to be decreased to increase the tip-sample interaction strength. However, upon approaching tip and surface very close into the regime where the slope of Δf changes its sign (cf. figure 3.8), the topography-regulator starts to regulate into the wrong direction. Whenever this happens, a tip crash is inevitable.

8.3.1 Spectroscopic Method

A more controllable way to induce tip modifications is performing $\Delta f(z)$ -spectroscopy, where the tip is approached very close to the surface above a specific point without using the z -feedback, hence a tip crash caused by the feedback regulator is avoided.

Figure 8.15a shows an atomic resolution image of the iron monolayer obtained with a Cr coated tip. While the tip is not magnetically sensitive, it is deliberately approached close to the surface utilizing force spectroscopy. The spectroscopy point is located in the upper right corner of figure 8.15a. During the $\Delta f(z)$ -curve at a stabilization frequency of $\Delta f_{\text{stab}} = -25$ Hz, the dissipation E_D rose from 0 meV at the relative starting point of $z_{\text{start}} = 0$ nm to a maximum value of $E_D = 6.8$ eV at $z = 0.96$ nm, 8.15f and close-up in 8.15g. At the point of closest approach ($z_{\text{end}} = 1$ nm), the dissipation showed a value of 4.3 eV, figure 8.15f. However, the oscillation is recovered with an amplitude deviation of $\Delta A = 60$ pm in maximum, which is only 2% of the amplitude value

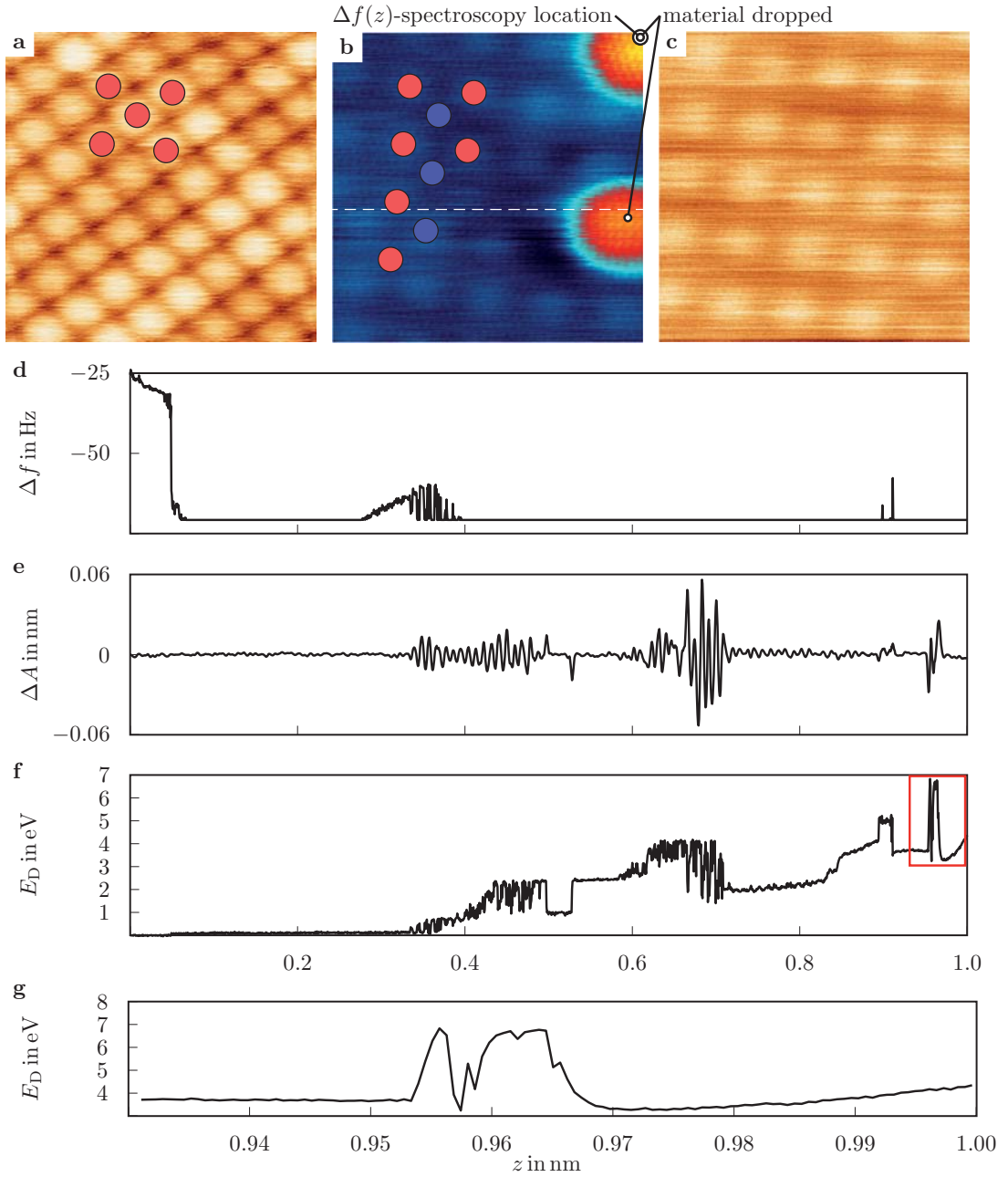


Figure 8.15: Using $\Delta f(z)$ -spectroscopy (the corresponding $\Delta f(z)$ -, $\Delta A(z)$ - and $E_D(z)$ -data are plotted in **d**, **e**, and **f**, respectively, **g** shows a close-up of **f**), a chemically sensitive tip in **a** is changed to a magnetically sensitive one in **b**. **c** The tip state stayed stable after moving to a different area. Along the white line in **b** the magnetic contrast is shifted by one lattice site.

Parameters: $(2 \times 2) \text{ nm}^2$, $\Delta f = -17 \text{ Hz}$ in **a**, $\Delta f = -25 \text{ Hz}$ in **b** and **c**, $c_z = 143 \text{ N/m}$, $A = 2.81 \text{ nm}$, $f_0 = 185 \text{ kHz}$, $B = 4.5 \text{ T}$, $Q = 62835$.

of 2.81 nm, figure 8.15e, but which is a significant distance change when the tip is close to the surface. The frequency shift during the approach is recorded as well, but it exceeds the actual PLL range limit of -76.3 Hz, figure 8.15d. After spectroscopy the dissipation reduced to zero with respect to the intrinsic dissipation, but the tip got shorter by about 160 pm, as measured via the scanner signal z . Scanning the same surface area after the spectroscopy revealed a magnetically sensitive tip with unstable spin orientation, that is, the shift in contrast along the white line in figure 8.15b indicates a spontaneous switch, and two adatoms of about 60 pm height each in figure 8.15b. Moving the tip to another surface area free of adsorbates, cf. figure 8.15c, proves the spin sensitivity with a stable tip (according to chapter 8.1.3).

The shape of the obtained E_D -curve indicates strong modifications during the approach: when a stable plateau of energy dissipation is reached, the tip dissipates additional energy on this order into the tip-sample system. Considering the tip as free standing cluster with negligible contact to the tip base according to chapter 8.13, where a weakly bound tip apex has been derived, several possible structural and magnetic non-conservative interactions exist.

For instance, the value of 4.3 eV (see close-up of E_D in figure 8.15g) corresponds very well to the binding energy of a single Fe atom in bcc iron, which is 4.28 eV [159]. The binding energies for iron clusters range from 1.837 eV/atom in Fe_2 to 2.440 eV/atom in Fe_3 , and to 2.939 eV/atom in Fe_4 , fairly approaching the bulk value. For instance, an Fe_{26} cluster has a binding energy of 4.698 eV/atom. The bulk value is reached for about 500 Fe atoms [146]. Thus, as the dissipated energy indicates severe reconfigurations at the tip apex, a breaking of atomic bonds is feasible. Of course, less severe structural changes due to relaxation might be induced into the apex cluster as well: an Fe_7 cluster, for instance, exhibits three different energetically favourable symmetries with energy differences on the order of 0.25 eV between two of these. The same accounts for other cluster sizes [146]. Changing the symmetry also changes the bond length of single Fe atoms in the cluster. An Fe_5 cluster, for instance, is found to have a noncollinear ground state, but turns ferromagnetic when the geometrical symmetry is broken [160]. Already the smallest cluster, Fe_2 , which exhibits a ferromagnetic ground state with a bond length of 220 pm is claimed to turn antiferromagnetic when the bond length is relaxed to 230 pm. The energy cost is on the order of 0.5 eV/atom [160].

During the events of largest energy dissipation at 0.955 nm and 0.96 nm distance, figure 8.15g, the tip changes drastically. The energies involved are on the order of 7 eV and the difference in dissipation between the corresponding energy levels is $\Delta E_D = 3$ eV. Hence, within one of these events the dropping of single atoms might have taken place.

8.3.2 Scanning at Close Distance

Very often, scanning over step edges, defects, vacancies and adsorbates at small tip-sample separation is the reason for spontaneous tip modifications: the coordination of iron atoms and adsorbates, for example, along the step edges, is lower than for atoms within the surface. Hence, such rim atoms might be picked up by the tip more easily (cf. figure 8.8). The knowledge that a spontaneous increase of dissipation at close distance to the surface indicates that the tip changed its state and got magnetically sensitive can be used to provoke a tip modification during scanning and avoid a tip crash: the tip is scanned across, for instance, a step edge in close distance and immediately after the excitation increases the tip is retracted slightly to secure its new tip state, either by hand, or by using the *SafeTip* feature of the data acquisition software [45], which prevents tip-crashes in the non-contact mode by monitoring the adjustable threshold of, for instance, the excitation. After moving the modified tip to a surface area known to be free of adsorbates or large topographic features, re-approaching and scanning frequently leads to magnetic contrast.

The only reliable way to distinguish a magnetically sensitive from a magnetically non-sensitive tip end is the detection of exchange and chemical forces simultaneously on a magnetically inhomogeneous sample as Fe/W(001). Though the tip does not stay stable when the surface is consequently scanned at a tip-sample separation where changes are induced, by this, several modifications driving the tip to change from magnetic sensitivity to chemical sensitivity and back again can be demonstrated. Figure 8.16a and b show dissipation and topography, respectively, obtained at constant frequency shift. The scanned surface area is the FM second layer on the left side and the AF monolayer on the upper tungsten terrace on the right side. Hence, on the left side of figure 8.16b, second layer Fe atoms are imaged equivalently with the magnetic unit cell coinciding with the chemical unit cell, while on the right side, first layer Fe atoms are imaged with a $c(2 \times 2)$ unit cell size, whenever the tip state is magnetic sensitive, that is, in part *i*, *ii*, *iii*, *vi* and *vii* of figure 8.16b. In different tip states, that is, part *iv*, *v* and *viii*, the tip shows only chemical contrast. The changes in tip length and dissipation between the different image parts are listed in the table in 8.16c, demonstrating several different states of the tip apex, showing either magnetic or chemical resolution, but none of the different states corresponds to one another.

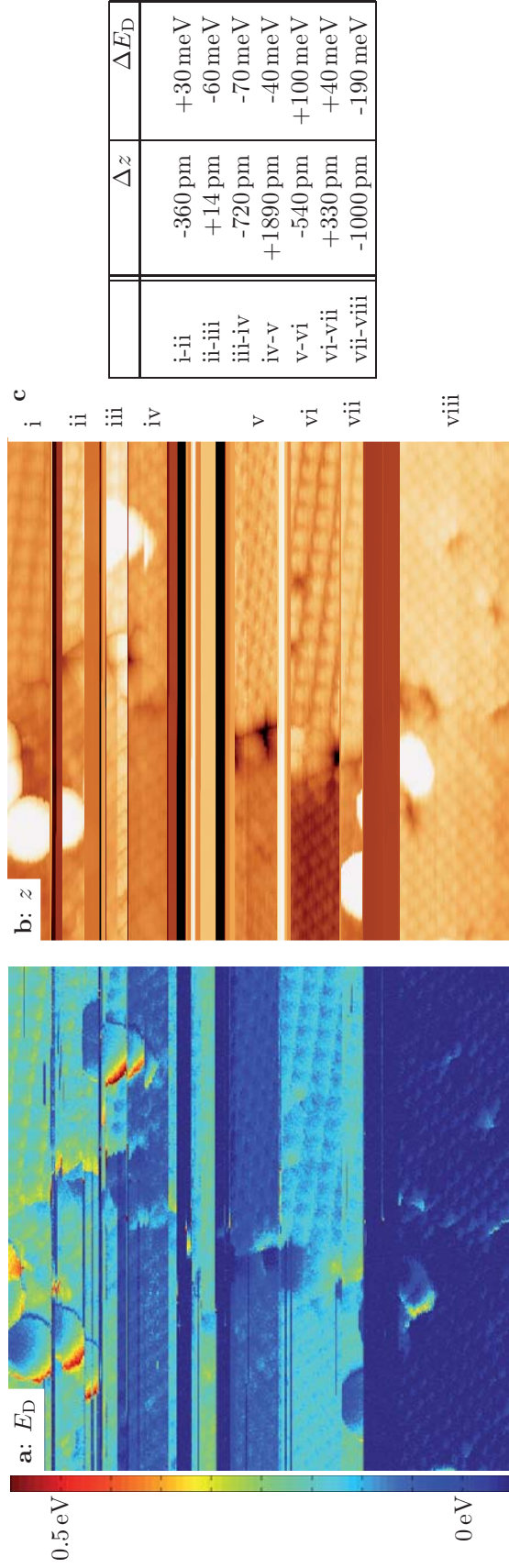


Figure 8.16: $(10 \times 10) \text{ nm}^2$ obtained with chemical and spin sensitivity across a tungsten step edge, thus covering FM second (left) and AF first (right) layer Fe (cf. figure 5.1). **a** Dissipation, E_D , **b** topography, z . **c** Changes in tip length, Δz , and difference in dissipation, ΔE_D , between several tip states.

Parameters: $\Delta f = -10 \text{ Hz}$, $c_z = 150 \text{ N/m}$, $A = 3 \text{ nm}$, $f_0 = 190 \text{ kHz}$, $B = 5 \text{ T}$, $Q = 202797$.

CHAPTER 9

SUMMARY AND OUTLOOK

The surface of iron grown on tungsten (001) in the monolayer coverage regime has been characterized structurally, electronically and magnetically using FM-AFM and related techniques in the non-contact regime. To understand the detection methods and the contrast mechanisms of the utilized AFM-based techniques, an introduction into atomic magnetism, especially into the phenomena related to magnetic exchange was followed by a discussion of the electromagnetic forces detectable by a probe above a surface, hence demonstrating the principle of AFM. After a short discourse into the instrumentation, the preparation of sample and probes was motivated and discussed in detail.

The survey of different sample properties presented in chapter 5 revealed different work functions for the first and second atomic layer iron, as well as different work functions for adjacent second layer iron stripes along the tungsten step edges. The magnetic order of the first and second layer iron was shown utilizing MFM and MExFM. A switching of the magnetization direction of free-standing second layer islands was observed for the first time. To gain deeper insights into the switching mechanisms and to get an elucidate idea whether ferromagnetic, antiferromagnetic, or anisotropic magnetic exchange play a dominant role between the first and second layer iron, additional experiments utilizing MFM or SP-STM are necessary.

Furthermore, due to its switching, two atomic layer-high iron islands on W(001) are an interesting candidate for time-resolved SP-STM measurements like those performed by KRAUSE and co-workers [25, 158, 161, 162], as the switching rate surely is much faster than observable with AFM. KRAUSE and co-workers measured the telegraph noise of switching in-plane FM monolayer patches of iron on non-magnetic W(110).

In contrast to [25, 161, 162], here the islands were grown on a magnetic substrate, that is, the AF ordered Fe monolayer on W(001). This gives rise to magnetic coupling phenomena which eventually influences the switching behaviour. Amongst the electronic and magnetic analysis of the sample system,

tip-related aspects were discussed in chapter 5, clarifying electronic and magnetic tip properties as well.

Utilizing MExFM, the $c(2 \times 2)$ AF structure of the Fe monolayer on W(001) is mapped in real-space using Fe and Cr coated tips. The results were presented in chapter 6. On Fe/W(001) much larger corrugation amplitudes compared to the previously studied NiO(001) were observed. This can be expected since the two sample systems are electronically and magnetically very different. As revealed by DFT-based simulations [10,102], the observed contrast on Fe/W(001), which is a peculiar interplay of chemical and magnetic exchange forces, strongly depends on the tip-sample separation as both interactions are electron mediated and short range in nature. Hence, both interactions are present simultaneously within the MExFM experiment. However, while on NiO(001) the magnetic contrast only appears as a supermodulation to the chemical contrast, for Fe/W(001), the contrast changes between (i) a pure magnetic contrast close to the surface (which is not yet experimentally proven) (ii) a mixture of both, chemical and exchange contrast, in an intermediate regime, and (iii) a contrast, where the exchange interaction is visible as supermodulation to the chemical contrast farther away from the surface. Comparing the previous calculations performed on NiO(001) using a single iron atom as tip [125], the present DFT results on Fe/W(001) [102,136] demonstrate that an accurate treatment of exchange forces requires a more realistic multi-atom tip and the implementation of relaxation effects. Moreover, the calculations reveal that Cr coated tips should enhance the ability to detect exchange forces already at a larger distance compared to Fe coated tips. Additionally, Cr tips are promising to be more stable at close distance than Fe tips due to a weaker coupling to the surface spins. Experimentally, it was verified that Cr coated tips, indeed, are more stable and an exchange contrast is frequently observed. Thus, using Cr coated tips, successful MExFM-experiments were performed in zero magnetic field for the first time, in contrast to the former MExFM study on NiO(001) [17].

MExFM images on Fe/W(001) revealed structural defects leading to a distortion of the magnetic configuration. By exploring defects in the materials surfaces using MExFM, vaguely understood phenomena like the exchange bias effect [163] on the interlayer between hard and soft magnetic materials, either metallic or insulating, might be addressed.

Without the limitation of conducting samples like with SP-STM, MExFM is indeed a versatile tool to study various magnetic nanostructures with atomic resolution, where different types of magnetic exchange, for example, superexchange, double exchange, or RKKY, are the driving interaction to the magnetic ordering. Hence, magnetic properties of, for example, single atoms or molecules on surfaces might be investigated. While on metallic substrates strong hybridization occurs, insulating substrates, where hybridization is absent, can be utilized using MExFM. Moreover, making use of spin-sensitive AF tips soft magnetic structures, such as domain walls, or even more complex

magnetic structures like spin spirals in electrically insulating systems can be imaged using MExFM without changing the magnetic structure with the tip stray field.

But even on conductive samples, MExFM is very useful, because it is sensitive to a different parameter compared to SP-STM. Namely, it is sensitive to the total charge density instead of the local density of states (LDOS). An interesting metallic surface to be studied with MExFM is Co/W(001) in the monolayer regime [164]. Due to hybridization with the tungsten substrate even the Co monolayer is expected to be AF with out-of-plane anisotropy [23, 165–168]. However, these theoretical predictions still lack their experimental verification. SP-STM fails, because strong states at the Fermi edge mask the magnetic states, making it difficult to probe this sample with SP-STM [167].

In chapter 7, the first direct measurement of the distance dependence of the magnetic exchange interaction across a vacuum gap was performed using the spectroscopic mode of MExFM, namely MExFS. Since measurements were performed on the AF iron monolayer on W(001), no magnetic field-dependent measurements were required and all non-magnetic contributions to the total tip-sample interaction, measured as frequency shift, were eliminated by subtracting the distance dependent curves recorded on two atomic sites with oppositely oriented atomic magnetic moments, hence, on ap- and p-site, respectively. Atomically resolved 3D-spectroscopy experiments were successfully performed using different magnetically sensitive tips, revealing two classes of distance dependent $\Delta f_{\text{ap}}(z)$ - and $\Delta f_{\text{p}}(z)$ curves with the shape of the curves being tip related. Based on the dissipation channel recorded simultaneously, the tips were classified as either non-dissipative or dissipative, hence, stable or unstable, respectively. While analysis and conversion of $\Delta f(z)$ -data obtained with non-dissipative tips is straightforward and allows one to extract the exchange energy $E_{\text{ex}}(z)$, it is not possible for dissipative tips. DFT calculations [136] using very simplified Cr/Fe cluster tip models reproduce the experimental result for the non-dissipative tips, that is, the slope of the experimental curve is comparable to the slope obtained with a symmetric, pyramidal shaped Fe tip in theory. Because accurate DFT calculations with relatively large supercells are very time consuming, it is at this point not possible to calculate a large number of different possible (and even dissipative) tip apices, including relaxation of the magnetization and different magnetic atoms as a tip end. However, theory reproduces basic features of the magnetic exchange interaction, that is, the presence or absence of a sign change as well as the absolute magnitude of the measured exchange energy. Particularly, the results demonstrate that it is indeed feasible to measure the distance dependence of the magnetic exchange interaction between atoms across a vacuum gap using MExFS.

A future perspective of MExFM and MExFS is the investigation of single magnetic atoms and molecules which are presently subject to research (SFB668 Magnetismus vom Einzelatom zur Nanostruktur, LExI-Cluster Nano-

Spintronics, ERC Advanced Grant FUnamental studies and innovative ap-pROaches of REsearch on magnetism - FURORE). A sound understanding of the atomic, as well as inter- and intra-molecular magnetic coupling on conducting and insulating surfaces, that is, with and without hybridization, respectively, is an indispensable step towards nanoscale spintronic devices [28]. Besides the possible structural manipulation of single atoms and molecules with FM-AFM [169], MExFM is able to visualize the magnetic structure and MExFS should give the possibility to switch the magnetic state of atoms, clusters or molecules involved in a controlled fashion by adjusting strength and sign of the magnetic exchange interaction by setting an appropriate tip-sample distance [137]. Unlike in previous SP-STM experiments [11, 12, 27], using force-related techniques as MExFM and MExFS on insulating samples opens a wide range of possibilities to study spin-switching and -excitation without the magnetic coupling being mediated by the substrate [4, 12, 27].

From the presented MExFM and MExFS studies, a lot of information can be gained about the structure of the tip apices. It is widely accepted [72, 148] that the tip-sample system experiences instabilities at close approach. Such instabilities are central to hysteresis mechanisms leading to an additional loss of energy during single cantilever oscillation cycles. Furthermore, low symmetry and low coordination of the tip-sample configuration enhances the dissipation of energy due to reversible or even irreversible relaxations. By analyzing the dissipation, it is experimentally confirmed that the tip apex is able to structurally and magnetically relax. A slightly different tip apex structure can completely change the dissipation signal. Hence, the dissipation is extremely sensitive to the stability and identity of the tip apex. While reversible relaxations do not permanently change a tip, irreversible relaxations do, and the tip apex is modified. Modifications are induced deliberately, for instance, during scanning the surface at close distance. Such an *in situ* tip preparation is necessary to change a chemically sensitive to a magnetically sensitive tip as none of the used tips ever showed a magnetic exchange contrast from the beginning. However, using Fe/W(001) as sample surface allows to easily distinguish chemical and magnetic exchange contrast within one image as both appear simultaneously when scanning a surface area containing FM second layer and AF monolayer.

Whether or not a modification or instability occurs, where it occurs, either at tip or sample, whether it will be reversible at all temperatures, and what the energies involved and the dependence on lateral tip position will be - all this depends on the exact nature of the tip apex [148], which might be considered as structurally and magnetically independent cluster of several or even single atoms in size.

After modification the tip apices sometimes change even drastically and neither structure nor composition can be determined experimentally. However, to know the exact tip shape and its chemical contribution is the most important requirement to get a sound understanding of the processes at its end.

Considering dissipation, it is important to have knowledge of the entire accessible energy landscape in the tip-surface junction to properly understand the imaging process at close approach. By considering more seriously how a tip is created and the processes it undergoes during scanning, it might be possible to establish some fundamental features of the tip apices. Still, this is a demanding future task [170] and a direct comparison between theoretical and experimental dissipation images is lacking [148]. This, however, would be a basis needed to perform spin-flip and spin excitation processes via the dissipation channel [171].

In conclusion, both, MExFM and MExFS, allow for a powerful analysis of all kinds of magnetic nanostructures with combined atomic and spin resolution. 3D mapping of forces is possible and further allows for a direct, quantitative measurement of the exchange interaction. Both techniques might be used to address open questions concerning nano-magnetism and spintronics and will soon be indispensable tools in the field of surface science.

BIBLIOGRAPHY

- [1] Wiesendanger, R. Spin mapping at the nanoscale and atomic scale. *Reviews of Modern Physics* **81**, 1495 (2009).
- [2] Bode, M. Spin-polarized scanning tunnelling microscopy. *Reports on Progress in Physics* **66**, 523 (2003).
- [3] Heinze, S. *et al.* Real-Space Imaging of Two-Dimensional Antiferromagnetism on the Atomic Scale. *Science* **288**, 1805 (2000).
- [4] Meier, F., Zhou, L., Wiebe, J. & Wiesendanger, R. Revealing magnetic interactions from single-atom magnetization curves. *Science* **320**, 82 (2008).
- [5] Heinrich, A. J., Gupta, J. A., Lutz, C. P. & Eigler, D. M. Single-atom spin-flip spectroscopy. *Science* **306**, 466 (2004).
- [6] Hirjibehedin, C. F., Lutz, C. P. & Heinrich, A. J. Spin coupling in engineered atomic structures. *Science* **312**, 1021 (2006).
- [7] Binnig, G., Quate, C. & Gerber, C. Atomic Force Microscope. *Physical Review Letters* **56**, 930 (1986).
- [8] Albrecht, T. R., Grütter, P., Horne, D. & Rugar, D. Frequency modulation detection using high-Q cantilevers for enhanced force microscope sensitivity. *Journal of Applied Physics* **69**, 668 (1991).
- [9] Kaiser, U., Schwarz, A. & Wiesendanger, R. Magnetic exchange force microscopy with atomic resolution. *Nature* **446**, 522 (2007).
- [10] Schmidt, R. *et al.* Probing the magnetic exchange forces of iron on the atomic scale. *Nano Letters* **9**, 200 (2009).
- [11] Wahl, P. *et al.* Exchange Interaction between Single Magnetic Adatoms. *Physical Review Letters* **98**, 56601 (2007).
- [12] Zhou, L. *et al.* Strength and directionality of surface Ruderman-Kittel-Kasuya-Yosida interaction mapped on the atomic scale. *Nature Physics* **6**, 187 (2010).

- [13] Wiesendanger, R. *et al.* Vacuum tunneling of spin-polarized electrons detected by scanning tunneling microscopy. *Journal of Vacuum Science & Technology B: Microelectronics and Nanometer Structures* **9**, 519 (1991).
- [14] Martin, Y. & Wickramasinghe, H. K. Magnetic imaging by force microscopy with 1000 Å resolution. *Applied Physics Letters* **50**, 1455 (1987).
- [15] Bhushan, B. *Scanning Probe Microscopy in Nanoscience and Nanotechnology 2*. NanoScience and Technology (Springer, 2011).
- [16] Rugar, D., Budakian, R., Mamin, H. J. & Chui, B. W. Single spin detection by magnetic resonance force microscopy. *Nature* **430**, 329 (2004).
- [17] Kaiser, U. *Magnetische Austauschkraftmikroskopie*. Ph.D. thesis, University of Hamburg (2007).
- [18] Hölscher, H., Langkat, S. M., Schwarz, A. & Wiesendanger, R. Measurement of three-dimensional force fields with atomic resolution using dynamic force spectroscopy. *Applied Physics Letters* **81**, 4428 (2002).
- [19] Langkat, S. M., Hölscher, H., Schwarz, A. & Wiesendanger, R. Determination of site specific interatomic forces between an iron coated tip and the NiO(001) surface by force field spectroscopy. *Surface Science* **527**, 12 (2003).
- [20] Hoffmann, R. *et al.* Atomic resolution imaging and frequency versus distance measurements on NiO(001) using low-temperature scanning force microscopy. *Physical Review B* **67**, 085402 (2003).
- [21] Sueoka, K., Subagyo, A., Hosoi, H. & Mukasa, K. Magnetic imaging with scanning probe microscopy. *Nanotechnology* **15**, S691 (2004).
- [22] Hosoi, H., Sueoka, K. & Mukasa, K. Investigations on the topographical asymmetry of non-contact atomic force microscopy images of NiO(001) surface observed with a ferromagnetic tip. *Nanotechnology* **15**, 505 (2004).
- [23] Ferriani, P., Heinze, S., Bihlmayer, G. & Blügel, S. Unexpected trend of magnetic order of 3d transition-metal monolayers on W(001). *Physical Review B* **72**, 024452 (2005).
- [24] Kubetzka, A. *et al.* Revealing Antiferromagnetic Order of the Fe Monolayer on W(001): Spin-Polarized Scanning Tunneling Microscopy and First-Principles Calculations. *Physical Review Letters* **94**, 087204 (2005).

- [25] Krause, S., Berbil-Bautista, L., Herzog, G., Bode, M. & Wiesendanger, R. Current-induced magnetization switching with a spin-polarized scanning tunneling microscope. *Science* **317**, 1537 (2007).
- [26] Bode, M. *et al.* Chiral magnetic order at surfaces driven by inversion asymmetry. *Nature* **447**, 190 (2007).
- [27] Serrate, D. *et al.* Imaging and manipulating the spin direction of individual atoms. *Nature nanotechnology* **5**, 350 (2010).
- [28] Khajetoorians, A. A., Wiebe, J., Chilian, B. & Wiesendanger, R. Realizing All-Spin-Based Logic Operations Atom by Atom. *Science* **332**, 1062 (2011).
- [29] Blundell, S. *Magnetism in Condensed Matter* (Oxford University Press, 2001).
- [30] Getzlaff, M. *Fundamentals of Magnetism* (Springer, 2007).
- [31] Coey, J. M. D. *Magnetism and Magnetic Materials* (Cambridge University Press, 2009).
- [32] Villars, P. & Calvert, L. D. *Pearson's Handbook of Crystallographic Data for Intermetallic Phases*, vol. 3 (American Society for Metals, 1985).
- [33] Danan, H. New Determinations of the Saturation Magnetization of Nickel and Iron. *Journal of Applied Physics* **39**, 669 (1968).
- [34] Ruderman, M. A. & Kittel, C. Indirect Exchange Coupling of Nuclear Magnetic Moments by Conduction Electrons. *Physical Review* **96**, 99 (1954).
- [35] Kasuya, T. A Theory of Metallic Ferro- and Antiferromagnetism on Zener's Model. *Progress of Theoretical Physics* **16**, 45 (1956).
- [36] Yosida, K. Magnetic Properties of Cu-Mn Alloys. *Physical Review* **106**, 893 (1957).
- [37] Slater, J. Cohesion in Monovalent Metals. *Physical Review* **35**, 509–529 (1930).
- [38] Kohlhaas, R., Dunner, P. & Schmitz-Pranghe, N. Über die Temperaturabhängigkeit der Gitterparameter von Eisen, Kobalt und Nickel im Bereich hoher Temperaturen. *Z. Angew. Phys.* **23**, 245 (1967).
- [39] Sutton, L. E. *Table of interatomic distances and configuration in molecules and ions*, vol. 18 (Chemical Society, London, UK, 1965).

- [40] Mann, J. B. *Atomic Structure Calculations II. Hartree-Fock wave functions and radial expectation values: hydrogen to lawrencium* (Los Alamos Scientific Laboratory, 1968).
- [41] Clementi, E. & Raimondi, D. L. Atomic Screening Constants from SCF Functions. *The Journal of Chemical Physics* **38**, 2686 (1963).
- [42] Skomski, R. *Simple Models of Magnetism* (Oxford University Press, 2008).
- [43] Meiklejohn, W. H. & Bean, C. P. New Magnetic Anisotropy. *Physical Review* **102**, 1413 (1956).
- [44] Meiklejohn, W. H. & Bean, C. P. New Magnetic Anisotropy. *Physical Review* **105**, 904 (1957).
- [45] Nanonis OC4, Specs Zürich, www.specs-zurich.com.
- [46] SSS-T10L250-20 and SSS-NCL-50, Nanosensors, www.nanosensors.com.
- [47] Colchero, J., Gil, A. & Baró, A. Resolution enhancement and improved data interpretation in electrostatic force microscopy. *Physical Review B* **64**, 245403 (2001).
- [48] Kitamura, S. Atomic-scale variations in contact potential difference on Au/Si(111) 7x7 surface in ultrahigh vacuum. *Applied Surface Science* **157**, 222 (2000).
- [49] Sadewasser, S. & Lux-Steiner, M. Correct Height Measurement in Non-contact Atomic Force Microscopy. *Physical Review Letters* **91**, 266101 (2003).
- [50] Schmidt, R., Schwarz, A. & Wiesendanger, R. Hydrogen-related contrast in atomic force microscopy. *Nanotechnology* **20**, 264007 (2009).
- [51] Allers, W. Dynamic scanning force microscopy at low temperatures on a van der Waals surface: graphite (0001). *Applied Surface Science* **140**, 247 (1999).
- [52] Israelachvili, J. *Intermolecular And Surface Forces* (Elsevier, 2011), 3rd edn.
- [53] Hartmann, U. Theory of van der Waals microscopy. *Journal of Vacuum Science & Technology B: Microelectronics and Nanometer Structures* **9**, 465 (1991).
- [54] Morse, P. Diatomic Molecules According to the Wave Mechanics. II. Vibrational Levels. *Physical Review* **34**, 57 (1929).

- [55] Lennard-Jones, J. E. Perturbation Problems in Quantum Mechanics. *Proceedings of the Royal Society of London. Series A, Containing Papers of a Mathematical and Physical Character* **129**, 598 (1930).
- [56] Cleveland, J. P., Anczykowski, B., Schmid, A. E. & Elings, V. B. Energy dissipation in tapping-mode atomic force microscopy. *Applied Physics Letters* **72**, 2613 (1998).
- [57] Anczykowski, B., Gotsmann, B., Fuchs, H., Cleveland, J. P. & Ellings, V. B. How to measure energy dissipation in dynamic mode atomic force microscopy. *Applied Surface Science* **140**, 376 (1999).
- [58] Hölscher, H. *et al.* Measurement of conservative and dissipative tip-sample interaction forces with a dynamic force microscope using the frequency modulation technique. *Physical Review B* **64**, 075402 (2001).
- [59] Gauthier, M., Pérez, R., Arai, T., Tomitori, M. & Tsukada, M. Interplay between Nonlinearity, Scan Speed, Damping, and Electronics in Frequency Modulation Atomic-Force Microscopy. *Physical Review Letters* **89**, 146104 (2002).
- [60] Trevethan, T., Kantorovich, L., Polesel-Maris, J. & Gauthier, S. Is atomic-scale dissipation in NC-AFM real? Investigation using virtual atomic force microscopy. *Nanotechnology* **18**, 084017 (2007).
- [61] Hug, H. J. & Baratoff, A. Measurement of Dissipation Induced by Tip-Sample Interactions. In *Noncontact Atomic Force Microscopy*, chap. 20 (Springer, 2002).
- [62] Gauthier, M., Kantorovich, L. N. & Tsukada, M. Theory of Energy Dissipation into Surface Vibrations. In *Noncontact Atomic Force Microscopy*, chap. 19 (Springer, 2002).
- [63] Denk, W. & Pohl, D. W. Local electrical dissipation imaged by scanning force microscopy. *Applied Physics Letters* **59**, 2171 (1991).
- [64] Sasaki, N. & Tsukada, M. Effect of Microscopic Nonconservative Process on Noncontact Atomic Force Microscopy. *Japanese Journal of Applied Physics* **39**, L1334 (2000).
- [65] Trevethan, T. & Kantorovich, L. Atomistic simulations of the adhesion hysteresis mechanism of atomic scale dissipation in non-contact atomic force microscopy. *Nanotechnology* **15**, S34 (2004).
- [66] Ghasemi, S. A. *et al.* Ubiquitous Mechanisms of Energy Dissipation in Noncontact Atomic Force Microscopy. *Physical Review Letters* **100**, 236106 (2008).

- [67] Hoffmann, P. M., Jeffery, S., Pethica, J. B., Özgür Özer, H. & Oral, A. Energy Dissipation in Atomic Force Microscopy and Atomic Loss Processes. *Physical Review Letters* **87**, 265502 (2001).
- [68] Kantorovich, L. N. A simple non-equilibrium theory of non-contact dissipation force microscopy. *J. Phys.: Condens. Matter* **13**, 945 (2001).
- [69] Yoshizawa, H., Chen, Y. L. & Israelachvili, J. Fundamental mechanisms of interfacial friction. 1. Relation between adhesion and friction. *The Journal of Physical Chemistry* **97**, 4128 (1993).
- [70] Dürig, U., Steinauer, H. R. & Blanc, N. Dynamic force microscopy by means of the phase-controlled oscillator method. *Journal of Applied Physics* **82**, 3641 (1997).
- [71] Cross, G. *et al.* Adhesion Interaction between Atomically Defined Tip and Sample. *Physical Review Letters* **80**, 4685 (1998).
- [72] Trevethan, T. & Kantorovich, L. Molecular dynamics simulations of atomic scale processes at close approach in non-contact atomic force microscopy. *Nanotechnology* **16**, S79 (2005).
- [73] Shluger, A. L., Kantorovich, L. N., Livshits, A. I. & Gillan, M. J. Ionic and electronic processes at ionic surfaces induced by atomic-force-microscope tips. *Physical Review B* **56**, 15332 (1997).
- [74] Caciuc, V., Hölscher, H., Blügel, S. & Fuchs, H. Hysteretic behaviour of the tip-sample interaction on an InAs(110) surface: an ab initio study. *Nanotechnology* **16**, S59 (2005).
- [75] Caciuc, V., Hölscher, H. & Blügel, S. Ab initio investigation of noncontact atomic force microscopy tip-surface instability in InAs(110) surface. *Physical Review B* **72**, 035423 (2005).
- [76] Nonnenmacher, M., O'Boyle, M. P. & Wickramasinghe, H. K. Kelvin probe force microscopy. *Applied Physics Letters* **58**, 2921 (1991).
- [77] Zerweck, U., Loppacher, C., Otto, T., Grafström, S. & Eng, L. Accuracy and resolution limits of Kelvin probe force microscopy. *Physical Review B* **71**, 125424 (2005).
- [78] Sáenz, J. J. *et al.* Observation of magnetic forces by the atomic force microscope. *Journal of Applied Physics* **62**, 4293 (1987).
- [79] Liebmann, M., Schwarz, A., Langkat, S. M. & Wiesendanger, R. A low-temperature ultrahigh vacuum scanning force microscope with a split-coil magnet. *Review of Scientific Instruments* **73**, 3508 (2002).

- [80] Liebmann, M. *Tieftemperatur-Magnetkraftmikroskopie an dünnen Manganperowskit-Filmen und Hochtemperatursupraleiter-Einkristallen*. Ph.D. thesis, University of Hamburg (2003).
- [81] Schwarz, A. Three-Dimensional Force Field Spectroscopy. *AIP Conference Proceedings* **696**, 68 (2003).
- [82] XPMPro 2.0.x, RHK Technology, www.rhk-tech.com.
- [83] Gotsmann, B., Anczykowski, B., Seidel, C. & Fuchs, H. Determination of tip-sample interaction forces from measured dynamic force spectroscopy curves. *Applied Surface Science* **140**, 314 (1999).
- [84] Gotsmann, B., Seidel, C., Anczykowski, B. & Fuchs, H. Conservative and dissipative tip-sample interaction forces probed with dynamic AFM. *Physical Review B* **60**, 11051 (1999).
- [85] Dürig, U. Relations between interaction force and frequency shift in large-amplitude dynamic force microscopy. *Applied Physics Letters* **75**, 433 (1999).
- [86] Hölscher, H., Schwarz, A., Allers, W., Schwarz, U. & Wiesendanger, R. Quantitative analysis of dynamic-force-spectroscopy data on graphite(0001) in the contact and noncontact regimes. *Physical Review B* **61**, 12678 (2000).
- [87] Giessibl, F. Forces and frequency shifts in atomic-resolution dynamic-force microscopy. *Physical Review B* **56**, 16010 (1997).
- [88] Giessibl, F. J. A direct method to calculate tip-sample forces from frequency shifts in frequency-modulation atomic force microscopy. *Applied Physics Letters* **78**, 123 (2001).
- [89] Sader, J. E. & Jarvis, S. P. Accurate formulas for interaction force and energy in frequency modulation force spectroscopy. *Applied Physics Letters* **84**, 1801 (2004).
- [90] Giessibl, F. J. Advances in atomic force microscopy. *Reviews of Modern Physics* **75**, 949 (2003).
- [91] MATLAB R2010b, MathWorks, www.mathworks.com/products/matlab.
- [92] UHV-AFM/STM, Omicron NanoTechnology GmbH, www.omicron.de.
- [93] Lämmle, K. *Aufbau einer Verdampferapparatur zur Präparation von Molekülen im Ultrahochvakuum*. Diploma thesis, University of Hamburg (2006).

- [94] Sader, J. E., Larson, I., Mulvaney, P. & White, L. R. Method for the calibration of atomic force microscope cantilevers. *Review of Scientific Instruments* **66**, 3789 (1995).
- [95] Wetzel, P., Pirri, C., Peruchetti, J., Bolmont, D. & Gewinner, G. Formation of CrSi and CrSi₂ upon annealing of Cr overlayers on Si(111). *Physical Review B* **35**, 5880 (1987).
- [96] Wawro, A., Suto, S., Czajka, R. & Kasuya, A. Thermal reaction of iron with a Si(111) vicinal surface: Surface ordering and growth of CsCl-type iron silicide. *Physical Review B* **67**, 195401 (2003).
- [97] Klein, L. J., Williams, C. C. & Kim, J. Electron tunneling detected by electrostatic force. *Applied Physics Letters* **77**, 3615 (2000).
- [98] Klein, L. J. & Williams, C. C. Single electron tunneling detected by electrostatic force. *Applied Physics Letters* **79**, 1828 (2001).
- [99] Zabel, H. Magnetism of chromium at surfaces, at interfaces and in thin films. *Journal of Physics: Condensed Matter* **11**, 9303 (1999).
- [100] Grempel, D. Surface magnetic ordering in chromium. *Physical Review B* **24**, 3928 (1981).
- [101] Blügel, S., Pescia, D. & Dederichs, P. H. Ferromagnetism versus antiferromagnetism of the Cr(001) surface. *Physical Review B* **39**, 1392 (1989).
- [102] Lazo, C., Caciuc, V., Hölscher, H. & Heinze, S. Role of tip size, orientation, and structural relaxations in first-principles studies of magnetic exchange force microscopy and spin-polarized scanning tunneling microscopy. *Physical Review B* **78**, 214416 (2008).
- [103] EFM3 Evaporator, Omicron NanoTechnology GmbH, www.omicron.de.
- [104] Schmidt, R. *Rasterkraftspektroskopie auf Ag(111) und Gd/W(110)*. Diploma thesis, University of Hamburg (2005).
- [105] Ultimex UX20P, IRCON Infrared Thermometers, www.ircon.com.
- [106] Potekhina, N., Gall', N., Rut'kov, E. & Tontegode, A. Carbon segregation on a tungsten surface. *Physics of the Solid State* **45**, 782 (2003).
- [107] von Bergmann, K., Bode, M. & Wiesendanger, R. Magnetism of iron on tungsten (001) studied by spin-resolved scanning tunneling microscopy and spectroscopy. *Physical Review B* **70**, 174455 (2004).

- [108] Yamasaki, A., Wulfhekel, W., Hertel, R., Suga, S. & Kirschner, J. Direct Observation of the Single-Domain Limit of Fe Nanomagnets by Spin-Polarized Scanning Tunneling Spectroscopy. *Physical Review Letters* **91**, 127201 (2003).
- [109] CapaciTorr Pump, SAES Getters S.p.A., www.saesgetters.com.
- [110] Plihal, M., Mills, D., Elmers, H. & Gradmann, U. Spin-polarized-electron scattering studies of the Fe bilayer on W(100): Theory and experiment. *Physical Review B* **51**, 8193 (1995).
- [111] von Bergmann, K. *Iron nanostructures studied by spin-polarised scanning tunneling microscopy*. Ph.D. thesis, University of Hamburg (2004).
- [112] Wu, R. Magnetism of Fe on W(001) and the effects of oxygen adsorption. *Journal of Magnetism and Magnetic Materials* **127**, 327 (1993).
- [113] Jacobs, H. O., Leuchtman, P., Homan, O. J. & Stemmer, A. Resolution and contrast in Kelvin probe force microscopy. *Journal of Applied Physics* **84**, 1168 (1998).
- [114] Mulhollan, G., Fink, R., Erskine, J. & Walters, G. Local spin correlations in ultrathin Fe/W(100) films. *Physical Review B* **43**, 13645 (1991).
- [115] Chen, J. & Erskine, J. Surface-step-induced magnetic anisotropy in thin epitaxial Fe films on W(001). *Physical Review Letters* **68**, 1212 (1992).
- [116] Wu, R. & Freeman, A. Magnetic properties of Fe overlayers on W(001) and the effects of oxygen adsorption. *Physical Review B* **45**, 7532 (1992).
- [117] Jones, T. Structural and magnetic characterization of thin iron films on a tungsten (001) substrate. *Surface Science* **302**, 126 (1994).
- [118] Sandratskii, L., Sasioglu, E. & Bruno, P. Exchange interactions and Néel temperature of a Fe monolayer on W(001): A first-principles study. *Physical Review B* **73**, 014430 (2006).
- [119] Bode, M. *et al.* Atomic spin structure of antiferromagnetic domain walls. *Nature materials* **5**, 477 (2006).
- [120] Niu, Y. R. & Altman, M. S. Superparamagnetic limit to spin-polarized vacuum tunneling from Fe-coated W(001) tips. *Applied Physics Letters* **95**, 203113 (2009).
- [121] Wulfhekel, W., Zavaliche, F., Porrati, F., Oepen, H. P. & Kirschner, J. Nano-patterning of magnetic anisotropy by controlled strain relief. *Europhysics Letters* **49**, 651 (2000).

- [122] Liebmann, M. *Aufbau und Charakterisierung eines Rasterkraftmikroskops für den Einsatz im Ultrahochvakuum, bei tiefen Temperaturen und im Magnetfeld*. Ph.D. thesis, University of Hamburg (2000).
- [123] Kaiser, U., Schwarz, A. & Wiesendanger, R. Evaluating local properties of magnetic tips utilizing an antiferromagnetic surface. *Physical Review B* **78**, 104418 (2008).
- [124] Schwarz, A., Kaiser, U. & Wiesendanger, R. Towards an understanding of the atomic scale magnetic contrast formation in NC-AFM: a tip material dependent MExFM study on NiO(001). *Nanotechnology* **20**, 264017 (2009).
- [125] Momida, H. & Oguchi, T. First-principles study on exchange force image of NiO(001) surface using a ferromagnetic Fe probe. *Surface Science* **590**, 42 (2005).
- [126] Kiwi, M. Exchange bias theory. *Journal of Magnetism and Magnetic Materials* **234**, 584 (2001).
- [127] Ohldag, H. *et al.* Correlation between Exchange Bias and Pinned Interfacial Spins. *Physical Review Letters* **91**, 017203 (2003).
- [128] Koon, N. Calculations of Exchange Bias in Thin Films with Ferromagnetic/Antiferromagnetic Interfaces. *Physical Review Letters* **78**, 4865 (1997).
- [129] Schulthess, T. & Butler, W. Consequences of Spin-Flop Coupling in Exchange Biased Films. *Physical Review Letters* **81**, 4516 (1998).
- [130] Takano, K., Kodama, R., Berkowitz, A., Cao, W. & Thomas, G. Interfacial Uncompensated Antiferromagnetic Spins: Role in Unidirectional Anisotropy in Polycrystalline Ni₈₁Fe₁₉/CoO Bilayers. *Physical Review Letters* **79**, 1130 (1997).
- [131] Takano, K., Kodama, R. H., Berkowitz, A. E., Cao, W. & Thomas, G. Role of interfacial uncompensated antiferromagnetic spins in unidirectional anisotropy in Ni₈₁Fe₁₉/CoO bilayers (invited). *Journal of Applied Physics* **83**, 6888 (1998).
- [132] Malozemoff, A. Random-field model of exchange anisotropy at rough ferromagnetic-antiferromagnetic interfaces. *Physical Review B* **35**, 3679 (1987).
- [133] Nowak, U. *et al.* Domain state model for exchange bias. I. Theory. *Physical Review B* **66**, 014430 (2002).

- [134] Keller, J. *et al.* Domain state model for exchange bias. II. Experiments. *Physical Review B* **66**, 014431 (2002).
- [135] Tao, K. *et al.* Manipulating magnetism and conductance of an adatom-molecule junction on a metal surface: An ab initio study. *Physical Review B* **78**, 014426 (2008).
- [136] Lazo, C., private communication.
- [137] Tao, K. *et al.* Switching a Single Spin on Metal Surfaces by a STM Tip: Ab Initio Studies. *Physical Review Letters* **103**, 057202 (2009).
- [138] Schmidt, R. *et al.* Quantitative Measurement of the Magnetic Exchange Interaction across a Vacuum Gap. *Physical Review Letters* **106**, 257202 (2011).
- [139] Caciuc, V., Hölscher, H., Blügel, S. & Fuchs, H. Atomic-Scale Sharpening of Silicon Tips in Noncontact Atomic Force Microscopy. *Physical Review Letters* **96**, 016101 (2006).
- [140] Hoffmann, R. *et al.* Mechanical manifestations of rare atomic jumps in dynamic force microscopy. *Nanotechnology* **18**, 395503 (2007).
- [141] Oyabu, N. *et al.* Single Atomic Contact Adhesion and Dissipation in Dynamic Force Microscopy. *Physical Review Letters* **96**, 106101 (2006).
- [142] Pérez, R., Payne, M., Štich, I. & Terakura, K. Role of Covalent Tip-Surface Interactions in Noncontact Atomic Force Microscopy on Reactive Surfaces. *Physical Review Letters* **78**, 678 (1997).
- [143] Hoffmann, R. *Magnetic and interatomic forces measured by low temperature scanning force microscopy*. Ph.D. thesis, University of Basel (2001).
- [144] Bennewitz, R. *et al.* Atomically resolved edges and kinks of NaCl islands on Cu(111): Experiment and theory. *Physical Review B* **62**, 2074 (2000).
- [145] Slater, J. C. Atomic Radii in Crystals. *The Journal of Chemical Physics* **41**, 3199 (1964).
- [146] Bobadova-Parvanova, P. *et al.* Scanning the potential energy surface of iron clusters: A novel search strategy. *The Journal of Chemical Physics* **116**, 3576 (2002).
- [147] Proksch, R., Babcock, K. & Cleveland, J. Magnetic dissipation microscopy in ambient conditions. *Applied Physics Letters* **74**, 419 (1999).

- [148] Trevethan, T. & Kantorovich, L. N. Models of atomic scale contrast in dissipation images of binary ionic surfaces in non-contact atomic force microscopy. *Nanotechnology* **17**, S205 (2006).
- [149] Néel, L. Théorie du traînage magnétique des ferromagnétiques en grains fins avec applications aux terres cuites. *Ann. Géophys.* **5**, 99 (1949).
- [150] Brown, W. F. Thermal Fluctuations of a Single-Domain Particle. *Physical Review* **130**, 1677 (1963).
- [151] Cabria, I., Nonas, B., Zeller, R. & Dederichs, P. Orbital magnetism of transition-metal adatoms and clusters on the Ag and Au(001) surfaces. *Physical Review B* **65**, 054414 (2002).
- [152] Gambardella, P. *et al.* Giant magnetic anisotropy of single cobalt atoms and nanoparticles. *Science* **300**, 1130 (2003).
- [153] Gambardella, P., Rusponi, S., Cren, T., Weiss, N. & Brune, H. Magnetic anisotropy from single atoms to large monodomain islands of Co/Pt(111). *Comptes Rendus Physique* **6**, 75 (2005).
- [154] Hirjibehedin, C. F. *et al.* Large magnetic anisotropy of a single atomic spin embedded in a surface molecular network. *Science* **317**, 1199 (2007).
- [155] Etz, C., Zabloudil, J., Weinberger, P. & Vedmedenko, E. Magnetic properties of single atoms of Fe and Co on Ir(111) and Pt(111). *Physical Review B* **77**, 184425 (2008).
- [156] Balashov, T. *et al.* Magnetic Anisotropy and Magnetization Dynamics of Individual Atoms and Clusters of Fe and Co on Pt(111). *Physical Review Letters* **102**, 257203 (2009).
- [157] Shick, A. B., Máca, F. & Lichtenstein, A. I. Magnetic anisotropy of single Co atom on CuN surface. *Journal of Applied Physics* **105**, 07C309 (2009).
- [158] Krause, S. *Thermal and Current-Induced Magnetization Switching of Fe/W(110) Nanoislands Investigated by Spin-Polarized Scanning Tunneling Microscopy*. Ph.D. thesis, University of Hamburg (2008).
- [159] Elliott, J. A., Shibuta, Y. & Wales, D. J. Global minima of transition metal clusters described by Finnis-Sinclair potentials: A comparison with semi-empirical molecular orbital theory. *Philosophical Magazine* **89**, 3311 (2009).
- [160] Köhler, C., Frauenheim, T., Hourahine, B., Seifert, G. & Sternberg, M. Treatment of collinear and noncollinear electron spin within an approximate density functional based method. *The Journal of Physical Chemistry A* **111**, 5622 (2007).

- [161] Krause, S. *et al.* Magnetization Reversal of Nanoscale Islands: How Size and Shape Affect the Arrhenius Prefactor. *Physical Review Letters* **103**, 127202 (2009).
- [162] Herzog, G., Krause, S. & Wiesendanger, R. Heat assisted spin torque switching of quasistable nanomagnets across a vacuum gap. *Applied Physics Letters* **96**, 102505 (2010).
- [163] Nogués, J. & Schuller, I. K. Exchange bias. *Journal of Magnetism and Magnetic Materials* **192**, 203 (1999).
- [164] Köhler, A. *Rasterkraftmikroskopie an Monolagen von Co auf W(001) und Graphen auf Ru(0001)*. Diploma thesis, University of Hamburg (2011).
- [165] Ondracek, M., Kudrnovský, J., Turek, I. & Maca, F. Magnetism of 3d transition metal atoms on W(001): submonolayer films. *Journal of Physics: Conference Series* **61**, 894 (2007).
- [166] Bergman, A., Nordström, L., Klautau, A. B., Frota-Pessoa, S. & Eriksson, O. Magnetism of Co overlayers and nanostructures on W(001): A first-principles study. *Journal of Magnetism and Magnetic Materials* **320**, 1173 (2008).
- [167] Kubetzka, A., private communication.
- [168] Yun, W. S., Hong, S. C., Lee, J. I. & Hwang, C. Magnetism of Co layers Grown on W(001) Surface: Density Functional Study. *Journal of the Korean Physical Society* **56**, 1472 (2010).
- [169] Custance, O., Pérez, R. & Morita, S. Atomic force microscopy as a tool for atom manipulation. *Nature nanotechnology* **4**, 803 (2009).
- [170] Foster, A. S., Shluger, A. L. & Nieminen, R. M. Realistic model tips in simulations of nc-AFM. *Nanotechnology* **15**, S60 (2004).
- [171] Pellegrini, F., Santoro, G. & Tosatti, E. Atomic Spin-Sensitive Dissipation on Magnetic Surfaces. *Physical Review Letters* **105**, 146103 (2010).

PUBLICATIONS

1. Schmidt, R., Kaiser, U., Lazo, C., Schwarz, A., Wiesendanger, R. & Heinze, S. Quantitative measurement of the magnetic exchange interaction across a vacuum gap. *Physical Review Letters* **106**, 257202 (2011).
2. Schmidt, R., Lazo, C., Hölscher, H., Pi, U. H., Caciuc, V., Schwarz, A., Wiesendanger, R. & Heinze, S. Probing the Magnetic Exchange Forces of Iron on the Atomic Scale. *Nano Letters* **9**, 200 (2009).
3. Schmidt, R., Schwarz, A. & Wiesendanger, R. Hydrogen-related contrast in atomic force microscopy, *Nanotechnology* **20**, 264007 (2009).
4. Schwarz, A., Kaiser, U., Schmidt, R. & Wiesendanger, R. Magnetic Exchange Force Microscopy in *Noncontact Atomic Force Microscopy* Vol. 2, Springer-Verlag Heidelberg (2009).

TALKS & CONFERENCES

Talks

1. R. Schmidt: *Magnetic Exchange Force Microscopy and Spectroscopy on Fe/W(001)*, Seminar über Wachstum und Magnetismus von Systemen reduzierter Dimensionen, Hamburg (Germany), 24.06.2011.
2. R. Schmidt, C. Lazo, A. Schwarz, S. Heinze, and R. Wiesendanger: *Magnetic Exchange Force Spectroscopy on antiferromagnetic Fe/W(001)*, 75rd Spring Conference, Deutsche Physikalische Gesellschaft, Dresden (Germany), 14.03.2011.
3. R. Schmidt, U. Kaiser, A. Schwarz, and R. Wiesendanger: *Measuring the distance dependence of the magnetic exchange interaction across a vacuum gap*, 74rd Spring Conference, Deutsche Physikalische Gesellschaft, Regensburg (Germany), 22.03.2010.
4. R. Schmidt: *Magnetic Exchange Force Microscopy*, LEXI-Workshop *Nanospintronics*, Hamburg (Germany), 03.03.2010.
5. R. Schmidt, C. Lazo, U. Kaiser, A. Schwarz, S. Heinze, and R. Wiesendanger: *High Resolution 3D-Force-Field-Spectroscopy on Fe/W(001)*, 73rd Spring Conference, Deutsche Physikalische Gesellschaft, Dresden (Germany), 25.03.2009.
6. R. Schmidt: *Probing the Magnetic Exchange Forces of Iron on the Atomic Scale*, GK 611 *Design and Characterisation of Functional Materials* - Seminarbeitrag, Hamburg (Germany), 04.02.2009.
7. R. Schmidt: *Magnetic Exchange Force Microscopy*, GK 611 *Design and Characterisation of Functional Materials* - Bonding 2008, Weissenhäuser Strand (Germany), 17.10.2008.
8. R. Schmidt, C. Lazo, U. H. Pi, V. Caciuc, H. Hölscher, A. Schwarz, R. Wiesendanger, and S. Heinze: *Probing Fe/W(001) with magnetic exchange force microscopy*, European Conference on Surface Science (ECOSS 2008), Liverpool (UK), 30.07.2008.

9. R. Schmidt, U. H. Pi, A. Schwarz, and R. Wiesendanger: *Fe/W(001) - a structurally, electronically and magnetically inhomogeneous system studied by force microscopy*, 72nd Spring Conference, Deutsche Physikalische Gesellschaft, Berlin (Germany), 28.02.2008.
10. R. Schmidt, U. H. Pi, A. Schwarz, and R. Wiesendanger: *Fe/W(001) - a structurally, electronically and magnetically inhomogeneous system studied by force microscopy*, 10th International Conference on Non-Contact Atomic Force Microscopy (NCAFM 2007), Antalya (Türkei), 17.09.2007.
11. R. Schmidt, K. Lämmle, U. H. Pi, A. Schwarz, R. Wiesendanger: *Towards Magnetic Exchange Force Microscopy*, GrK 611 *Design and Characterisation of Functional Materials* - Bonding 2006, Weissenhäuser Strand (Germany), 14.10.2006.
12. R. Schmidt, A. Schwarz, and R. Wiesendanger: *Hydrogen-altered Gd(0001) surfaces investigated by dynamic force microscopy*, 9th International Conference on Noncontact Atomic Force Microscopy (NCAFM 2006), Kobe (Japan), 18.07.2006.
13. R. Schmidt, A. Schwarz, and R. Wiesendanger: *Hydrogen-altered Gd(0001) surfaces investigated by dynamic force microscopy*, 70th Spring Conference, Deutsche Physikalische Gesellschaft, Dresden (Germany), 28.03.2006.

Posters

1. R. Schmidt, C. Lazo, H. Hölscher, V. Caciuc, A. Schwarz, R. Wiesendanger and S. Heinze: *Probing Fe/W(001) with Magnetic Exchange Force Microscopy*, 20th International Colloquium on Magnetic Films and Surfaces (ICMFS), Berlin (Germany), 23.07.2009.
2. R. Schmidt, C. Lazo, U. H. Pi, V. Caciuc, H. Hölscher, A. Schwarz, R. Wiesendanger and S. Heinze: *Probing Fe/W(001) with magnetic and exchange force microscopy*, International Conference on Nanoscience and Technology, Keystone, Colorado (USA), 22.07.2008.
3. R. Schmidt, U. H. Pi, A. Schwarz, and R. Wiesendanger: *Structural and magnetic properties of Fe/W(001) studied by force microscopy*, International Conference on Nanoscience and Technology, Stockholm (Schweden), 02.07.2007.
4. R. Schmidt, M. Zeyer-Düsterer, A. Schwarz, and R. Wiesendanger: *Formation of Ag islands on Ag(111) using AFM in the dynamic mode*, 8th International Conference on Noncontact Atomic Force Microscopy (NCAFM 2005), Bad Essen (Germany), 17.08.2005.

ACKNOWLEDGEMENTS

Many sincere thanks are given to all who contributed to this work and to all who supported me in this extensive project.

In particular I would like to thank Prof. Dr. Roland Wiesendanger who gave me the chance to do research on a very sophisticated level. I further thank Dr. Alexander Schwarz for the supervision and for sharing his experience in all aspects of daily lab work, whenever it was needed. Many thanks go to Dr. Uwe Kaiser for sharing measurement time, daily lab work and many MATLAB code snippets, and to Dr. Ung-Hwan Pi for his great support in the early beginnings of the Fe/W(001)-project. Prof. Dr. Stefan Heinze and Dr. Cesar Lazo contributed a lot to this thesis by performing all presented DFT calculations and I would like to thank both for their excellent work. I would further like to thank Prof. Dr. Hendrik Hölscher and Dr. Vasile Caciuc for simulating the MExFM images, hence providing a basis to compare experimental and theoretical data.

Many thanks go to all of my former and recent lab mates for a great teamwork and many fruitful discussions. The same is true for the whole Group R and I would like to thank all members for the pleasant working atmosphere.

Very special thanks go to my parents for their in every respect wonderful support during all the time.

Most of all I would like to thank my wife Martina, for giving me all the love and emotional support. There were many ups and even more downs, but together with our daughters, Laura and Luisa, you always kept me smiling and moving on.

